VIETNAM NATIONAL UNIVERSITY, HANOI
UNIVERSITY OF SCIENCE

Pham The An

IMPROVEMENTS OF CRITICAL CURRENT DENSITY OF Bi-Pb-Sr-Ca-Cu-O HIGH-T_c SUPERCONDUCTOR BY ADDITIONS OF NANO-STRUCTURED PINNING CENTERS

Major: Thermophysics

Code: 9440130.07

DISSERTATION FOR DOCTOR OF PHILOSOPHY IN PHYSICS

SUPERVISORS :

1. Dr. Luu Tuan Tai

   Professor of Physics

2. Dr. Tran Hai Duc

   Associate Professor of Physics

Ha Noi - 2023

DECLARATION

I hereby declare that this is my own research work. The results written in collaboration with other authors have been approved by the co-authors prior to being included in the thesis. The results presented in the thesis are truthful and have not been published in any other works.

Author

Pham The An

ACKNOWLEDGMENTS

Time as a doctoral student is the first step on our academic long journey. A challenging period that demanded great effort and perseverance, but was extremely rewarding, has enabled me to develop the necessary mindset, skills, and character to conduct independent research and contribute to scientific advancement. The achievements that I have attained today have greatly benefited from the contribution and support of my supervisors, lab-mates, colleagues, friends, and family. Although these words can never fully express my gratitude and love, I would like to send my sincerest thanks to those who have accompanied me throughout this journey.

First and foremost, I would like to express my highest reverent gratitude to my supervisors – Asso.Prof. Tran Hai Duc and Prof. Luu Tuan Tai, for their supervision, guidance, and invaluable feedback throughout the journey. Their insightful comments and constructive criticisms were instrumental in shaping and refining my research work. I am truly grateful for the time and effort they have devoted to helping me achieve my academic goals.

I am also grateful to the members of my dissertation committee, for their precise feedback. Their constructive comments and suggestions have immensely improved the quality of my work.

I would like to express my appreciation to my lab-mates, colleagues, and friends, who have provided enthusiasm and valuable support to me during the research. I extend my gratitude to the professors and staffs at my faculty and functional departments, especially, Dr. Nguyen Duy Thien, Dr. Sai Cong Doanh, Dr. Nguyen Quang Hoa at Faculty of Physics, Asso.Prof. Nguyen Hoang Nam at Nano and Energy Center, and Dr. Nguyen Thanh Binh, University of Science, Vietnam National University; Dr. Nguyen Khac Man at International Training Institute for Materials Science, Hanoi University of

Science and Technology, who have provided me with administrative and technical support. I also would like to express my appreciation for the collaboration with the research groups of Dr. Le Minh Tien, Msc. Tran Tien Dzung at Sungkyunkwan University (Korea), Dr. Wantana Klysubun at Synchrotron Light Resource Institute (Thailand), and Prof. Takafumi Miyanaga at Hirosaki University (Japan). Their assistance has been crucial in facilitating the completion of my doctoral course.

I would like to thank PhD Scholarship Programme of Vingroup Innovation Foundation, the Institute of Big Data and The Development Foundation of Vietnam National University, Hanoi for sponsoring my research.

Lastly, I would like to express my sincere gratitude to my family and my girlfriend, for their support, encouragement, and spiritual strength during all of this challenging period. Their love has been my great motivation to achieve every goal. I am most sincerely grateful for their sacrifices and unwavering belief in me.

Ha Noi, August 2023

Pham The An

CONTENTS

LIST OF NOTATIONS AND ABBREVIATIONS

Notations	Explain
%Bi-2212	volume fraction of Bi-2212 phase
%Bi-2223	volume fraction of Bi-2223 phase
APC	artifial pinning center
A-L	Azlamazov-Larkin
b	normalized field ($b = B/B_{irr}$)
B_{c1}	lower critical field
B_{c2}	upper critical field
BCS	Bardeen-Cooper-Schrieffer
B_{irr}	irreversibility field
B_{lb}	large bundle field
b_{peak}	reduced field at maximum of flux pinning force density
BSCCO	Bi-Sr-Ca-Cu-O
BPSCCO	Bi-Pb-Sr-Ca-Cu-O
B_{sb}	small bundle field
d	effective inter-layering spacing
d_ϕ	inter-flux-line spacing
e	electron charge
F_L	Lorentz force density
F_p	pinning force density
f_p	normalized pinning force density ($f_p = F_p/F_{p,max}$)
$F_{p,max}$	maximum value of pinning force density
FWHM	full width at half maximum
$\hbar$	reduced Planck constant
HTS	high-T_c superconductor
I	electric current

I_{2212}	X-ray diffraction intensity of Bi-2212 phase
I_{2223}	X-ray diffraction intensity of Bi-2223 phase
j	normalized critical current density ($j = J_c/J_c(0)$)
J	interlayer coupling strength
J_c	critical current density
J_{sv}	critical current density in single vortex regime
k	Gaussian critical exponent
k_B	Boltzmann's constant
L-D	Lawrence-Doniach
PPMS	Physical Property Measurement System
R	resistance
SEM	scanning electron microscopy
T	temperature
t	normalized temperature ($t = T/T_c$)
T_c	critical temperature
TEM	transmission electron microscopy
T_{LD}	Lawrence–Doniach temperature
U	voltage difference
U_0	pinning potential
v	hole concentration
V	valence
$XANES$	X-ray absorption near edge structure
XAS	X-ray absorption spectrocopy
XRD	X-ray diffraction
ΔM	magnetization hysteresis width
$\Delta\sigma$	excess conductivity
ε	reduced temperature ($\varepsilon = (T - T_c)/T_c$)

λ	coherence length
$\lambda_{Cu\text{-}K\alpha}$	Cu-Kα radiation wavelength
ξ	penetration depth
ξ_c	c-axis coherence length
ρ	resistivity
ρ_0	residual resistivity
τ	crystallite size
Φ_0	magnetic flux quantum

LIST OF TABLES

LIST OF FIGURES

ABSTRACT

It has been approximately 40 years since the high-temperature superconductor Bi-Pb-Sr-Ca-Cu-O (BPSCCO) was discovered. Both theoretical and experimental studies on BPSCCO have been carried out to investigate the mechanism as well as the applications of the material. Some potential application areas on BPSCCO superconductors are the ability of electric power transmission at the temperature region in the vicinity of liquid nitrogen and under the applied fields. To address this scientific purpose, the so-called flux pinning properties of BPSCCO superconductors are strongly required to be improved.

The objective of this dissertation is to systematically investigate the impact of pinning center additions on the enhancement of the critical current density (J_c) and the flux pinning mechanism in $Bi_{1.6}Pb_{0.4}Sr_2Ca_2Cu_3O_{10+\delta}$ polycrystalline superconductors synthesized using the conventional solid-state reaction method. Types of nano-structured pinning centers with the increased average size and different magnetic properties, including point-like defects, non-magnetic, and magnetic nanoparticles, were added to $Bi_{1.6}Pb_{0.4}Sr_2Ca_2Cu_3O_{10+\delta}$ superconductors to systematically study the resultant changes in flux pinning properties of the fabricated samples. The pinning-related parameters were also obtained by using the collective pinning and Dew-Hughes models, those were the most important motivations in this work.

The results showed that the additions of nano-structured pinning centers all provided clear J_c enhancements while maintaining T_c above 77 K. In comparison, the highest J_c enhancement was obtained for the addition of the magnetic nanoparticles. By using the collective pinning model, the dominant pinning mechanism of all fabricated samples was found to be δl pinning. By using the Dew-Hughes, the geometry of pinning centers was identified.

The 2-dimensional (2D) and 0-dimensional (0D) pinning were found to be dominant in the pure and nano-structured pinning center added $Bi_{1.6}Pb_{0.4}Sr_2Ca_2Cu_3O_{10+\delta}$ samples, respectively.

The additions of nano-structured pinning centers have been proved to enhance J_c in $Bi_{1.6}Pb_{0.4}Sr_2Ca_2Cu_3O_{10+\delta}$ polycrystalline superconductors. The results might be used as solid evidences for expansions of potential studies in power-related applications of high-temperature superconductors near future.

CHAPTER 1: OVERVIEW

1.1. INTRODUCTION

1.1.1. History of Superconductivity

Superconductivity is a fascinating phenomenon that occurs when certain materials are cooled below a certain critical temperature. At this temperature, the materials can conduct electricity with zero resistance, which has the potential to revolutionize a wide range of industries. This discovery has led to many technological advancements, and scientists are still working to uncover the secrets behind superconductivity.

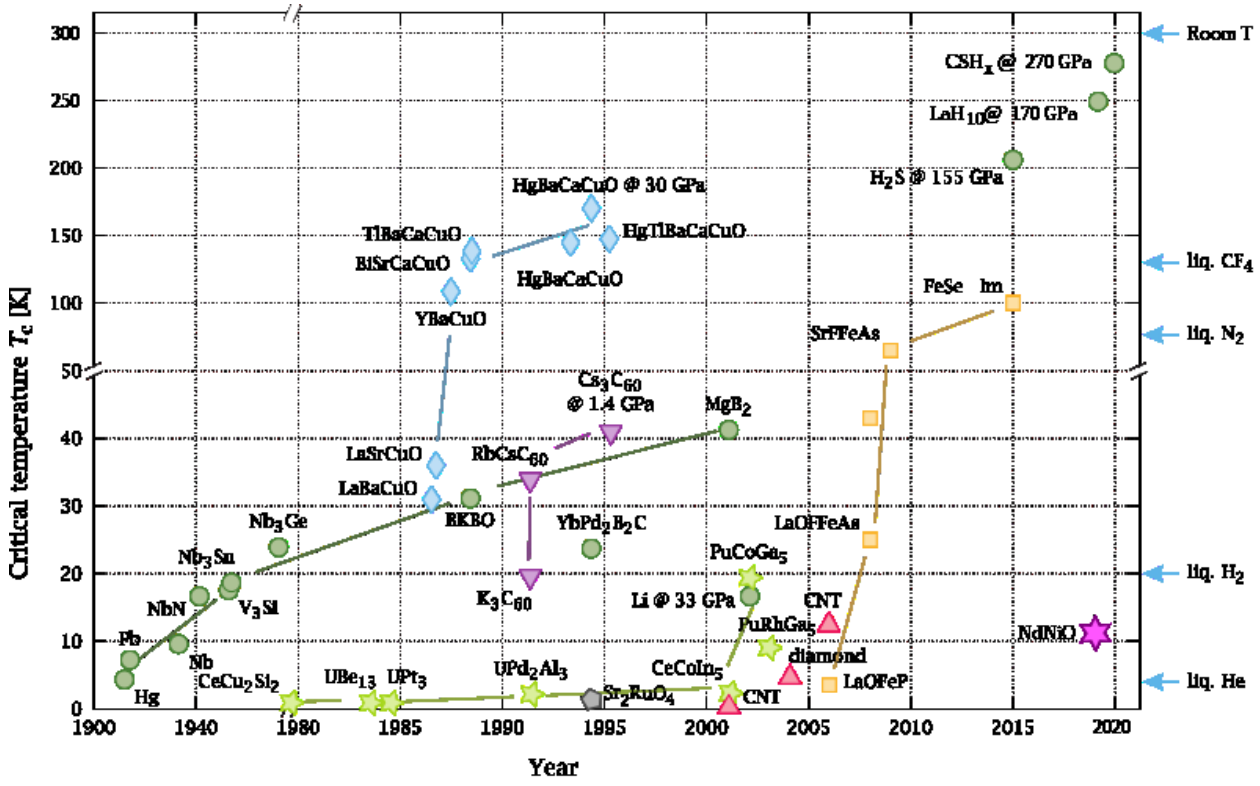

Figure 1.1. History of Superconductivity [83].

The discovery of superconductivity dates back to 1911 when Dutch physicist Heike Kamerlingh Onnes was conducting experiments on the properties of matter at extremely low temperatures. He found that when he cooled mercury to a temperature of 4.2 K (-268.8 ºC), it suddenly became a

perfect conductor of electricity, with zero resistance. This marked the first time that superconductivity had been observed, and it quickly sparked a flurry of research in the field as summary in Figure 1.1 [37].

One of the most interesting aspects of superconductivity is that it is a quantum mechanical phenomenon. At extremely low temperatures, electrons in the material pair up and form what are known as Cooper pairs. These Cooper pairs can move through the material without encountering any resistance, which allows the material to conduct electricity with zero resistance. The exact mechanism behind the formation of Cooper pairs is still not fully understood, and scientists continue to study this phenomenon to gain a better understanding of the physics behind superconductivity [9].

Superconductivity has many practical applications, particularly in the field of electrical engineering. For example, superconducting wires can be used to transmit electricity with zero resistance, which would significantly reduce energy loss during transmission. This could lead to more efficient power grids and lower energy costs for consumers. Superconducting magnets are also used in a variety of applications, including MRI machines, particle accelerators, and magnetic levitation trains.

One promising area of research is the development of high-temperature superconductors (HTS), which have critical temperatures above the boiling point of liquid nitrogen (-196 ^{o}C). These high-temperature superconductors are easier to work with than traditional superconducting materials and could have a wide range of practical applications [13].

Another promising area of research is the development of superconducting materials that can carry high currents. Many superconducting materials are limited in their current-carrying capacity, which makes them impractical for certain applications. Scientists are working to develop new

materials that can carry higher currents, which would make them more practical for applications such as power transmission and energy storage [8,57,86,102].

In addition to these practical applications, superconductivity also has important implications for our understanding of physics. The study of superconductivity has led to many important discoveries in the field of condensed matter physics, and it continues to be an active area of research for scientists around the world.

1.1.2. Critical parameters of a superconductor

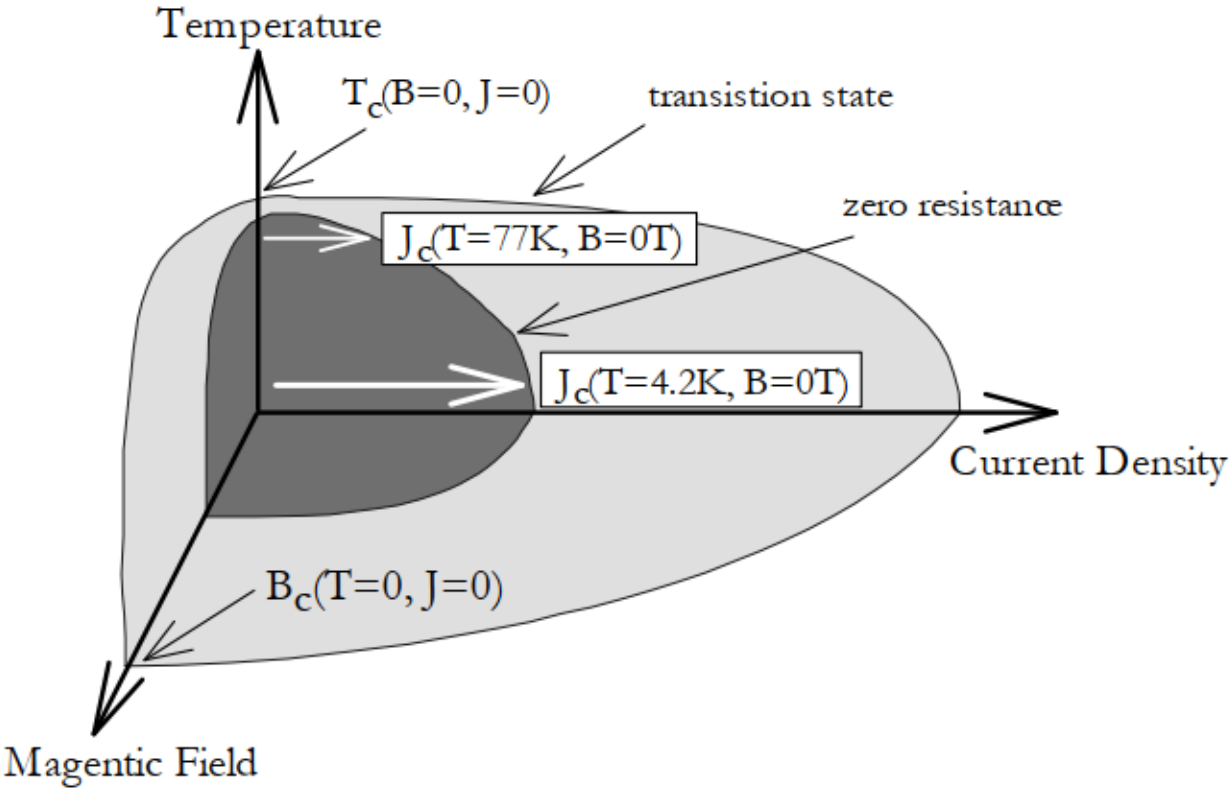

Figure 1.2. Three states of conductivity in a superconductor: zero resistance (inside the innermost surface), transition state (outer surface), and normal conductance (beyond the outer surface) [84].

Superconductors exhibit a lack of electrical resistance and become diamagnetic below a specific temperature before being disrupted by excess external magnetic fields or applied currents. The three parameters that

determine the different states of conductivity for a superconductor are temperature, magnetic field, and current density. When the temperature, magnetic field, and current are below certain critical points, the material is in its superconducting state. In the transition state, the resistivity increases as the temperature, magnetic field, and current density rise. Type I superconductors, which are primarily made up of pure metals, have a sharp transition from superconducting to normal states when subjected to an external magnetic field. Type II superconductors, which are generally alloys and compounds, gradually lose their superconducting properties when an external magnetic field is applied [9]. The transition region between the superconducting and normal states is known as the mixed state, and normal conductance is observed when the resistivity is independent of the magnetic field and current density. Figure 1.2 provides a schematic representation of these different regions.

When any of the critical values for T_c, B_c, or J_c are exceeded, the superconductivity of the material disappears. However, the surface of the zero-resistance space is determined by the combination of these parameters. In Figure 1.2, the white arrows indicate the critical current densities for a temperature near T_c (e.g., 77 K) and a temperature close to absolute zero (e.g., 10 K) in the absence of a magnetic field. For $Bi_2Sr_2Ca_1Cu_2O_{10+\delta}$ thick films, the J_c value increases from 5000 A/cm^2 at 77 K and 0 T to 30,000 A/cm^2 at 10 K [8,86]. The critical temperature T_c of Bi-2212 is 96 K. The mechanical properties of HTS materials cause difficulties during the manufacturing of conductors due to their brittleness and low flexural strength. Without support from a ductile, high-strength matrix or substrate, they cannot be formed into wires or tapes. If the manufacturing process requires temperatures above the solidus temperature of the compounds, silver alloys are the only suitable matrix materials.

1.1.3. Superconductor classification

1.1.3.1. Type-I and type-II superconductors

1.1.3.1.1. Type-I superconductor

Type-I superconductors are a class of materials that exhibit superconductivity when cooled below a certain critical temperature. Type-I superconductors have a single critical field and are characterized by their complete expulsion of magnetic fields.

One of the defining characteristics of type-I superconductors is their critical field, which is the maximum magnetic field that the material can tolerate before it loses its superconducting properties. In type-I superconductors, this critical field is relatively low, typically on the order of a few hundred gauss. This means that these materials are only useful for applications that require relatively weak magnetic fields [9].

Another important characteristic of type-I superconductors is their ability to completely expel magnetic fields from their interior. This is known as the Meissner effect, and it occurs when a superconducting material is placed in a magnetic field. The magnetic field induces a circulating current in the material, which generates an opposing magnetic field that cancels out the external field. This results in a complete expulsion of the magnetic field from the material's interior, which makes type-I superconductors useful for applications such as levitation and magnetic shielding [9].

The Meissner effect is particularly useful for levitation applications, as it allows superconducting materials to float in mid-air above a magnet. This is because the magnetic field of the magnet induces a circulating current in the superconductor, which generates an opposing magnetic field that cancels out the magnetic field of the magnet. This creates a stable levitation effect, which has applications in fields such as transportation and energy storage [60].

While type-I superconductors have many useful properties, they also have some limitations. One of the biggest limitations is their low critical field, which limits their practical applications to those that require relatively weak magnetic fields. Another limitation is their relatively low critical temperature, which means that they must be cooled to extremely low temperatures to exhibit superconductivity. This presents several engineering challenges, as cryogenic cooling systems are complex and expensive to operate.

1.1.3.1.2. Type-II superconductor

Unlike type-I superconductors, which have a single critical field and exhibit complete expulsion of magnetic fields, type-II superconductors have multiple critical fields and exhibit a mixed state of superconductivity and normal conductivity in the presence of a magnetic field.

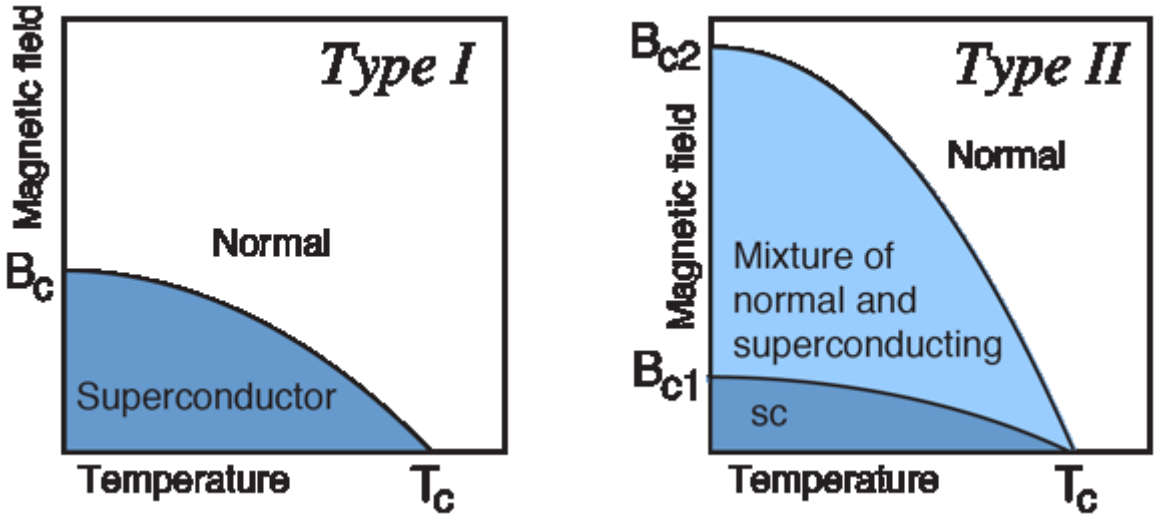

Figure 1.3. Phase diagram of Type-I and Type-II superconductors [84].

One of the defining characteristics of type-II superconductors is their multiple critical fields. In these materials, there are two critical fields: the lower critical field (B_{c1}) and the upper critical field (B_{c2}) as described in Figure 1.3. B_{c1} is the point at which the material begins to transition from the superconducting state to the mixed state, while B_{c2} is the maximum magnetic

field that the material can tolerate before it completely loses its superconducting properties [3,9,26].

In the mixed state, type-II superconductors exhibit a complex behavior known as flux pinning. This occurs when magnetic flux lines become trapped within the material's structure, creating regions of normal conductivity surrounded by regions of superconductivity. These trapped flux lines can become pinned in place by defects in the material's structure, creating a strong resistance to changes in magnetic fields [3,9,26].

While type-II superconductors exhibit more complex behavior than type-I superconductors, they also have some advantages. One of the biggest advantages is their higher critical field, which allows them to tolerate much stronger magnetic fields than type-I superconductors. This makes them useful for applications such as magnetic resonance imaging and high-energy physics experiments.

1.1.3.2. Low-T_c and high-T_c superconductor

1.1.3.2.1. Low-T_c superconductor

It has been widely reported that electrons in a normal metal had the relatively independent interactions with electrons or and with the lattice. Interestingly, these interactions might become dependent under certain conditions. The electrons might indirectly interact with each other via the vibration of lattice called as phonon. Let us make an animation: as the first electron passes through the lattice. Due to the Coulomb interaction, the positive ions of the lattice would be attracted towards the passing electron. The Coulomb attraction, however, was not strong enough to balance the ion bonding, which led to the distortion of positively charged density: the density of positive charges nearby the moving path of the electron would be increased. Consequently, the group of positive charges would generate another Coulomb

interaction to the second electron, attracting electron come to the lattice. By this visualization, the electron potential has been the only factor acting on the electrons, a gradient of which is provided by an electromotive force. As a result, electrons would pass through a conductor without any resistance. A conductor was then called a superconductor. This electron-electron attraction via phonon has been called Cooper Pairing established in the Bardeen-Cooper-Schrieffer theory [9].

The temperature at which the material reached the superconducting state has been found to be absolutely critical for electron bonding. It was clearly shown that the energy of ions of the lattice is required to be so low that the valence electrons stay within their associated atoms, and the lattice vibration was very slight. The requirement led to the fact that the temperature for that energy state was less than 25 K. When it was compared to the temperature of liquid helium (~ 4.2 K), the superconductors whose T_c of less than 25 K were able to work, and were classified as low temperature superconductors (LTS).

1.1.3.2.2. High-T_c superconductor

High-temperature superconductors (HTS) are a class of superconductors with T_c at temperatures above the boiling point of liquid nitrogen. HTS was first discovered in 1986 in a copper-oxide material known as La-Ba-Cu-O with T_c ~ 35 K, and since then, a variety of HTS materials have been discovered [8,86]. This is in high contrast to traditional superconductors with lower T_c, for example, Pb (T_c ~ 7.2 K), (PbTl T_c ~ 4.8 K), or NbN (T_c ~ 16 K).

HTS are exhibited by a low critical field B_{c1} that shows the maximum field where the materials display Meissner effect. Between B_{c1} and the upper critical field B_{c2}, a mixed phase with vortices, that is, normal regions of cylindrical magnetic tubes containing a magnetic flux quantum $\Phi_0 = \hbar/2e$, is formed that order into a hexagonal lattice to minimize interactions. These two

critical fields are determined by two fundamental lengths of the superconducting state, the penetration depth (λ) and the coherence length (ξ), in the following way: $\mu_0 H_{c1} = \Phi_0/2\pi\lambda^2$ and $\mu_0 H_{c2} = \Phi_0/2\pi\xi^2$. HTS are extreme type-II superconductors, that is, the ratio $\kappa = \lambda/\xi$ is very high [14].

Major application researches of HTS have been focused on $YBa_2Cu_3O_{7-\delta}$ (YBCO) with $T_c \sim 92$ K, $Bi_2Sr_2Ca_1Cu_2O_{8+\delta}$ (Bi-2212) with T_c of ~ 85 K, and $Bi_2Sr_2Ca_2Cu_3O_{10+\delta}$ (Bi-2223) with T_c of ~ 110 K. Most of them possess CuO_2 planes, which will be elaborated on shortly. Evidently, these planes play a crucial role in the formation of the superconducting state. Another notable characteristic of high-temperature superconductors (HTS) is the metallic nature of their conductivity within the CuO_2 planes, which is comparable to the conductivity found in certain disordered metallic alloys. HTS crystals exhibit various imperfections, including crystal grains, grain boundaries, twinning, oxygen vacancies, and porosity, all of which exert a detrimental impact on the maximum critical currents [36,74].

Despite these challenges, HTS materials have the potential to revolutionize a variety of applications. One of the most promising areas is power transmission and distribution, where HTS materials can be used to create more efficient and compact electrical systems. HTS materials can also be used in magnetic levitation systems, such as maglev trains, due to their ability to generate strong magnetic fields.

1.2.1. Vortex state in type-II superconductors

1.2.1.1. Typical characteristics of vortices

In type-II superconductors, vortices are a common feature of the mixed state in which the material is partially superconducting and partially normal conducting. Vortices are created when magnetic field lines penetrate the material and become trapped in small areas of normal conductivity, creating a

circulating current around the magnetic field lines. Understanding the behavior of vortices is important for the study and application of type-II superconductors [3,9,26].

Vortices in type-II superconductors are characterized by their size, density, and dynamics. The size of a vortex is typically on the order of the coherence length, which is a measure of the distance over which superconducting properties are maintained. The density of vortices is determined by the strength of the applied magnetic field and the critical field of the material, which is the maximum magnetic field that the material can tolerate while remaining superconducting [3,9,26].

The dynamics of vortices in type-II superconductors are complex and depend on several factors, including temperature, magnetic field strength, and the properties of the material itself. One important factor that affects vortex dynamics is the pinning of vortices, which occurs when the material contains defects or impurities that trap vortices in place. Pinning is important because it can prevent vortices from moving and dissipating energy, which can improve the superconducting properties of the material [14].

Vortices in type-II superconductors can also interact with each other, forming complex patterns and structures. One example of this is the vortex lattice, which occurs when vortices arrange themselves into a regular lattice structure due to the repulsive forces between vortices. The properties of the vortex lattice depend on the strength of the applied magnetic field and the geometry of the sample, and can be studied using a variety of experimental techniques such as neutron scattering and magnetic force microscopy [14,26].

The study of vortices in type-II superconductors has important implications for the development of new superconducting materials and the design of superconducting devices. For example, researchers are working to

develop new materials with improved vortex pinning properties, which can lead to materials that are more efficient and reliable for applications such as energy storage and transmission. Understanding vortex dynamics can also help researchers design superconducting devices that are more resistant to magnetic field fluctuations and other sources of noise.

1.2.1.2. Important role of vortices for enhancements of J_c in type-II superconductors

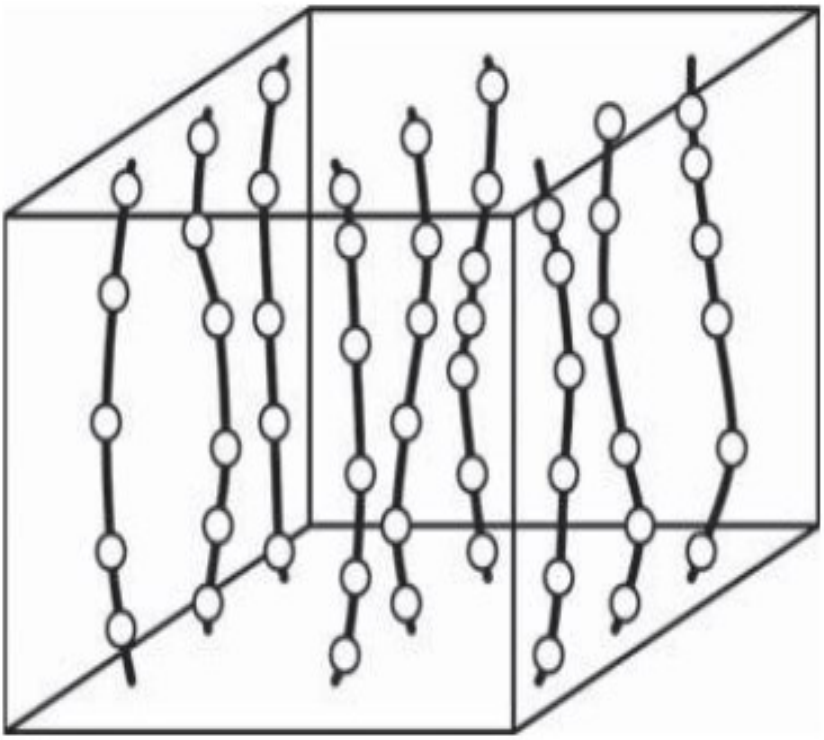

Figure 1.4. Vortices pinning in type-II superconductor [48].

According to Ampere's law: $\nabla \times \vec{B} = \mu_0 \vec{J}$, to increase J_c, the amount of vortex permeating the BSCCO system needs to be increased. In electrical transmission, the Lorentz force appears and acts on the vortices, making them able to move, which leads to the appearance of the resistance and a decrease in its superconductivity [39]. To maintain the superconductivity of the material, a force called as pinning force is needed to balance the Lorentz force, which pins

the vortices and prevents them from moving as Figure 1.4. In recent years, there has been a growing interest in the study of topological vortices, which are vortices that are characterized by their topological properties. These vortices are of particular interest because they are predicted to have exotic properties such as non-Abelian statistics, which could have important applications in quantum computing and other areas of technology.

The study of topological vortices is an active area of research, and researchers are working to identify new materials that can support these types of vortices.

In conclusion, vortices in type-II superconductors are a complex and important feature of these materials. Vortices are created when magnetic field lines penetrate the material and become trapped in areas of normal conductivity, creating a circulating current. Understanding the behavior of vortices is important for the development of new superconducting materials and the design of superconducting devices. The study of vortices in type-II superconductors is an active area of research, and researchers are working to identify new materials and phenomena that can improve the superconducting properties of these materials.

1.2. VORTEX DYNAMICS IN TYPE-II SUPERCONDUCTORS

1.2.1. The collective pinning theory

Collective pinning theory is one of the most useful techniques that have been used to analyze the interaction between penetrated vortices in type-II superconductors. In the light of quantum mechanics, the vortices are a collection of interacting particles, and their interaction is controlled by the collective interaction between them and their surroundings. By using the collective pinning theory, the field dependence of J_c and the flux pinning mechanism in HTS samples would be systematically investigated.

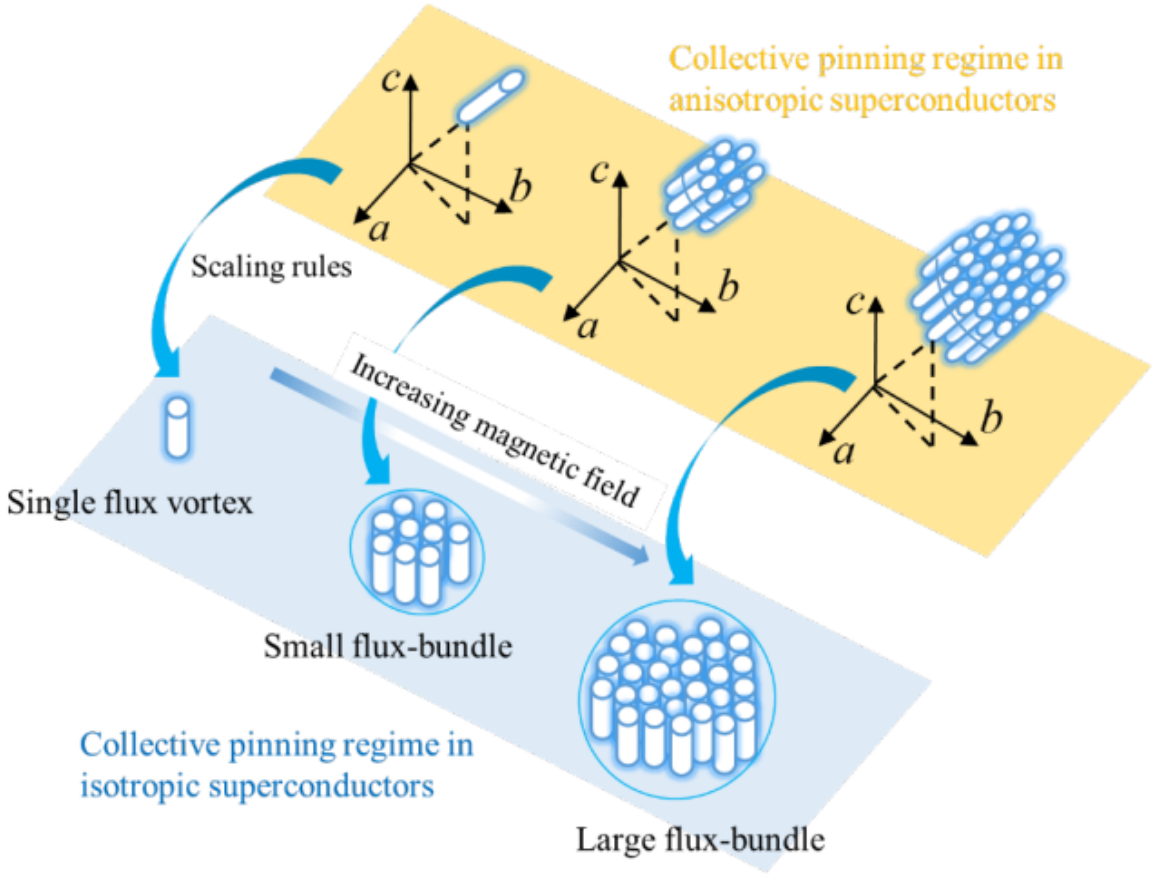

Figure 1.5. Schematic of collective pinning regimes with increasing magnetic field [52].

The basements of the collective pinning theory were first introduced in the 1980s by scientists who were trying to understand the vortex interactions in superconducting materials as randomly distributed defects or impurities were added. It was observed that the penetrated vortices inside type-II superconductors tended to become trapped in small regions of the samples, those form the vortex lattice. The possible origin of the observations was generated by the collective interaction between the vortices and the defects in the materials [3,14,26,50].

Collective pinning theory is then developed based on the assumption that vortices can interact with each other and with the surrounding material through

a variety of mechanisms, such as elastic/plastic deformations, and thermal fluctuations. The theory assumes that collective systems of the vortices were formed, and the underlying physics of the superconductor is governing the vortex interactions. One of the key factors playing an important role in collective pinning theory is the existence of a pinning landscape. In the pinning landscape model, the distribution of defects or impurities inside the superconductors, as well as their interactions, are clearly described. The type of the pinning landscape might affect the vortex interactions. The vortices would be trapped in small regions of the material or freely move. Another important concept in collective pinning theory is the idea of critical current density. Critical current density is the maximum current that a superconductor can carry before it becomes normal conducting. In type-II superconductors, the critical current density is determined by the density of vortices and their interaction with the pinning landscape. By understanding the collective behavior of vortices and their interaction with the pinning landscape, researchers can work to improve the critical current density of superconducting materials. A schematic of collective pinning regimes with increasing field is given in Figure 1.5. Following Blatter *et al.*, J_c is field independent when the applied field (B) is lower than the crossover field B_{sb} of the single vortex pinning regime:

$$B_{sb} = \beta_{sb} \frac{J_{sv}}{J_0} B_{c2} \tag{1.1}$$

where β_{sb} is the coefficient with a value of ≈ 5, $J_0 = 4B_c/3\sqrt{6}\mu_0\lambda$ is depairing current, $B_c = \Phi_0/2\sqrt{2}\pi\lambda\xi$ is the thermodynamic critical field, $B_{c2} = \mu_0\Phi_0/2\pi\xi^2$ is the upper critical field, and J_{sv} is the value of J_c in the single vortex regime, λ and ξ are coherence length and penetration depth and coherence length of a superconductor, respectively, μ_0 is the permeability of

vacuum (μ_0 = 4π×10^{-7} H/m), Φ_0 is the flux quanta (Φ_0 ~ 2.067 × 10^{-15} Wb) [14,27,80].

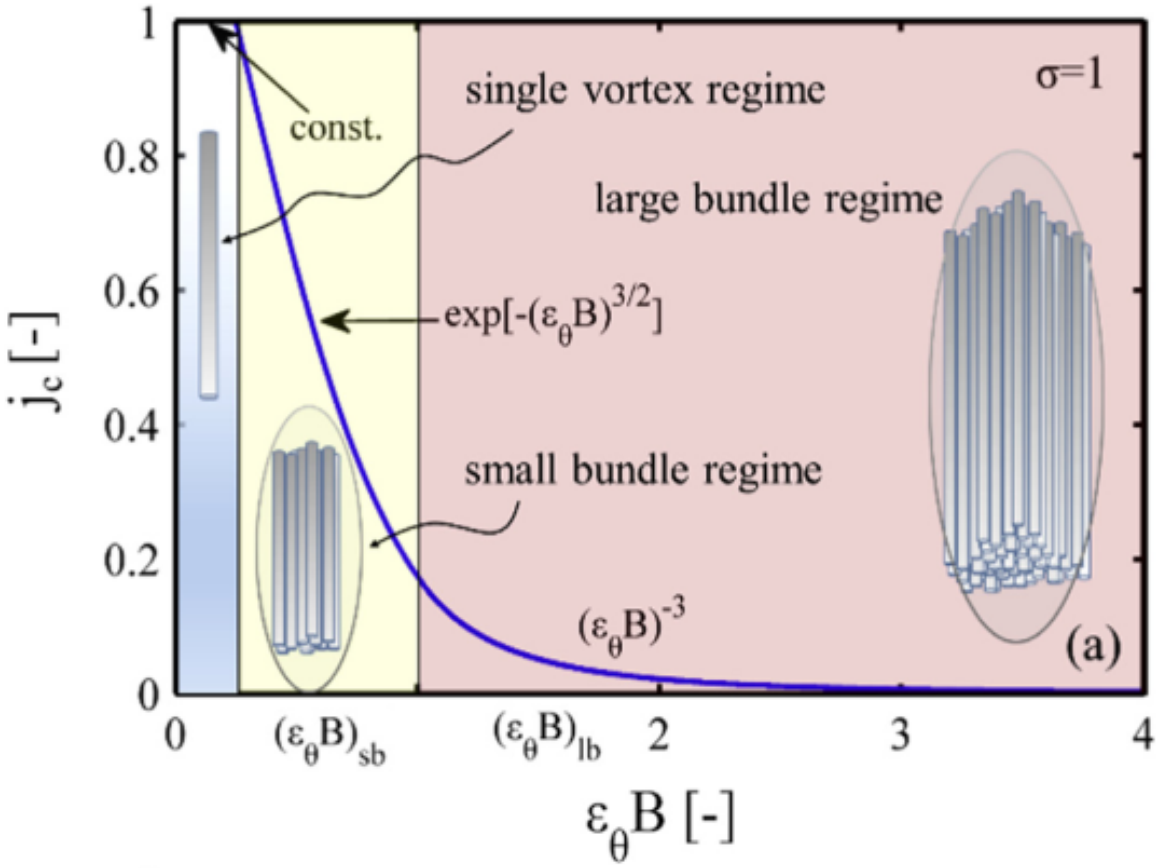

Figure 1.6. The $J_c(B)$ pinning regimes as collective pinning theory [52].

The single vortex pinning regime occurs when there is only one vortex pinned to a single pinning site. In this regime, the pinning force is proportional to the vortex displacement from the pinning site. When $B > B_{sb}$, the small bundle pinning regime occurs with a small number of vortices are pinned together in a small area, forming bundles. In this regime, the pinning force is proportional to the distance between the vortex bundle and the pinning site. J_c in this regime follows an exponential law:

$$J_c = J_c(0).\exp\left[-\left(\frac{B}{B_0}\right)^{3/2}\right], \quad (1.2)$$

where $J_c(0)$ and B_0 were fitting parameters. Collective pinning theory has been used to study a wide range of phenomena in type-II superconductors, including the dynamics of vortices in applied magnetic fields, the effects of thermal fluctuations on vortex motion, and the behavior of vortices in materials with complex pinning landscapes [14,24,25,27,80]. Three separations of different pinning regimes in $J_c(B)$ relation was described in Figure 1.6.

One example of this is the use of artificially created pinning centers, such as nanoparticles or nanoscale defects, to improve the pinning landscape and increase the critical current density of superconducting materials. These pinning centers can be engineered to have specific shapes, sizes, and distributions, allowing researchers to tailor the pinning landscape to the specific needs of a particular application [20,52,75].

The magnetic interaction and the core interaction are the two most significant elementary interactions between vortices and pinning centers in type-II superconductors. In type-II superconductors, the applied field is typically relatively modest, and the magnetic interaction results from the interaction of surfaces between superconducting and non-superconducting materials that are parallel to the applied field. The core interaction results from the coupling of the locally distorted superconducting properties with the periodic modification of the superconducting order parameter. While fluctuations in the charge-carrier mean free path near lattice defects are the primary cause of the pinning type called δl pinning, type of δT_c pinning is induced by the spatial variation of the Ginzburg-Landau coefficient κ (where $\kappa = \lambda/\xi$, which is a theoretical parameter used to classify types of superconductors: $0 < \kappa < \frac{1}{\sqrt{2}}$ for type-I and $\kappa > \frac{1}{\sqrt{2}}$ for type-II superconductors) linked with disorder in the critical temperature T_c [14,24–27,80,106].

Griessen *et al*. derived the corresponding laws for each pinning mechanism in the single vortex pinning regime [24,27,55,80,106], as follows:

For δl pinning

$$J_{sv}(t)/J_c(0)=(1-t^2)^{5/2}(1+t^2)^{-1/2}, \quad (1.3)$$

and for δT_c pinning

$$J_{sv}(t)/J_c(0)=(1-t^2)^{7/6}(1+t^2)^{5/6}. \quad (1.4)$$

Based on the regime separation above, J_{sv} was chosen as J_c at the field of 0.01 T [24,55,106], and t was the normalized temperature ($t=T/T_c$).

In the framework of the collective pinning theory, B_{sb} is correlated to critical current density via relation: $B_{sb} \sim J_{sv}B_{c2}$ [14,80]. Therefore, by inserting Eq. (1.3) and (1.4), Qin *et al.* obtained the expression for the normalized temperature dependence of B_{sb} [80]:

For δl pinning

$$B_{sb}(t)/B_{sb}(0)=[(1-t^2)/(1+t^2)]^{2/3}, \quad (1.5)$$

and for δT_c pinning.

$$B_{sb}(t)/B_{sb}(0)=[(1-t^2)/(1+t^2)]^2, \quad (1.6)$$

In conclusion, collective pinning theory is an important framework for understanding the behavior of vortices in type-II superconductors. By treating the vortices as a collective system and understanding their interaction with the pinning landscape, researchers can gain insights into the behavior of these materials and work to improve their superconducting properties. Collective pinning theory has applications in a wide range of fields, including energy storage, high-field magnets, and quantum computing.

1.2.3. Flux pinning mechanism in type-II superconductor

Expressions for flux-pinning in type-II superconductors are developed from analysis of the geometry of the pinning centers and the interaction between the individual flux lines and the centers. It is shown that the scaling

laws that have been seen in experiments can be obtained without the need to first introduce the idea of flux-lattice elasticity. It has been discovered that predicted pinning functions can adequately explain measured Lorentz force curves in a variety of high value of κ.

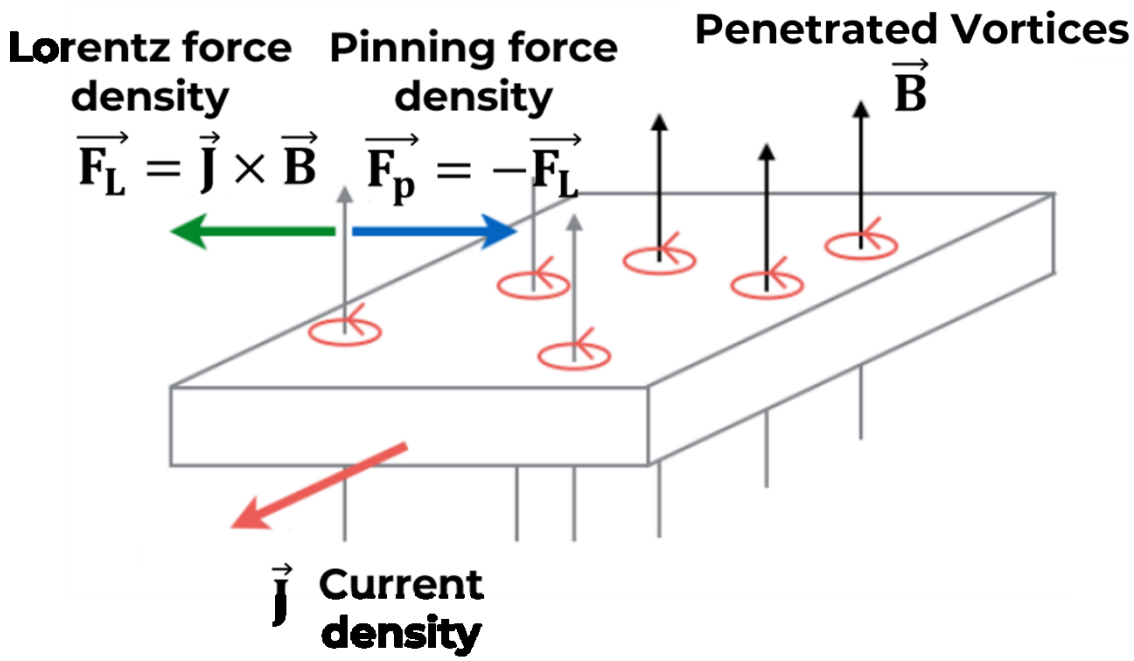

Figure 1.7. Balance of forces acting on vortices [91].

Figure 1.7 describes the balance of forces acting on vortices. When a magnetic field penetrates type II superconductors, an electric field is induced. As a current with current density J is applied to these samples, vortices will be acted by the Lorentz force density, i.e., $\overrightarrow{F_L} = \vec{J} \times \vec{B}$. So, vortices start to flow in the mixed-state region. When flux lines flow, they experience the viscous drag force F_v which opposes this motion i.e., ηV_L inside the medium, where V_L vortex velocity and η are proportionality constant. In the absence of pinning, i.e. when F_L overcomes F_v at higher applied fields, the vortex or flux lines start moving, resistance increases so J_c decreases. To maintain high values of J_c in the high applied fields, vortices should be kept at rest by introducing a pinning force.

This pinning force is induced by the addition of pinning centers or defects that serve as a potential well where the vortices will become pinned. Pinning has been investigated to come from the inhomogeneity in the material. The inhomogeneity might consist of grain boundaries, voids, or impurities. Normal states inside the grain boundary act like pinning centers and prevent vortex motion. So the variety of nanoparticles: insulators, metal, and oxides (both non-magnetic and magnetic) are promising candidates for creating pinning centers [16,20,50].

The performance of magnetic flux pins in type II superconductors was investigated in relation to the nature of the vortices-pin center interactions, as well as the geometrical structure of the magnetic pin centers. The theory is proven through experimental observations on the point of ignoring the model of elasticity of the magnetic vortex network. The obtained magnetic pinning functions have shown the ability to give suitable explanations for the experimental magnetic pinning force density curves on many large κ and strong magnetic pinning systems.

Flux pinning force density is influenced by four factors:

(i) The superconducting nature of the magnetic pin centers, as it is the difference in superconducting parameters between them and the lattice, and determine the strength of the local interaction

(ii) The size and distance (or wavelength) of the micro-pin structure relative to the penetration depth λ of each superconductor, because only if these parameters are greater than λ, the value of B corresponding to the local equilibrium will be obtained

(iii) The size of the magnetic pin centers relative to the magnetic inter-vortex distance, as this can determine the total length of the interaction magnetic vortex and the geometric nature of the interaction

(iv) The stiffness of the magnetic vortex network, as this determines the displacement of the magnetic vortex under the action of a local magnetic pin force is completely elastic, limited by neighboring magnetic vortices, or sufficient magnetic pinning force strong to completely break the vortex network and allow the magnetic vortex to operate independently [20].

1.2.3.1. Types of interaction

If both the size *(a)* and the distance (*l*) of the magnetic pin centers are larger than λ, the magnetic vortices can adjust themselves to reach their equilibrium. This change generates a Bean-Livington potential barrier to the motion of the magnetic vortices at the intersection of the pin center and the superconducting matrix and produces magnetic pinning. This interaction is the magnetic interaction.

In the opposite case, if *a* or *l* is less than λ, magnetic cannot be adjusted to equilibrium. The free energy of the magnetic vortices has a value in the range of the magnetic pin centers that are different from the superconducting matrix, due to the difference in the superconducting parameters. This interaction is the core interaction [20].

1.2.3.2. Types of pinning center

Magnetic vortices interact with the pinning centers because their superconducting parameters are different from those of the superconducting matrix. The strength of the interaction is a function of the magnitude of the difference. Small differences can be expressed through changes in the critical temperature, the critical magnetic field, or the Ginzburg-Landau parameter κ. Large differences can be seen in the case of non-superconducting magnetic pin centers. The biggest difference gives the strongest pinning capacity when the ferromagnetic pin centers are ferromagnetic. Of all the possible cases, there are two main ones that affect magnetic pinning in superconducting materials.

(i) The small difference in κ, which occurs due to changes in resistivity in the normal state due to compositional fluctuations, heterogeneous distribution of lattice defects.

(ii) Non-superconducting particles, which can be common metals, insulators or holes. The magnetic pinning strength of non-superconducting particles does not depend on the nature of these particles. If the non-superconducting metal particles have a path less than or equal to the coherence length of the superconducting material, the binding effect will turn the particles into superconductors, and their presence can lead to a change in the superconductivity. change κ.

As a result, there are two types of magnetic pin centers classified, named as normal and $\Delta\kappa$-type pins [20].

1.2.3.3. Geometries of pinning center

Magnetic pinning centers can be classified based on the number of dimensions larger than the inter-flux-line spacing $d_\phi = 1.07(\phi_0/B)^{1/2}$, where Φ_0 is the flux quanta ($\Phi_0 \sim 2.067 \times 10^{-15}$ Wb) and B is applied field.

Classification of nano-sized pinning centers is presented in Figure 1.8. Point-like pin centers (0D) are regions whose dimensions in all directions are less than d_ϕ. A point magnetic pin center can interact with only one magnetic vortex at a time.

Line (1D) pin centers, such as lattice deflections or needle precipitates, have a length greater than d_ϕ. When lying parallel to the direction of the field, they can interact with a magnetic vortex along their length. When lying at an angle from B, it can interact with some magnetic vortices.

Grain boundaries, double boundaries, stacking errors, plate precipitates, and superconducting material surfaces often have two dimensions larger than

d_ϕ and act as surface (2D) pin centers. They have the strongest pinning ability when the plane is parallel to the direction of the Lorentz force.

Volume pinning centers are all dimensions greater than d_ϕ. The magnetic vortices interact with the surface of the pinning center, and the most important parameter is the scattering cross-section of the surface in the direction of the Lorentz force.

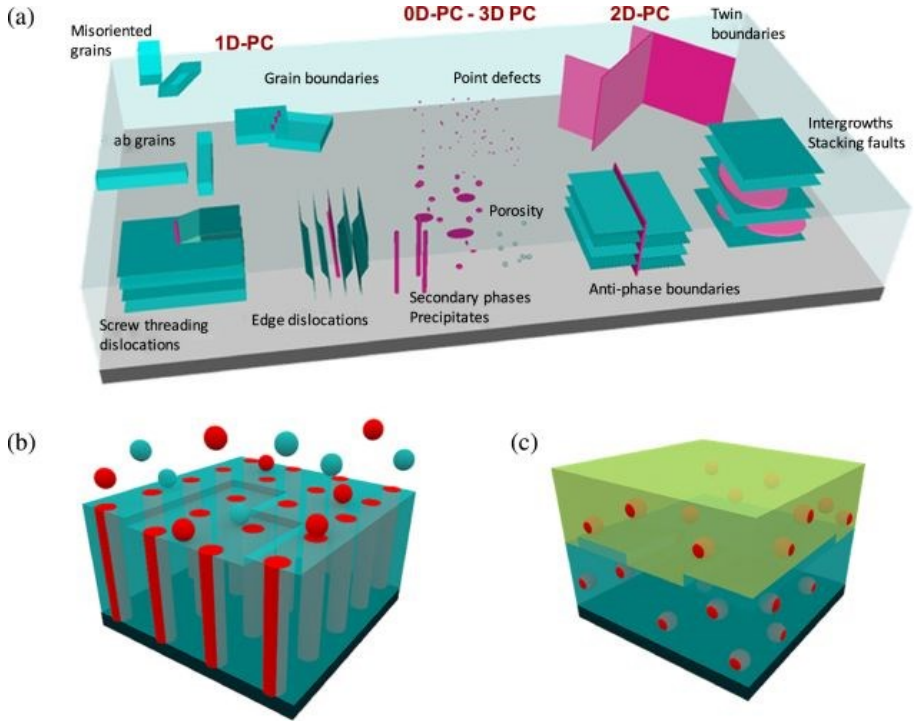

Figure 1.8. Schematic of different types of nano-sized pinning centers in type-II superconductors [75].

One of the most powerful models which has been widely applied to analyze pinning mechanism in type-II superconductors is the Dew-Hughes' model [20]. The normalized flux pinning force density versus normalized field modified function is widely applied:

$$f_p \sim b^p (1-b)^q, \tag{1.7}$$

where, $f_p = F_p/F_{p,max}$ is the normalized pinning force density, $b = B/B_{irr}$ is the normalized field, p and q are fitting parameters used to determine the pinning center properties. The position of maximum F_p, named as b_{peak}, is estimated by $b_{peak} = p/(p + q)$. The all types of pinning centers are summarized in Table 1.1.

Table 1.1. Details of types of pinning properties in type II superconductors [20].

Type of Interaction	Geometry of pin	Type of centre	Pinning function	Pinning parameters	Position of maximum	Max. Const.
Magnetic	Volume	Normal	$Ab^{1/2}(1-b)$	$p = 1/2$	$b_{peak} = 0.33$	A = 2.56
		$\Delta\kappa$	$Bb^{1/2}(1-2b)$	$p = 1/2$	$b_{peak} = 0.16$	B = 0.27
Core	Volume	Normal	$C(1-b)^2$	$p = 0$	-	C = 1.00
		$\Delta\kappa$	$Db(1-b)$	$p = 1$	$b_{peak} = 0.5$	D = 4.00
	Surface	Normal	$Eb^{1/2}(1-b)^2$	$p = 1/2$	$b_{peak} = 0.2$	E = 3.50
		$\Delta\kappa$	$Fb^{3/2}(1-b)$	$p = 3/2$	$b_{peak} = 0.6$	F = 5.37
	Point	Normal	$Gb(1-b)^2$	$p = 1$	$b_{peak} = 0.33$	G = 6.76
		$\Delta\kappa$	$Hb^2(1-b)$	$p = 2$	$b_{peak} = 0.67$	H = 6.76

The flux pinning center classification was summarized in Figure 1.9 by three criteria: vortices-pinning centers interaction, type and geometry of pinning center following Dew-Hughes model.

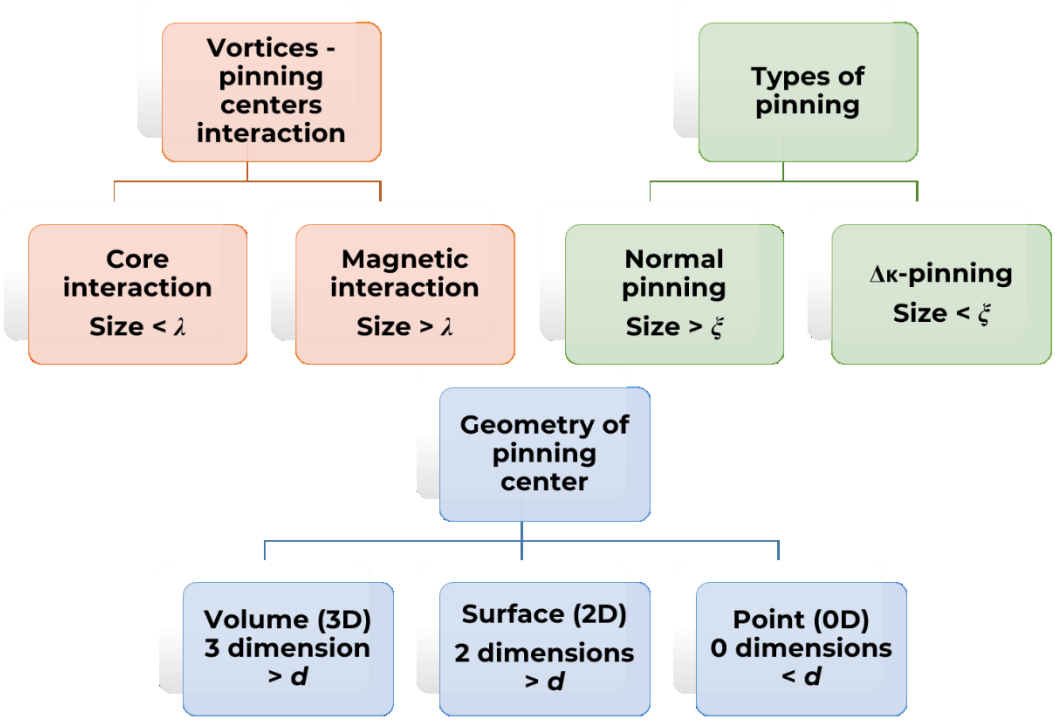

Figure 1.9. Classification of types of pinning centers.

1.3. OVERVIEW ON Bi-Sr-Ca-Cu-O SUPERCONDUCTOR

1.3.1. Crystal structure of Bi-Sr-Ca-Cu-O superconductor

Since 1986, Bi-Sr-Ca-Cu-O (BSCCO) high-temperature superconductor superconductors have been considered to be promising materials for power related and industrial applications [58]. The BSCCO superconductors show advantageous properties, such as relatively simple sample preparation or high T_c, that is well above the liquid nitrogen point (77 K).

All three superconducting phases in the BSCCO superconductor have crystallographic structures with the stoichiometry of $Bi_2Sr_2Ca_{n-1}Cu_nO_{2n+4+\delta}$. The phases have layered structures parallel to the *(ab)* plane as exhibited in Figure 1.10. The major planes are CuO_2 separated by calcium and covered in SrO layers in the c direction. The outer layers are BiO bilayers. Depending on the number of CuO_2 planes, one CuO_2 layer (n = 1) characterizes the 2201

phase, while two and three CuO_2 layers, n = 2 and n = 3, respectively, characterize the 2212 and 2223 phases [86].

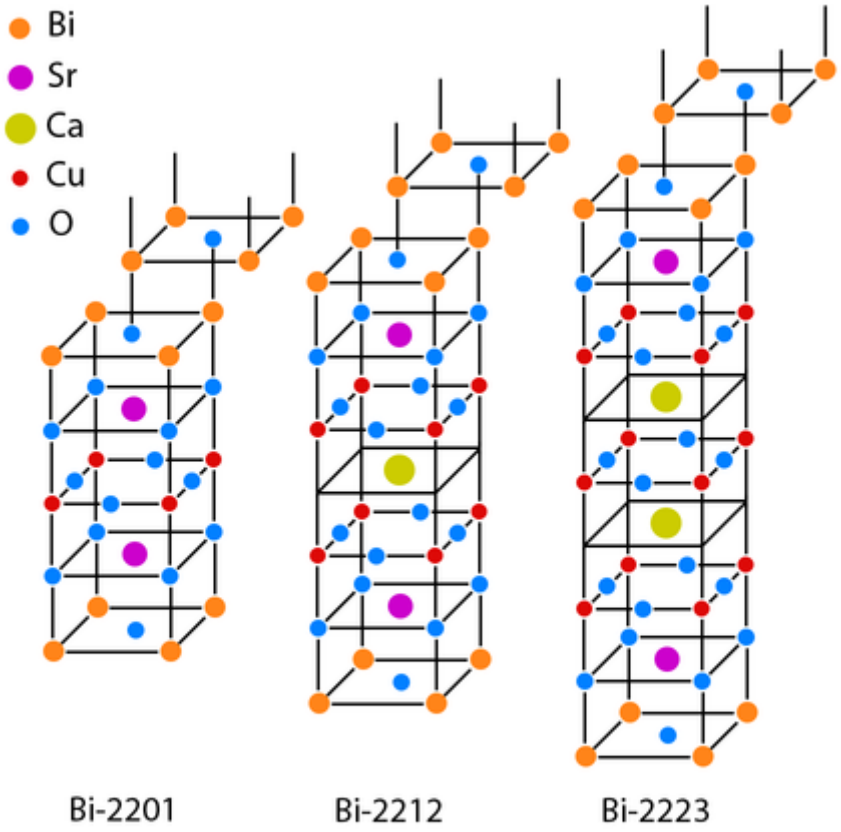

Figure 1.10. Illustration of crystal structures of three phases of BSCCO system [8].

A Bi–O bond length of 0.212 – 0.215 nm and Cu–O bond length of 0.1914 nm. The values of T_c of the Bi-2201, Bi-2212 and Bi-2223 are ~ 20 K, 80 K, and 110 K, respectively [15,42]]. The significant difference between the lattice parameters of *a*, *b* and *c* leads to the crystallization speed in the direction of the *(ab)* plane could be about a thousand times quicker than in the *c*-direction. This structure is the origin of anisotropy of the properties in this

compound, especially, the supercurrent through the Cu–O planes and the critical current density of the superconductor [59].

On the technical side, fabrication of the sample consisting of mainly single Bi-2223 phase is difficult. The Bi-2212 has been found to usually co-exist. In additions, sample fabrication conditions for making Bi-2223 phase requires high sintering temperature ~ 880 – 890 ^{o}C, which might cause more difficulties. Experimentally, the Pb partial substitution accelerates the formation of the Bi-2223 phase. Consequently, the T_c has been improved with a lower sintering temperature to ~ 850 ^{o}C. In this dissertation, the ratio of Bi:Pb was maintained as 1.6:0.4, which was found to be the optimum ratio for obtaining the highest T_c in the Pb-substituted BSCCO systems [62].

1.3.2. Recent studies on the power applications of BSCCO superconductor

1.3.2.1. Studies on BSCCO in the world

Ceramic BSCCO was widely used as the material for the 1st generation HTS cable as in Figure 1.11, besides several HTS such as YBCO, TBCCO, HBCCO [8,86]. YBCO and BSCCO are two types of superconducting materials used for magnetic field applications. YBCO is preferred because it has better flux pinning capabilities. However, BSCCO is considered to be the most technologically useful material and has been more commonly used in bulk applications. BSCCO has also been made into superconducting wires. Multi-filamentary Bi-2223, also called the first generation (1G) HTS material, were fabricated by the traditional powder in tube process with large current capacity, high uniformity, good mechanical properties and the length of over 1000 m can be produced as commercial products. The self-field J_c of ceramic Bi-2223 range from a few hundred to a few thousand A/cm^2 at near liquid nitrogen boiling

temperature. However, the presence of weak link effect and weak natural pinning center lead to a not effective J_c, especially on high field.

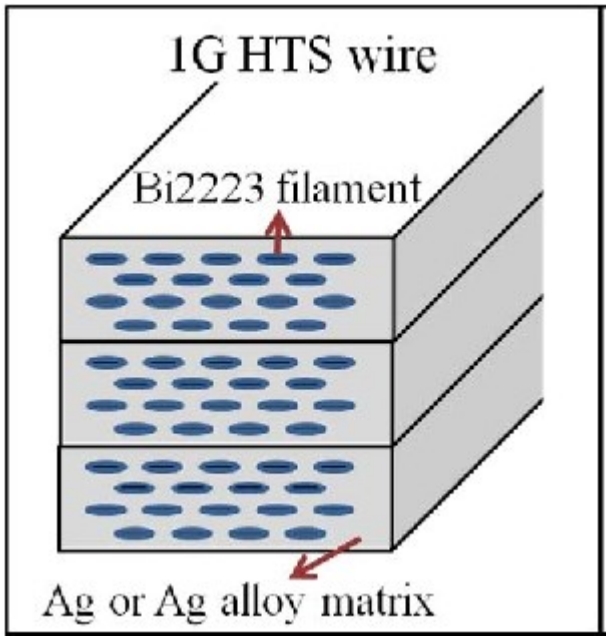

Figure 1.11. BSCCO 1st generation HTS wire [39].

Flux pinning and J_c enhancement are still difficult and need to be addressed to overcome the disadvantaged sides of the material [4,72,73,108,109,111]. Various methods and techniques have been used to produce artificial pinning centers other than the natural centers [45,65,76,111,113,114].

If all four types of geometrical artificial pinning center (APC) have been introduced into HTS films, the flux pinning properties of HTS polycrystals have been shown be clearly improved by the additions of zero-dimensional (0D) and three-dimensional (3D) APCs. Crystal growths in the polycrystalline samples were evidenced to orient in both the (ab) plane and the *c*-axis, which led to the existence of natural grain boundaries with uncontrollable depth. When the substitution/or addition methods were applied, 3D APCs would be expected to stay at grain boundaries of the superconducting crystals.

Recently, substitution effect and nanoparticle addition on Bi-Pb-Sr-Ca-Cu-O (BPSCCO) system has been widely applied to effectively enhance the flux pinning properties and critical current density [6,13,17,23,28,65,104,112–114]. Rare-earth ions have been substituted into Bi-site while alkaline or alkaline earth metals have been provided into reservoir layers, e.i. Ca-site and Sr-site [1,22,73,102,111]. The J_c enhancement was found mostly on these article, so providing motivation to Na-substitution effect study on the dissertation. However, the flux pinning mechanism of the additional APCs has not been fully investigated, which would be performed in the Chapter 3.

Different adequate dopants have been reportedly used as insulator (ZrO_2, MgO), conductor (Al_2O_3), anti-ferromagnetic (Cr_2O_3), or ferromagnetic (Fe_3O_4) nanoparticles [6,17,23,68,69,76,90,104,114]. The nanoparticle characteristics, including non-magnetic or semiconducting characteristics, are significantly different from those of superconductors. Nevertheless, the effects of nanoparticle strongly depend on its fabrication, geometry and especially, magnetism. TiO_2 nanoparticle is one of the most produced ceramic nanoparticles with high stability, simple preparation, and less harmful to human health [29]. The similar semiconducting nanoparticle as SnO_2 nanoparticle was chosen and improved superconducting of (Bi,Pb)-2223 phase [108]. Therefore, TiO_2 nanoparticles can satisfy the ability in industrial manufacture. Besides that, TiO_2 nanoparticle was proved to enhance the critical current density and improve flux pinning properties of high-T_c superconductors in other reports [32,41,51]. Hence, TiO_2 nanoparticle was expected to improve the critical current density and flux pinning properties of BPSCCO superconductor. Following flux pinning mechanism in type-II superconductor, the strength of flux-center interaction is depended on the difference in superconducting properties between the superconductor and pinning centers [16,20]. Therefore,

the strongest pinning center could be suggested to be ferromagnetic centers. There are several publications have pointed out that magnetic nanoparticles have expressed positive influence on BSCCO superconductor [2,19]. Following previous publications, in our experiments, Fe_3O_4 nanoparticles have been chosen as dopant, with average size is around 20 nm. For more details, magnetite nanoparticle with the dimension mentioned above are characterized as ferromagnetic material, which has been known as the strongest pinning type [16,20]. Furthermore, the flux pinning mechanism on nanoparticle addition is also required to investigated, which could lead to nanoparticle selection on the further research on this field.

Hence, the substitutions and nanoparticles addtion could be effective for $Bi_{1.6}Pb_{0.4}Sr_2Ca_2Cu_3O_{10+\delta}$ materials and require systematic investigations.

1.3.2.2. Studies on BSCCO in Vietnam

In Vietnam, the study of superconducting physics has been and is an important research area in the field of physics and materials science, which is evident in the formation of specialties/laboratory research in magnetism and superconductivity at universities and research institutes. The Department of Low Temperature Physics (formerly known as Cryogenics Laboratory) at the Faculty of Physics of VNU University of Science began researching HTS in the late 1970s, shortly after the discovery of YBCO. Over time, other organizations such as the Institute of Materials Science (Vietnam Academy of Science and Technology) and the International Training Institute of Materials Science (ITIMS - Hanoi University of Science and Technology) also began to focus on HTS. By the end of the 20th century, these groups had reported a series of positive results. In order to produce a BSCCO sample with a high phase fraction of Bi-2223, it is necessary to subject the sample to a high temperature of around 880-890 ^oC for a duration of approximately 168 hours. However,

researches during this period have indicated that the necessary temperature for this heat treatment can be lowered to around 850 ^{o}C by partially substituting Pb for Bi at an optimal ratio of Bi:Pb = 0.6:0.4.

Since 2014, the research group led by Dr. Duc Hai Tran, in collaboration with Dr. Nguyen Khac Man (International Training Institute for Materials Science), at the Department of Low Temperature Physics, University of Science, Vietnam National University has focused on improving the J_c and H_c of BPSCCO ceramics and MgB_2 thin films. The research has been carried out on the basis of a combination of domestic and foreign research groups. The group has achieved many high-rated publications on prestigious journals in recent years [78,95,96].

1.4. MOTIVATION OF THE DISSERTATION

Based on the above analyses, along with the limitations of the BPSCCO system, the dissertation aims to investigate the microscopic flux pinning properties of the BPSCCO superconductors through the manipulation of pinning center addition effects. If most of the previous studies were temporarily focused on the overall enhancements of J_c in the BPSCCO bulk and film samples at single measurement temperatures (mostly at 10 K or 20 K), so the applications of theoretical models to investigate the microscopic pinning parameters were not fully performed. The dissertation will go deeper in studying temperature and field dependences of J_c and pinning force (F_p) by using theoretical models such as collective pinning theory, Dew-Hughes model… to extract the microscopic pinning related parameters. The measurement temperature will be scanned from 25 K, 35 K, 45 K, 55 K, 65 K and the applied field will be ranged from 0 T to 7 T. Since the pinning effectiveness has been proved to be strongly depended on the average size of pinning centers (d) with the condition: coherence length (ξ) < d < penetration

depth (λ), types of pinning centers with increased average size are separately added to the samples. The following issues are going to be addressed:

- Additions of point-like pinning centers (pinning centers having the smallest sizes) into $Bi_{1.6}Pb_{0.4}Sr_2Ca_2Cu_3O_{10+\delta}$ samples by substitutions of alkali metal. The theoretical models of collective pinning and flux pinning mechanism will be applied to investigate enhancements of J_c as well as the additional pinning/pinning dominant in the substituted samples. The geometry of additional pinning centers will be identified by the Dew-Hughes model.

- Addition of non-magnetic nanoparticles (pinning centers whose larger average size compared to that of the point-like pinning) into $Bi_{1.6}Pb_{0.4}Sr_2Ca_2Cu_3O_{10+\delta}$ samples. The influence of non-magnetic nanoparticles on crystal structure, local structure and critical properties will be investigated systematically. The decrease of T_c related to the variation in local structure and was investigated by Aslamazov-Larkin model and XANES analysis. The effect of nanoparticles served as pinning centers on flux pinning mechanism of the fabricated samples will be examined. The geometry of additional pinning centers will be identified by the Dew-Hughes model.

- Addition of magnetic nanoparticles (developed from the non-magnetic nanoparticles with multiple effective pinning properties) into $Bi_{1.6}Pb_{0.4}Sr_2Ca_2Cu_3O_{10+\delta}$ samples. The influence of ferromagnetic nanoparticles on crystal structure and critical properties of the superconductor system will be investigated. The geometry of additional pinning centers will be identified by the Dew-Hughes model. The pinning potential will be presented as more confident evidence for magnetic dopant on the J_c and flux pinning enhancement.

- Comparison of the separated effects of additions of nano-structured pinning centers on the improvements of J_c and flux pinning properties of

$Bi_{1.6}Pb_{0.4}Sr_2Ca_2Cu_3O_{10+\delta}$ samples. The possiblly optimum conditions for the highest improvement of J_c would be concluded.

CHAPTER 2: EXPERIMENTS

2.1. SAMPLE FABRICATIONS

2.1.1 Fabrication of Bi-Pb-Sr-Ca-Cu-O polycrystalline samples

The sample of stoichiometry of $Bi_{1.6}Pb_{0.4}Sr_2Ca_2Cu_3O_{10+\delta}$ were prepared by the conventional solid-state reaction technique. The first step involved the preparation of the appropriate amounts of 99.9% pure Bi_2O_3, PbO, $SrCO_3$, $CaCO_3$, and CuO powders for $Bi_{1.6}Pb_{0.4}Sr_2Ca_2Cu_3O_{10+\delta}$ samples. The powders were mixed, ground, pelletized, and calcinated in four stages. At every stage, the mixture was sintered in air at 670 ^oC, 750 ^oC, 800 ^oC, and 820 ^oC for 48 hours, respectively, with intermediate grinding and pelleting processes. Finally, the compound was calcinated at 850 ^oC for 168 hours, then free cooled in air.

2.1.2. Fabrication of nanoparticles

2.1.2.1. The Titanium dioxide nanoparticle

Semiconducting TiO_2 nanoparticles were prepared by the hydrothermal route. $TiCl_4$ solution was slowly added to the diluted H_2SO_4 (10 %) solution at 0◦C. The mixed solution was heated at 70 ^oC for an hour. After that, concentrated NH_4OH was slowly added to gain a pH of ~ 7 solution, and then the precipitate was formed. The obtained precipitate was filtered and washed with distilled water. Following that, the precipitate was heated at 220 ^oC for 24 hours. Finally, the precipitate was filtered and dried in air at 120 ^oC for 24 hours.

2.1.2.2. The Iron(II,III) oxide nanoparticle

Fe_3O_4 nanoparticles were synthesized by the chemical co-precipitation route from $FeCl_2$ and $FeCl_3$ salts. The mixed solution was vigorously stirred at 800 cycles/min and remaining at 70°C until the addition of NH_4OH 28% initiated a black-colored precipitate. The nanoparticles were purified through magnetic separation using ethanol and distilled water several times to remove

residual chemicals. The samples were finally dispersed in ethanol. The nanoparticles were dried before used as the dopant.

2.1.3. Introductions of pinning centers into Bi-Pb-Sr-Ca-Cu-O polycrystalline samples

2.1.3.1. The sodium substitution

Polycrystalline superconducting $Bi_{1.6}Pb_{0.4}Sr_2Ca_{2-x}Na_xCu_3O_{10+\delta}$ samples with x = 0.00, 0.02, 0.04, 0.06, 0.08, and 0.10 were prepared by the conventional solid-state reaction method with appropriate amounts of Bi_2O_3, PbO, Sr_2O_3, $CaCO_3$, Na_2CO_3, and CuO high-purity powders. All sample preparation steps followed the 2.1.1.

2.1.3.2. The non-magnetic and magnetic nanoparticle additions

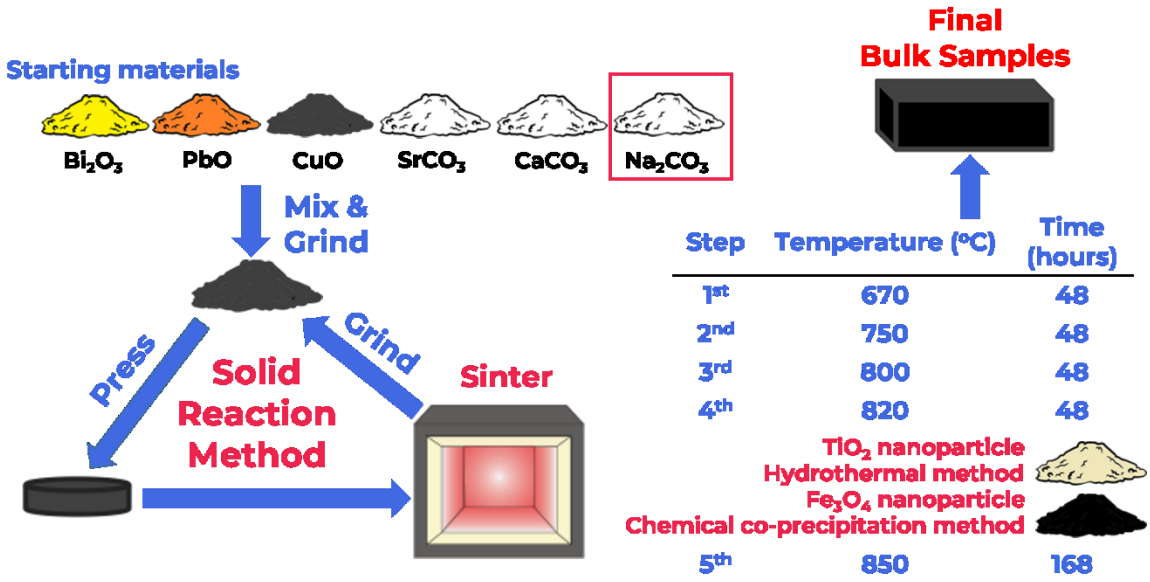

Figure 2.1. Fabrication process of sample series illustration.

The TiO_2 nanoparticles were independently prepared with 12 nm in average diameter and high purity. After the 820 °C stage, the resulting compound was thoroughly mixed with the TiO_2 at appropriate proportions. Finally, all samples were ground, pelleted, and sintered at 850 °C for 168 h. All

samples were freely cooled to room temperature in air. The sample stoichiometry was $(Bi_{1.6}Pb_{0.4}Sr_2Ca_2Cu_3O_{10+\delta})_{1-x}(TiO_2)_x$.

The additions of Fe_3O_4 nanoparticles (an average diameter of ~ 15 nm) to BPSCCO samples were carried out by using the same methods those applied to the additions of TiO_2. The sample stoichiometry was $(Bi_{1.6}Pb_{0.4}Sr_2Ca_2Cu_3O_{10+\delta})_{1-x}(Fe_3O_4)_x$.

So, there were 3 series of the polycrystalline samples. The completed fabrication process was illustrated in Figure 2.1.

2.2. SAMPLE CHARACTERIZATIONS

2.2.1. Crystal structure analyses

2.2.1.1. Transmission electron microscopy

Transmission Electron Microscopy (TEM) is a powerful analytical technique that has ability to investigate the nano-materials. TEMs utilize a high-voltage electron beam to generate images. At the outset of a TEM, an electron gun situated at its apex emits electrons, which traverse the microscope's vacuum tube. In contrast to light microscopes that employ glass lenses to focus light, TEMs utilize electromagnetic lenses to concentrate electrons into a precise beam. This focused electron beam subsequently traverses an exceedingly thin specimen, where the electrons either disperse or strike a fluorescent screen located at the microscope's base. As a result, an image of the specimen emerges on the screen, revealing its various components, each depicted in distinct shades determined by its density. The nanoparticles morphology in the dissertation were investigated by JEOL JEM-2100, Institute of Materials Science , Vietnam Academy of Science and Technology.

2.2.1.2. Xray diffraction measurement

X-ray diffraction (XRD) is a technique used to study the crystal structure of materials. When a beam of X-rays is directed at a crystalline material, the X-

rays interact with the atoms in the crystal lattice, causing them to diffract, or scatter, the X-rays in different directions. The pattern of scattered X-rays can be detected and analyzed to determine the arrangement of atoms in the crystal lattice. The general relationship between the wavelength of the incident X-rays, angle of incidence and spacing between the crystal lattice planes of atoms is known as Bragg's Law and illustrated in Figure 2.2:

$$n\lambda_{\mathrm{Cu-K}\alpha} = 2d_{hkl}sin(\theta), \quad (2.1)$$

where n is the reflection order, $\lambda_{Cu\text{-}K\alpha}$ is the radiation wavelength, d_{hkl} is the interplanar spacing of the crystal and θ is the angle of incidence.

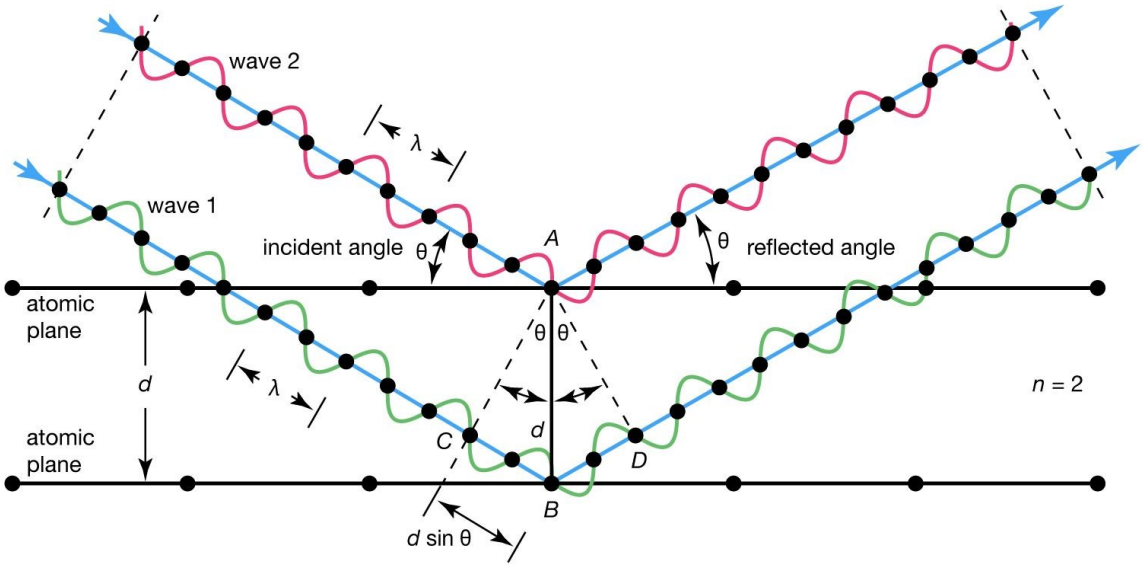

Figure 2.2. Bragg's Law reflection [115].

The XRD patterns of the samples were investigated from 10° to 70° of 2θ using Bruker D8 Advance model using Cu–Kα radiation at Faculty of Physics, VNU University of Science, with wavelength $\lambda_{\mathrm{Cu\text{-}K}\alpha}$ = 1.5418 Å. The measured XRD data was treat following steps, including background determination, profile fitting and refined by Rietveld refinement method. The phase identification was defined using Inorganic Crystal Structure Database (ICSD) and Crystallography Open Database (COD) [100].

The crystallite size has been calculated using Scherrer's formula:

$$\tau = \frac{0.9\lambda_{Cu-K\alpha}}{B.cos\theta}, \quad (2.2)$$

where τ is crystallite size, $\lambda_{\text{Cu-K}\alpha}$ is Cu-Kα wavelength, B is the full width at half maximum (FWHM) and θ is the diffraction angle of the XRD peak.

The lattice constants of BPSCCO cells were calculated as a tetragonal structure using Bragg's law and Miller's indices:

$$\frac{1}{d_{\text{hkl}}^2} = \frac{4}{3}\left(\frac{h^2+h.k+k^2}{a^2}\right) + \frac{l^2}{c^2}, \quad (2.3)$$

where h, k, l are Miller's indices and a, b, c are lattice constants.

2.2.1.3. Scanning electron microscopy

Scanning electron microscopy (SEM) is a powerful imaging technique that uses a beam of high-energy electrons to scan the surface of a sample and create a detailed image of its morphology. The surface morphology of the samples was examined using Nova NanoSEM 450 at Faculty of Physics, VNU University of Science. A beam of electrons with 500 V is focused onto the surface of a sample and causes the emission of secondary electrons and backscattered electrons. The detector in the system collects and amplifies these backscattered electrons signals, which are then processed to generate 5000 times magnification image of the sample surface.

2.2.1.4. Xray Absorption spectroscopy

X-ray absorption spectroscopy (XAS) is a powerful analytical technique used to study the local structure of materials. In XAS, a sample is exposed to a beam of X-rays of varying energies, and the absorption of the X-rays by the sample is measured as a function of the energy of the X-rays. X-rays are a type of electromagnetic radiation that could ionize atoms by exciting their core electrons to an excited state or to the continuum above the ionization threshold

as in Figure 2.3. The excited state is a vacant energy level below the ionization threshold. Each core electron has its own unique binding energy [67].

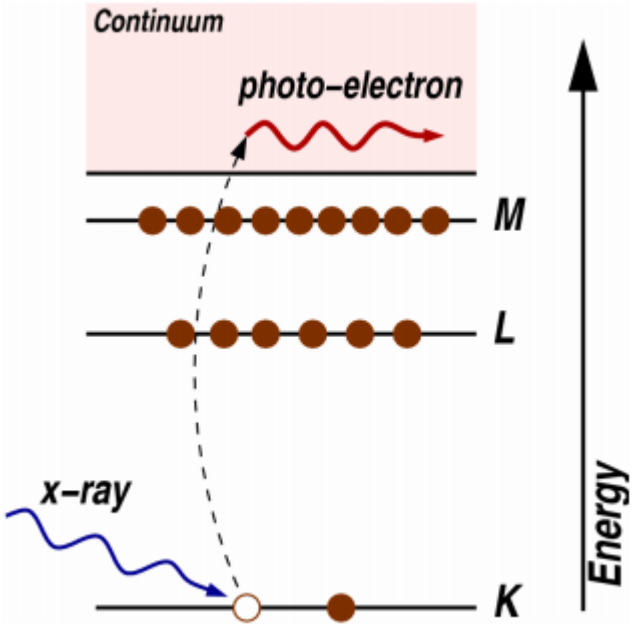

Figure 2.3. The photoelectric effect, in which an x-ray is absorbed and a core level electron is promoted out of the atom [67].

As previously mentioned, when an X-ray photon is absorbed by a core electron, it creates a space in the core shell known as a core hole. These core holes are highly energetic and unstable due to their electronegativity. Their average lifespan is approximately one femtosecond. There are two processes by which a core hole can be created: X-ray absorption, where a core electron absorbs the X-ray photon, or X-ray Raman scattering, where a core electron absorbs part of the X-ray photon's kinetic energy. The decay of a core hole occurs through either the ejection of an Auger electron or X-ray fluorescence. When X-ray radiation moves through the binding energy range of a core shell, there is a sudden rise in absorption that corresponds to the X-ray photon being absorbed by a specific type of core electrons. The absorption edges are named after the principal quantum number, n, of the excited electrons. By analyzing

the energies of the absorption edges in X-ray absorption spectra, it is possible to determine the identity of the absorbing elements [67].

XAS can be performed in two modes: X-ray absorption near-edge structure (XANES) and extended X-ray absorption fine structure (EXAFS). In XANES, the X-ray energy is varied near an absorption edge of a specific element, providing information about the electronic transitions that occur near that edge. The XANES measurement at Cu and Ti K-edge was operated at the Beamline 8 (BL8) Synchrotron Light Research Institute, Thailand using an electron energy of 1.2 GeV and beam current of 80–150 mA at room temperature. The XANES measurements of Cu $L_{2,3}$-edge were performed on BL11A at Photon Factory, KEK, Tsukuba, Japan.

2.2.2. Superconducting property analyses

2.2.2.1. Resistivity vs. temperature measurement

A four-probe measurement system with close-cycle liquid helium is a setup used to measure electrical resistance in materials at low temperatures. The resistance is examined based on Ohm's law:

$$R = \frac{U}{I}. \quad (2.4)$$

It consists of four electrical probes that are arranged in a specific configuration, usually in a square or rectangular pattern. The sample to be tested is placed in the center of this configuration. The measurement is performed by passing a 10 mA electrical current through the outer two probes and measuring the voltage drop across the inner two probes. This allows for the determination of the electrical resistance of the sample.

Close-cycle liquid helium is used to cool the sample and the probes to extremely low temperatures in a 10^{-3} mbar vacuum cabinet. This is necessary because at higher temperatures, thermal energy can disrupt the electrical

resistance measurements. The close-cycle system circulates helium gas in a closed loop to continuously cool the sample and probes, without the need for a continuous supply of liquid helium. The helium compressor is the CTI CRYOGENICS 8200 from Oxford. The temperature reduction process is controlled by CRYOCON 32B to regulate the helium compression process from the Cryodriver pump. The measurements were performed at ITIMS – Hanoi University of Science and Technology.

2.2.2.2. Magnetization vs. field measurement

The magnetization of the fabricated samples was measured by using a magnetic property measurement system (MPMS) and Physical Property Measurement System (PPMS) systems. For the MPMS at Department of Physics - Sungkyunkwan University, temperature can be varied continuously between 2 K and 400 K, while a magnetic field of up to ± 5 Tesla can be applied. The heart of MPMS is SQUID sensor, which able to resolve magnetization changes of less than 10^{-8} emu. A Physical Property Measurement System (PPMS) is a versatile laboratory instrument used for measuring a wide range of physical properties of materials at various temperatures and magnetic fields. The PPMS is a cryogen-free system, which means it does not require the use of liquid helium. The PPMS consists of a cryostat, a superconducting magnet, and various measurement probes and accessories. The cryostat is used to cool the sample to low temperatures, and the superconducting magnet is used to generate high magnetic fields. The measurement probes and accessories are used to measure various physical properties of the sample.

The sample was mounted onto in the center of a sample holder using non-magnetic sample tube. The system can measure the magnetization curve at low temperatures down to 65 K, 55 K, 45 K, 35 K and 25 K and high magnetic fields up to ± 7 Tesla applied perpendicular to the samples' surface. The critical

current density (J_c) was calculated from magnetization hysteresis (M−H) loop using Bean's critical state model.

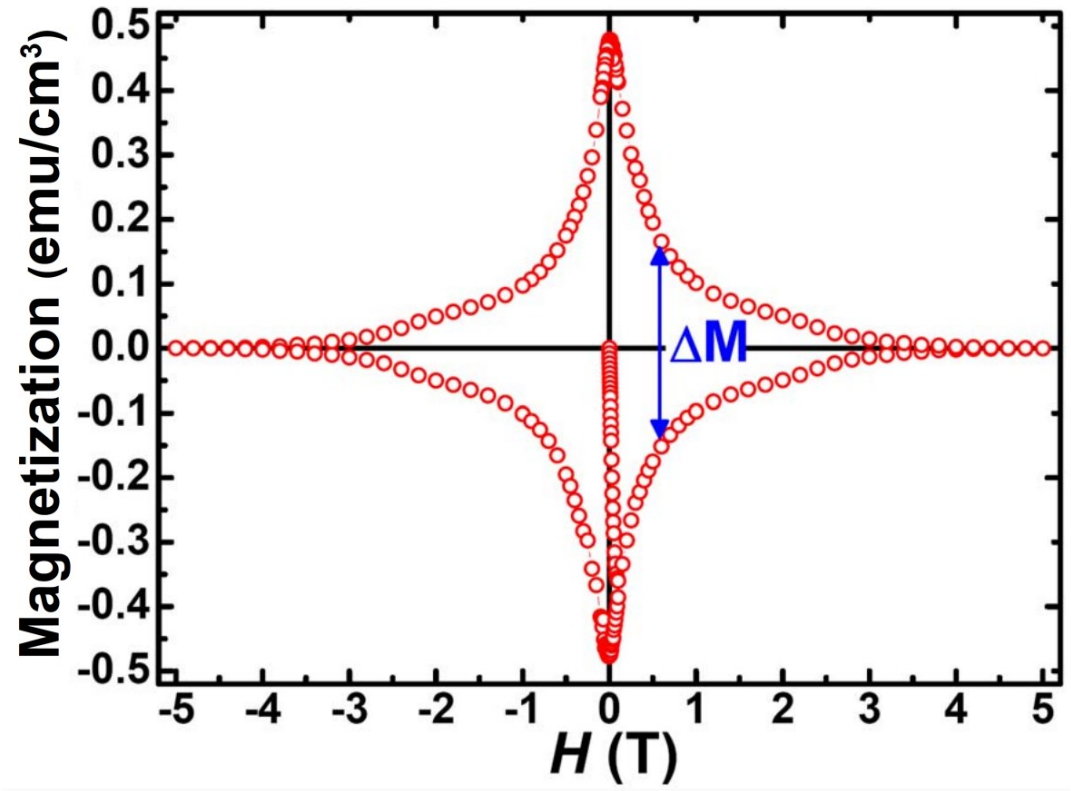

Figure 2.4. Illustration of estimation of *ΔM* from a hysteresis loop of a BPSCCO sample measured at 65 K.

According to this model, each filament in the sponge carries either its critical current or no current at all. When an external magnetic field is applied, surface barrier current shields the inner filaments from the field. The field can only penetrate when the surface barrier current reaches its critical value. As the field is increased, filaments closer to the center start carrying the critical current, until the flux has penetrated to the center of the sample. When the field is reduced to zero, current flows in all the filaments, and the flux becomes trapped in the sample. Applying a field in the opposite direction, the critical current in the filaments progressively reverses. By using the Ampere's law:

$\vec{\nabla}_{\times}\vec{B} = \mu_0\overrightarrow{J_c}$ and the magnetic flux density expression: $B = \frac{1}{V}\int Hdv$, the Bean's formula was defined to proportion with $\Delta M = M^{+} - M^{-}$is the width of hysteresis loop [10]. For the rectangular bulk samples, the Bean's model has been modified as:

$$J_c = \frac{20\Delta M}{a\left(1-\frac{a}{3b}\right)}, \tag{2.5}$$

where *a* and *b* are the sample dimensions perpendicular to the magnetic field. The M^{+}, M^{-}, and ΔM practical estimation was described in Figure 2.4.

CHAPTER 3: IMPROVEMENTS OF CRITICAL CURRENT DENSITY IN HIGH-T_c $Bi_{1.6}Pb_{0.4}Sr_2Ca_2Cu_3O_{10+\delta}$ SUPERCONDUCTOR BY USING SODIUM SUBSTITUTION EFFECT

As presented in Chapter 2, there have been 3 series of polycrystalline samples. The effect of additions of pinning centers whose the smallest averaged size on $Bi_{1.6}Pb_{0.4}Sr_2Ca_2Cu_3O_{10+\delta}$ samples are going to discuss in this chapter. For substitution effect, Na was partially substituted into Ca site in BPSCCO crystal structure based on the two advantages. Firstly, two elements are similar in chemical properties (Na is the alkali metal and Ca is alkaline earth metals). Secondly, the small difference in ionic radii between Na^{1+} (0.95 Å) and Ca^{2+} (1.00 Å), which led to the high probability of substitution of Na^{1+} to Ca^{2+} and point-like defects would be generated. In this chapter, effect of Na-substitution on crystal structure and improvements of J_c in in BPSCCO sample will be studied. Polycrystalline superconducting $Bi_{1.6}Pb_{0.4}Sr_2Ca_{2-x}Na_xCu_3O_{10+\delta}$ samples were denoted as Na000 (x = 0), Na002 (x = 0.02), Na004 (x = 0.04), Na006 (x = 0.06), Na008 (x = 0.08), and Na010 (x = 0.10), respectively.

3.1. FORMATION OF THE SUPERCONDUCTING PHASES

In Figure 3.1, XRD patterns of the pure and Na-substituted BPSCCO samples are provided. It would be seen that two main superconducting phases have been formed: high-T_c (Bi-2223) and low-T_c (Bi-2212) phases. For the Na000 sample, volume fraction of Bi-2223 (%Bi-2223) is ~ 72.08% and that of Bi-2212 (%Bi-2212) is ~ 27.92%. For Na-substituted samples, %Bi-2223 is increased to 75.86% in sample Na004, but then decreased to 72.45% in sample Na010. Conversely, the %Bi-2212 is decreased to 24.14% in sample Na004, but then increased to 29.35% in sample Na010. The results might reveal the fact that that the substitution of Na accelerate the formation of the Bi-2223 phase until x = 0.04.

Table 3.1. Variations of volume fractions and lattice parameters for Bi-2223 phase of $Bi_{1.6}Pb_{0.4}Sr_2Ca_{2-x}Na_xCu_3O_{10+\delta}$ samples [95].

Sample	Volume fractions (%)		*a* (Å)	*b* (Å)	*c* (Å)
	% Bi-2223	% Bi-2212			
Na000	72.08	27.92	5,398 ± 0.007	5,427 ± 0.007	37,10 ± 0.01
Na002	73.06	26.94	5,397 ± 0.007	5,427 ± 0.007	37,09 ± 0.01
Na004	75.86	24.14	5,398 ± 0.007	5,426 ± 0.007	37,09 ± 0.01
Na006	74.85	27.15	5,397 ± 0.007	5,427 ± 0.007	37,08 ± 0.01
Na008	74.05	28.95	5,397 ± 0.007	5,426 ± 0.007	37,07 ± 0.01
Na010	72.45	29.35	5,399 ± 0.007	5,426 ± 0.007	37,07 ± 0.01

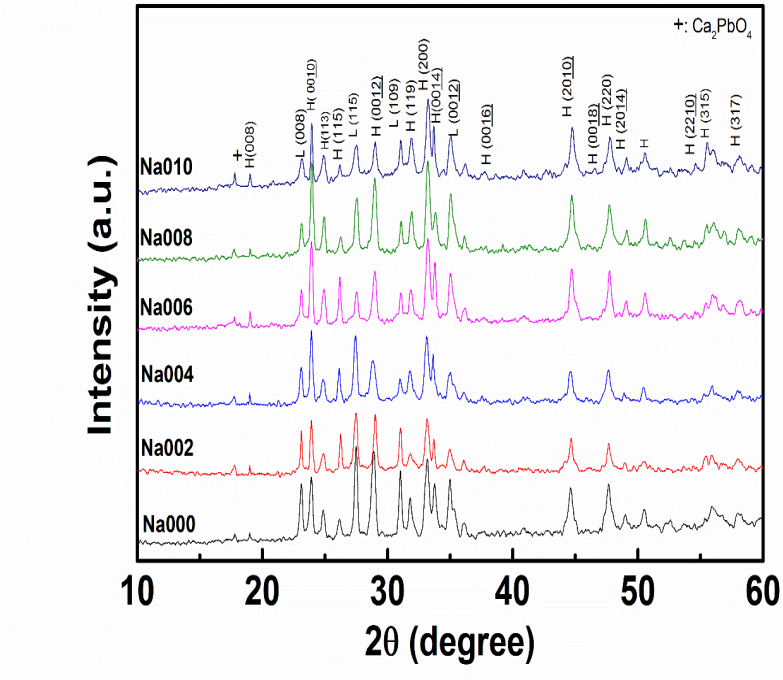

Figure 3.1. XRD patterns of $Bi_{1.6}Pb_{0.4}Sr_2Ca_{2-x}Na_xCu_3O_{10+\delta}$ samples [95].

Lattice constants for the Bi-2223 phase of all samples are also calculated and listed in Table 3.1. As Na^+ was partially substituted into the Ca-site, the values of the lattice constants a and b are found to remain nearly unchanged, while the lattice constant *c* is slightly reduced.

3.2. IMPROVEMENTS OF J_c

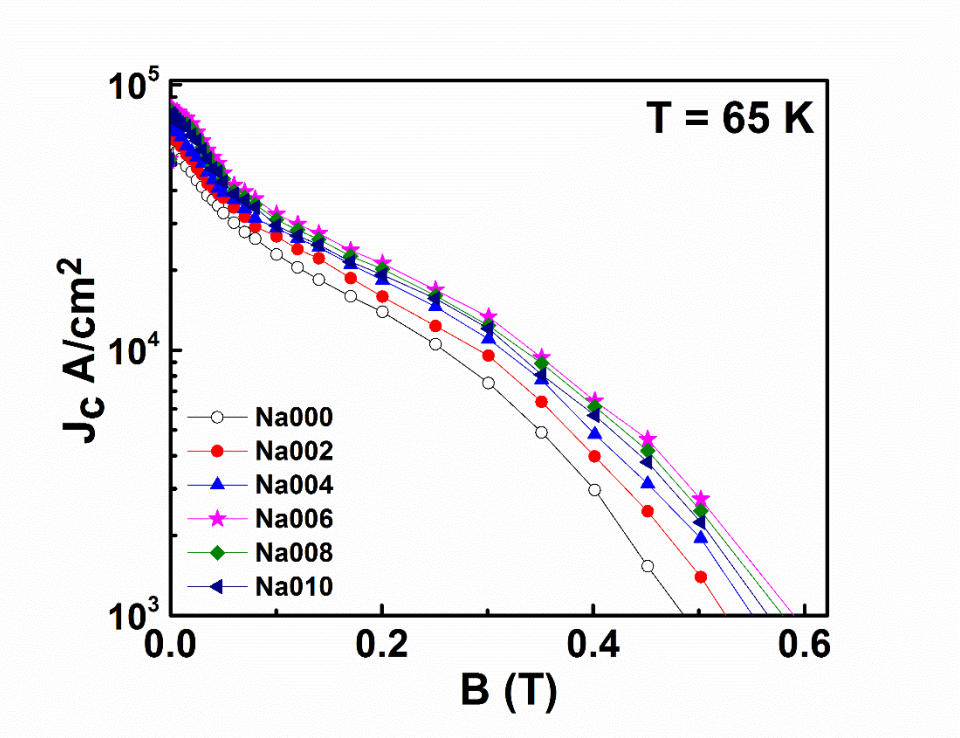

Figure 3.2. Field dependence of J_c at 65 K for $Bi_{1.6}Pb_{0.4}Sr_2Ca_{2-x}Na_xCu_3O_{10+\delta}$ samples in which enhancements of J_c were observed [95].

Field dependence of J_c at 65 K of the fabricated samples are given in Figure 3.2. It would be clearly seen that the enhancements of J_c are obtained in all Na-substituted samples. Among them, the highest enhancement of J_c is reached for Na006 sample. To gain deeper understanding of effects of the Na substitutions on BPSCCO, the magnetic field dependences of J_c for pure and Na-substituted samples at different temperatures ranged between 65 K and 25 K was investigated. The three-dimensional plot of $J_c(B, T)$ for two selected samples - Na000 and Na006 - were exhibited in Figure 3.3 In both samples, the

values of J_c of both Na000 and Na006 samples were increased as decreasing temperature from 65 K to 25 K. The results also showed that the J_c enhancement in the Na006 sample was observed at all investigated temperatures.

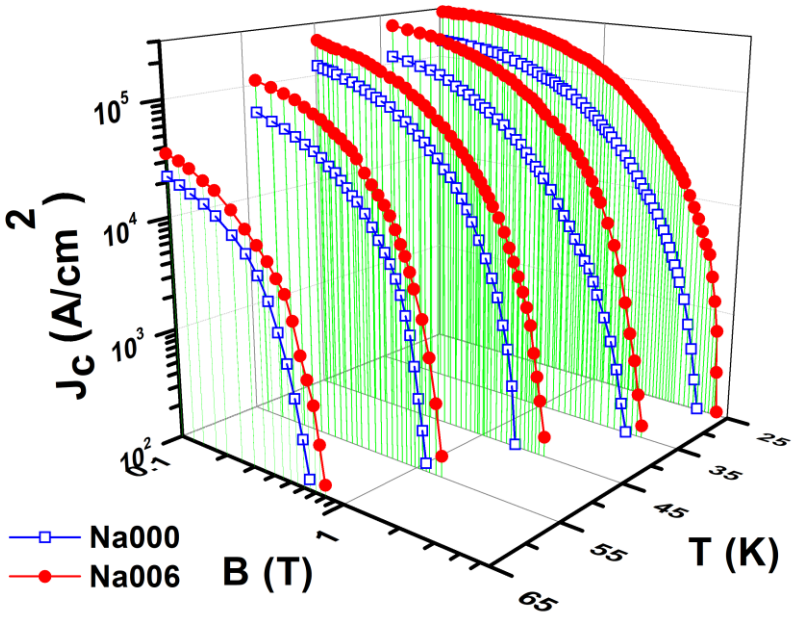

Figure 3.3. Field dependence of J_c of the Na000 and Na006 samples at different temperatures.

In the context of polycrystalline superconductors, it was observed that disorders and pinning sites were not correlated. The BPSCCO system falls into the category of layered structure superconductors, exhibiting anisotropic properties [71]. In this system, vortices were described as an array of two-dimensional pancakes connected by Josephson vortices [12,18]. To explain the magnetic field dependence of the J_c in HTS, the collective pinning theory has proven to be a valuable model [62,73,94].

Originally, the collective pinning theory was developed for isotropic superconductors. However, for anisotropic superconductors like YBCO or BSCCO, it was found to hold when the applied magnetic field was parallel to

the c-axis of the samples [73]. Under these conditions, the anisotropy parameter became irrelevant, and the planar J_c was shown to be independent of the angle between the applied field direction and the ab-plane. This theory has been successfully applied experimentally to polycrystalline MgB_2 and YBCO superconductors [62,94].

Inspired by these studies, we applied this model to analyze the pinning characteristics of BPSCCO superconductors. The magnetic field dependence of J_c for both pure and Na-substituted samples was investigated at three selected temperatures: 65 K, 45 K, and 25 K, and the results were plotted in a double-logarithmic scale in Figure 3.4. In general, all samples exhibited a decrease in J_c as the magnetic field increased.

Starting from a field strength of 0.01 T, the $J_c(B)$ could be divided into three regions, separated by the small bundle field B_{sb} and the large bundle field B_{lb} [14,52]. The first region occurred when applied fields were below B_{sb}, dominated by the single vortex pinning mechanism, resulting in a nearly plateau region for J_c [14,18,21]. The second region was observed when applied fields exceeded B_{sb}, transitioning from single vortex pinning to small bundle pinning, leading to a noticeable decrease in J_c [21,46]. The field dependence of J_c in this region was well-matched with an exponential law (Equation 1.2, provided in 1.2.1). The solid line in Figure 3.4(a-c) represents the best fit to the experimental data. The third region was identified when applied fields exceeded B_{lb}, causing a significant drop in J_c due to thermal fluctuation effects [14].

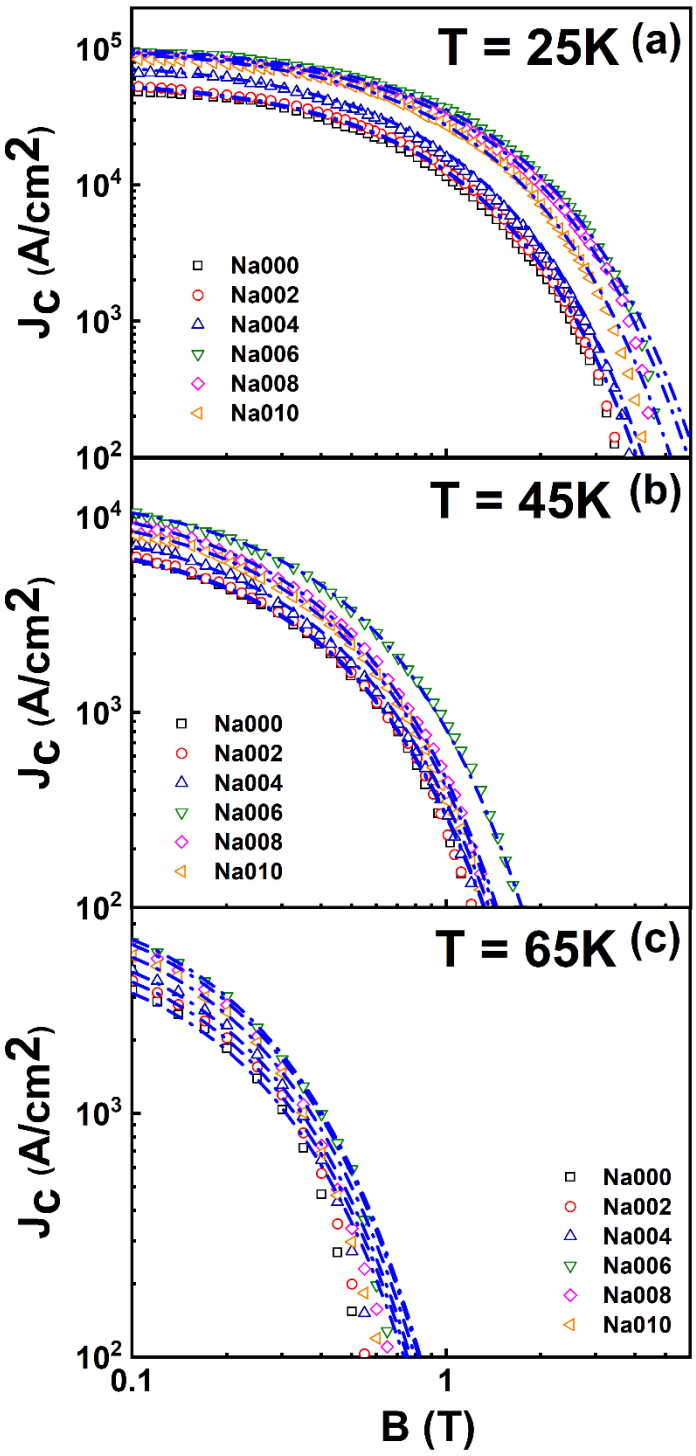

Figure 3.4. Descriptions of the field dependence of J_c of all samples by using the collective pinning theory at (a) 65 K, (b) 45 K and (c) 25 K. The solid lines are the fitting curves using Eq. (1.2).

At the specified temperatures of 25 K, 45 K, and 65 K, the J_c exhibited a non-monotonic trend for the Na-substituted samples. Specifically, J_c showed an increase from Na002, peaked at Na006, and subsequently decreased for Na008 and Na010 samples. The relatively lower enhancements in J_c for Na008 and Na010 samples can be attributed to a deterioration in inter-grain connectivity and an increase in porosity [73].

In the context of the collective pinning theory, a qualitative explanation for the enhancements in J_c can be understood by examining the expansion of both the single vortex pinning and small bundle pinning regimes, as indicated by an increase in the values of B_{sb} and B_{lb}. Figure 3.5(a) illustrates the -ln($J_c(B)/J_c(0)$) vs. field for two selected samples, Na000 and Na006, at 65 K. In the high-field region, these experimental data displayed a linear form, indicating the presence of the small bundle pinning region [25,106]. The values of B_{sb} and B_{lb} were determined based on the points at which the experimental data deviated from this linear trend.

Additionally, the B_{irr} values for all samples were determined from Figure 3.4 using a criterion of J_c=100 A/cm^2 [24]. These obtained data could be fitted by using the equation [25,38]:

$$B_{irr}(t) = B_{irr}(0)\left(1-\frac{T}{T_c}\right)^{3/2}, \qquad (3.1)$$

where $B_{irr}(0)$ was considered as a fitting parameter. The exhibition was shown in Figure 3.5(b) as solid lines. These observations suggested the significant influence of substantial flux creep, aligning with findings reported in prior studies [25,105].

The obtained values of B_{sb}, B_{lb} and B_{irr} values for the two chosen samples, Na000 and Na006, across all examined temperatures, were used to create the B-T diagrams, as depicted in Figure 3.5(c-d), respectively.

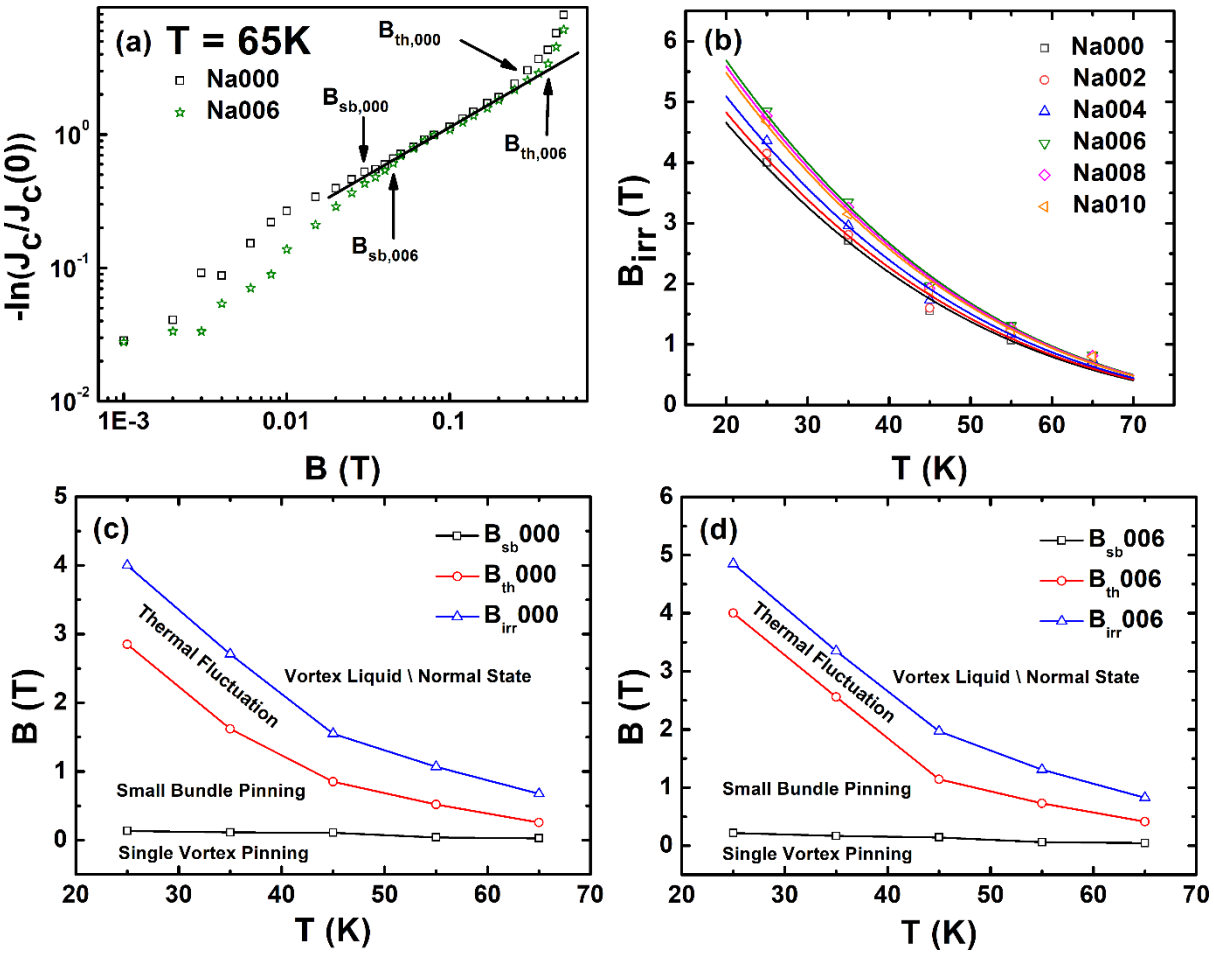

Figure 3.5. (a) Field dependence of -ln($J_c(B)/J_c(0)$) of Na000 and Na006 samples at 65 K. (b) The temperature dependence of B_{irr} of all samples at different temperatures. The solid lines are the fitting curves using Eq. (3.1). (c) The B-T phase diagram of Na000 sample. (d) The B-T phase diagram of Na006 sample.

The various characteristic fields exhibited significant temperature-dependent behavior. The B-T diagrams were categorized into four distinct regions. In the $B < B_{sb}$ region, single vortex pinning was the dominant mechanism, vortex motion displayed elasticity, and the relaxation rate was relatively low. As we moved to the $B_{sb} < B < B_{lb}$ region, the pinning mechanism shifted to small bundle pinning, vortex motion became more plastic, and the

relaxation rate increased significantly. Within the $B_{lb} < B < B_{irr}$ region, the large bundle regime prevailed. Beyond B_{irr}, the vortex state transitioned into a liquid state, vortex motion became notably mobile, and superconducting current ceased, leading to the normal state [25].

In comparison, the Na006 sample exhibited more extensive single vortex pinning and small bundle pinning regions compared to the Na000 sample. These expansions in the regions of single vortex pinning and small bundle pinning could be attributed to the improvements in flux pinning properties in the Na006 sample resulting from Na substitution. Additionally, the large bundle regime was restricted in the Na006 sample, leading to a reduced transformation into vortex liquid state [25].

3.3. FLUX PINNING PROPERTIES

3.3.1. Improvements of pinning force density

To gain a deeper understanding of the reasons behind the J_c enhancements in the Na-substituted BPSCCO samples, we analyzed the behavior of the pinning force density F_p concerning the magnetic field. F_p was graphed against the reduced field (b), where $b = B/B_{irr}$, at temperatures ranging from 65 K to 25 K. These graphs are depicted in Figure 3.6. There are two crucial aspects highlighting the strength of pinning that deserve attention. First, the values of F_p for the Na-substituted samples exhibited significant improvements at all temperatures, with the most substantial enhancements observed in the Na006 sample. Second, the position of the maximum pinning force density ($F_{p,max}$) shifted towards higher values of b for the Na-substituted samples. These two observable features provide strong evidence for the enhanced pinning strength in the Na-substituted samples [44,93]. The source of these improvements is likely associated with the creation of point-like defects, which act as effective pinning centers [95].

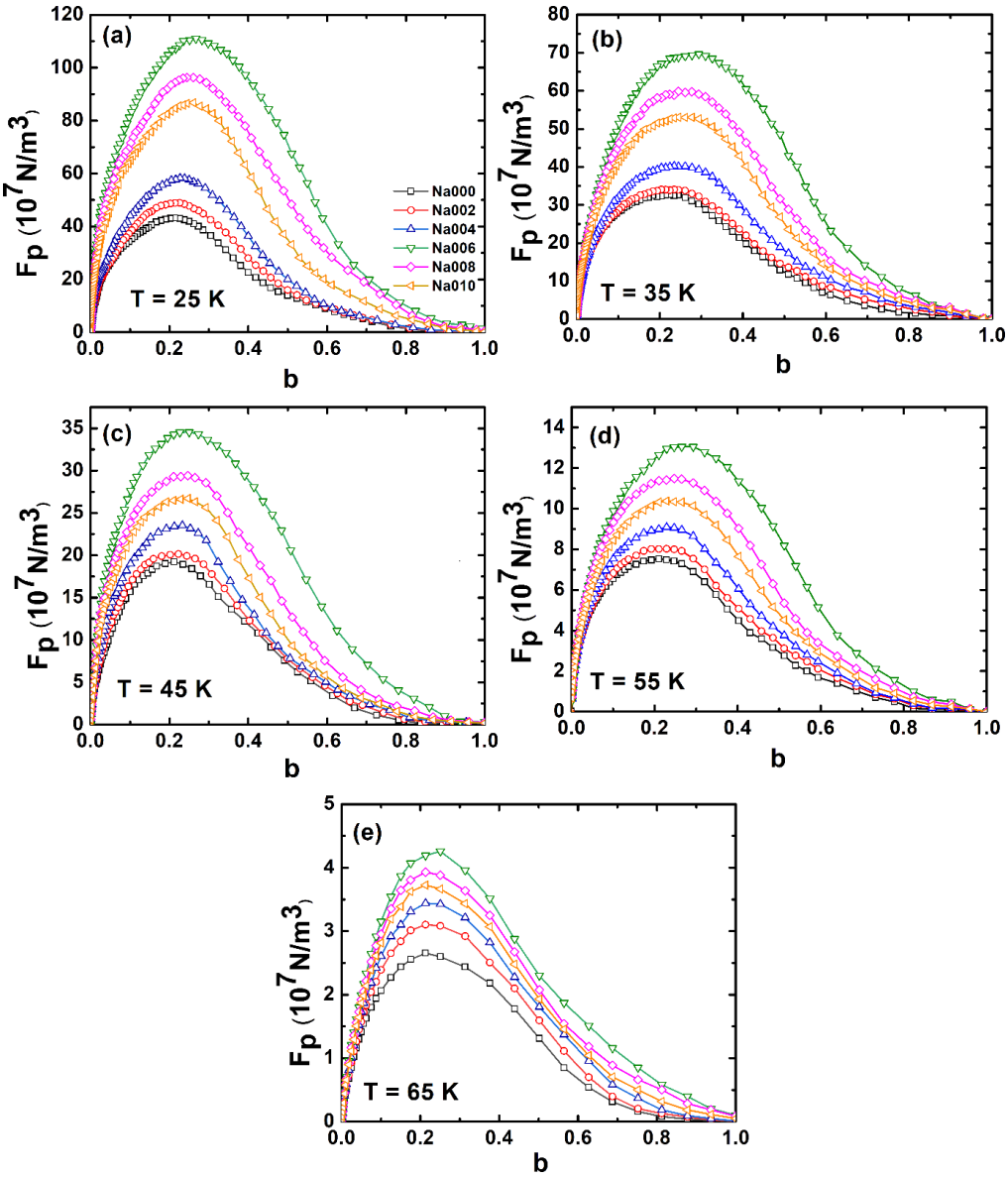

Figure 3.6. Pinning force density (F_p) versus reduced field (b) of the samples at (a) 65 K, (b) 55 K, (c) 45 K, (d) 35 K and (e) 25 K.

Although the pinning strength increased as the temperature decreased, it is important to examine the temperature dependence of the flux pinning mechanism. Figure 3.7 illustrates double-logarithmic plots depicting the variation of $F_{p,max}$ versus B_{irr} at temperatures of 65 K, 55 K, 45 K, 35 K, and 25 K, respectively, while considering Na content as a hidden variable. All the data points were successfully fitted onto single straight lines.

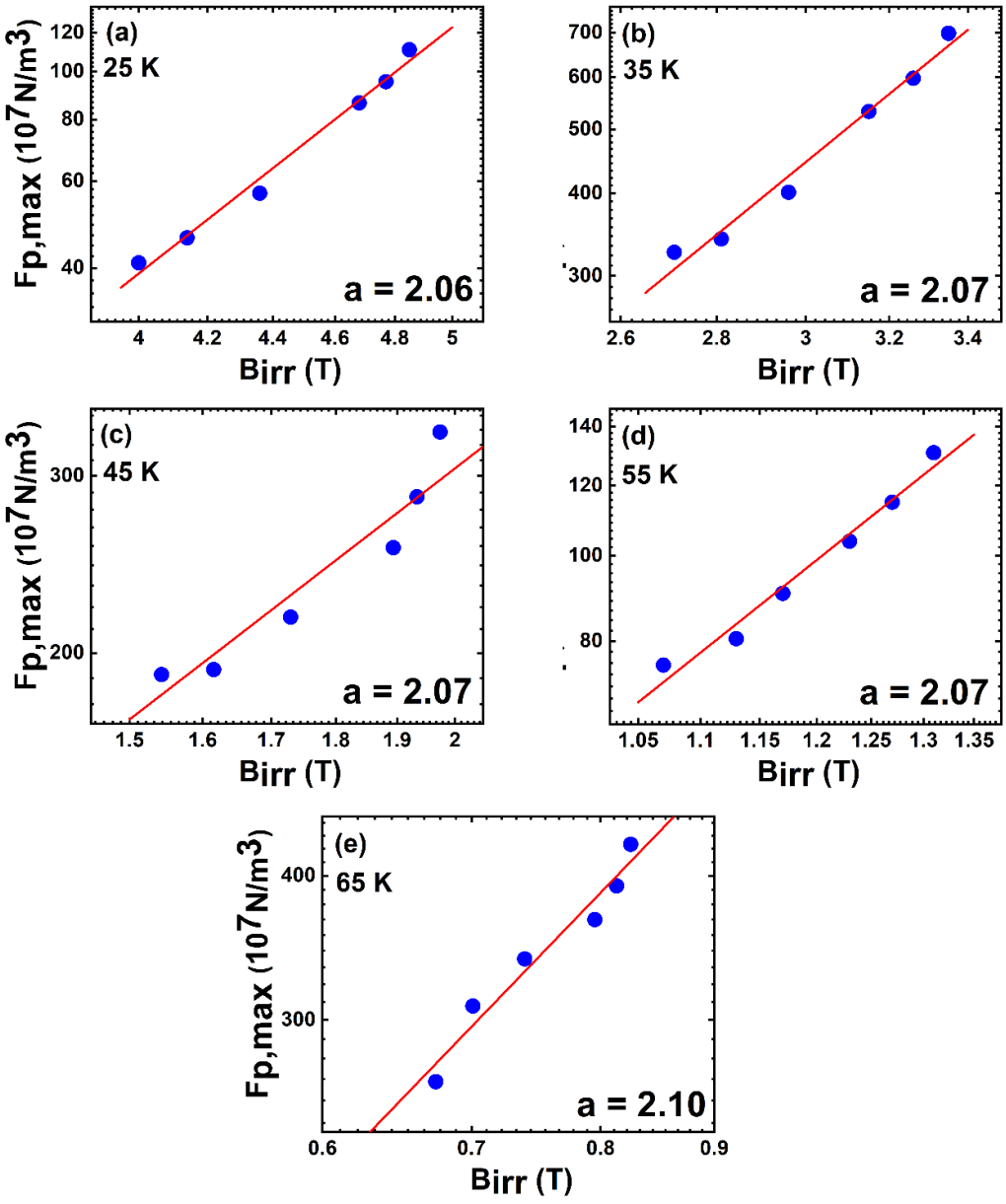

Figure 3.7. The relation between the pinning force density maximum $F_{p,max}$ and irreversible field B_{irr} with Na content as the hidden variable. Data are shown in double-logarithmic plots.

These plots effectively describe the temperature scaling relationship of $F_{p,max} \sim B_{irr}^{\alpha}$ [38,101]. The slopes of these straight lines for all samples were found to be nearly constant, with an exponent value of $\alpha = 2.0 \pm 0.1$. This α

value is comparable to that observed in NbN films and 3d-transition-metal (Fe, Co, and Ni)-doped Y-Ba-Cu-O bulks and films [38,93,105]. These analyses suggest that the predominant pinning mechanism in all samples remains independent of temperature.

3.3.2. Identification of flux pinning type

In the quest to understand the fundamental pinning mechanism of superconductors, the use of f_p versus b plots has become a common approach [20,43,93,101]. Figure 3.8 displays such plots for all the samples, and the average values of p, q, and b_{peak} for each sample can be found in Table 3.2. Notably, for each sample, the experimental data at different temperatures, ranging from 65 K to 25 K, were aptly fitted with a single curve. This suggests that each sample predominantly exhibited a single pinning mechanism, a notion supported by the consistent relationship observed between $F_{p,max}$ and B_{irr} at various temperatures, as depicted in Figure 3.7.

For the Na000 sample, the values of p and q were determined to be 0.49 and 1.77, respectively. It is evident that these values gradually increased with higher Na content (x). The Na006 sample exhibited the maximum p and q values, measuring 0.70 and 1.92, respectively. In contrast, for the Na008 and Na010 samples, p and q values were observed to decrease. These findings align with SEM analyses conducted in prior research. These analyses revealed a degradation in inter-grain connectivity in the surface morphology of the Na008 and Na010 samples [95]. This observation suggests that grain boundary pinning was prominent in the pure sample but weakened in the Na-substituted samples. These results are in harmony with other studies on BSCCO [80,103]. Furthermore, they indicate that the core interaction was the dominant pinning mechanism in all samples, as predicted by Dew-Hughes [20].

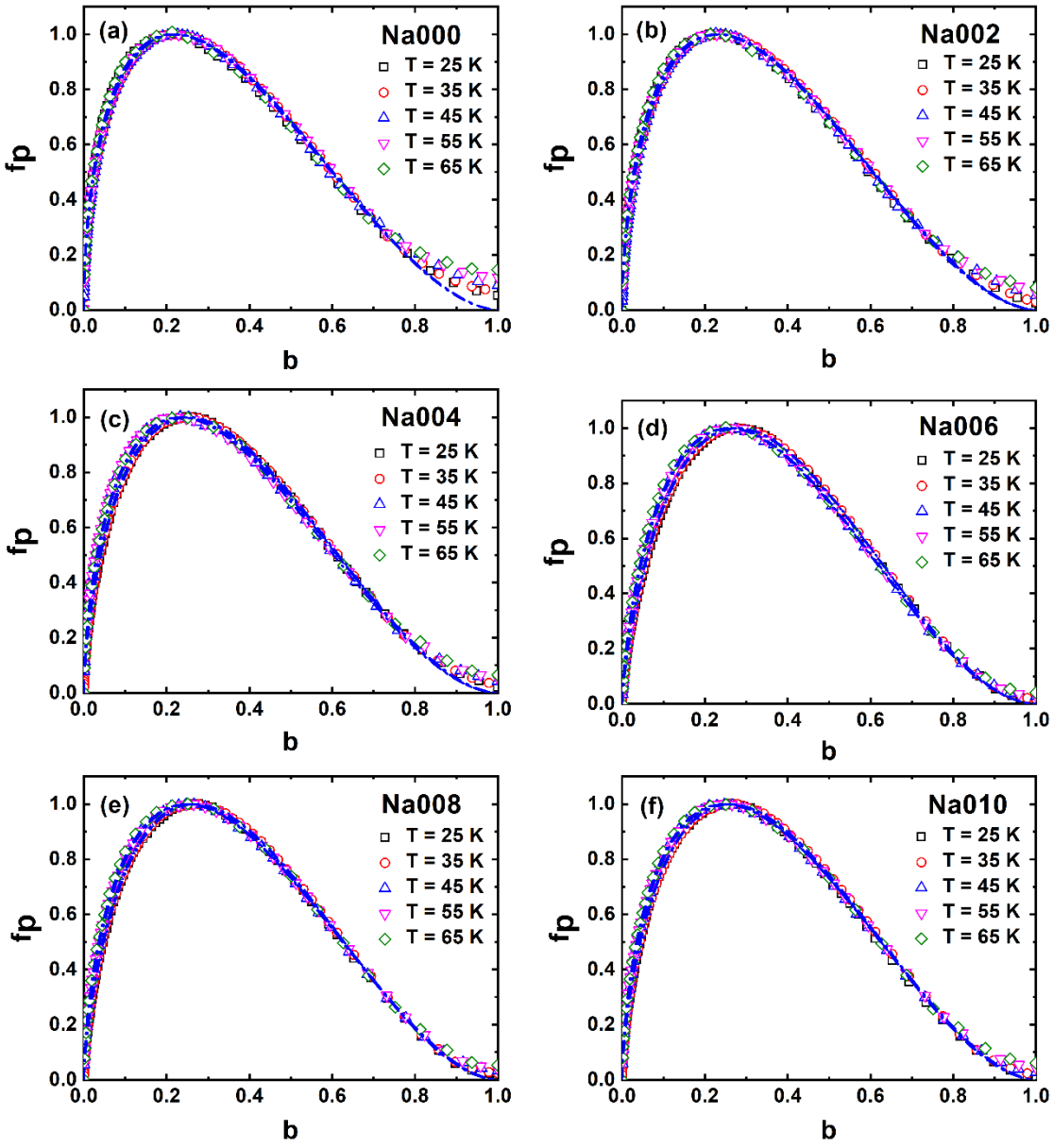

Figure 3.8. Scaling behaviors of the normalized pinning force density (f_p) versus (b) at all measured temperatures of (a) Na000, (b) Na002, (c) Na004, (d) Na006, (e) Na008 and (f) Na010 samples. The solid lines are the fitting curves using Eq. (1.7).

One plausible explanation for these phenomena could be related to the successful partial substitution of Na^+ into Ca sites. Consequently, the mismatch

in ionic radii between Ca^{2+} and Na^{+} created additional point-like defects [43]. As a result, the flux pinning behavior in the BPSCCO samples was improved through Na substitutions, confirming its role in enhancing J_c.

Table 3.2. Flux pinning centers properties with modified Dew-Hughes model scaling of the samples at 65 K, 55 K, 45 K, and 35 K.

Sample	T = 65 K			T = 55 K		
	p	q	b_{peak}	p	q	b_{peak}
Na000	0.514	1.934	0.210	0.534	2.009	0.213
Na002	0.544	1.827	0.229	0.531	1.812	0.226
Na004	0.592	1.866	0.240	0.588	1.853	0.240
Na006	0.703	1.924	0.267	0.716	1.941	0.269
Na008	0.637	1.822	0.259	0.624	1.817	0.255
Na010	0.612	1.803	0.253	0.607	1.791	0.253
Sample	T = 45 K			T = 35 K		
	p	q	b_{peak}	p	q	b_{peak}
Na000	0.517	1.910	0.221	0.524	1.847	0.211
Na002	0.531	1.826	0.225	0.532	1.827	0.225
Na004	0.591	1.864	0.241	0.589	1.866	0.240
Na006	0.710	1.926	0.269	0.715	1.924	0.271
Na008	0.635	1.822	0.259	0.624	1.822	0.255
Na010	0.612	1.791	0.255	0.612	1.803	0.253

3.3.3. Flux pinning mechanism

The outcomes derived from the Dew-Hughes model have validated that the primary interactions between vortices and pinning centers within the samples were core interactions [111]. In the context of type-II superconductors, core predominant pinning encompasses δl pinning, which pertains to fluctuations in the charge carrier mean free path near lattice defects, and δT_c

pinning, associated with spatial variations in the Ginzburg-Landau coefficient [50,61,79]. The individual expressions for these components were originally formulated by Griessen et al., as referenced in 1.2.1 [27]. The results of the fitting process are depicted in Figure 3.9(a). Upon comparing the theoretical predictions with the experimental data, it becomes evident that δl pinning was the dominant pinning mechanism across all samples within the temperature range of 65 K to 25 K. This suggests that the primary type of defect likely resulted from the formation of point-like defects due to the partial substitution of Na^{+} for Ca^{2+}, leading to spatial variations in the mean free path.

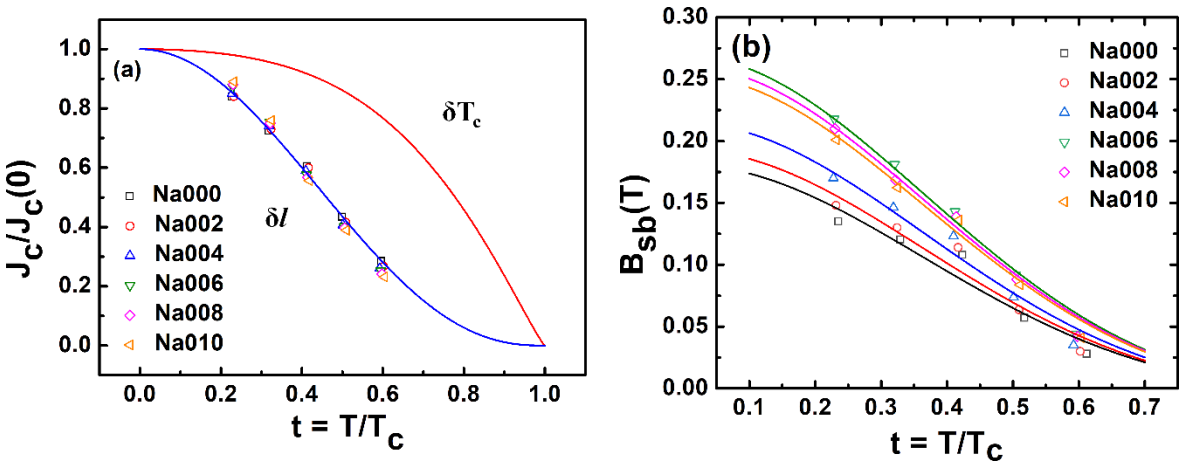

Figure 3.9. (a) Normalized critical current density $J_c(t)/J_c(0)$ versus normalized temperature t of all the samples; (b) Crossover field (B_{sb}) versus normalized temperature of all the samples. The solid lines are the fitting curves using Eq. (1.5).

Following the investigation of the pinning mechanism described above, B_{sb} was subjected to fitting as a function of temperature using the δl pinning model [25,61,79,106]. The normalized temperature dependence of B_{sb} and the corresponding fitting curves can be found in Figure 3.9(b). This outcome reaffirmed the dominance of δl pinning, resulting from spatial variations in the charge carrier mean free path, as illustrated in Figure 3.9(a). In summary, the

consistency between the collective pinning model and the Dew-Hughes model indicates that the introduction of 0D punctual defects via partial Na substitution enhances J_c through the δl core interaction over a wide range of temperatures and magnetic fields, utilizing a flux pinning mechanism.

3.4. CONCLUSION OF CHAPTER 3

In this chapter, the scaling behaviour of flux pinning forces in $Bi_{1.6}Pb_{0.4}Sr_2Ca_{2-x}Na_xCu_3O_{10+\delta}$ superconductors was systematically investigated. It was found that the magnetic field dependence of J_c at different temperatures ranged between 65 K and 25 K was significantly enhanced by the Na substitution via point-like defect creations. This field dependence of J_c was well described using the collective pinning theory. The B-T phase diagrams were constructed to include a significant expansion of the small bundle pinning regime. The flux pinning mechanism was investigated by analysing the normalized field (b) dependences of pinning force density (F_p). For all samples investigated, the dominant pinning mechanism appeared to be temperature independent. The improved flux pinning properties in the Na-substituted samples were evident from comparing the fitting values of p, q and b_{peak} following the Dew-Hughes model. The obtained data also demonstrated the growth of point-like pinning and the decline of grain boundary pinning resulting from the Na substitution. Especially, the δl pinning was found to be the predominant pinning mechanism responsible for the samples, which was related to spatial variations in the mean free path of charge carriers.

CHAPTER 4: IMPROVEMENTS OF CRITICAL CURRENT DENSITY IN HIGH-T_c $Bi_{1.6}Pb_{0.4}Sr_2Ca_2Cu_3O_{10+\delta}$ SUPERCONDUCTOR BY ADDITION OF NON-MAGNETIC TiO_2 NANOPARTICLE

After obtaining the improvements of J_c in BPSCCO samples by the addition of induced point-like defects via Na substitutions, additions of pinning centers whose larger average size in form of nanoparticles in BPSCCO samples are performed. Purpose of continue study is examining effect of increase size of APCs, the first stage of research series is carried out with a selection of non-magnetic nanoparticles. Among non-magnetic nano-materials, TiO_2 nanoparticle is one of the most produced ceramic nanoparticles with high stability, simple preparation, and less harmful to human health. Therefore, TiO_2 nanoparticles can satisfy the ability in industrial manufacture. Besides, TiO_2 nanoparticles were proved to enhance the critical current density and improve flux pinning properties of high-T_c superconductors in other reports [30-32]. Hence, the addition of TiO_2 nanoparticles was expected to improve the J_c and flux pinning properties of BPSCCO superconductor. Detailed analyses in changes in flux pinning mechanism in the TiO_2 added BPSCCO samples, which was not fully studied in the past, will be systematically investigated.

4.1. NANOPARTICLE CHARACTERISTICS

Figure 4.1 displays TEM images of the produced TiO_2 nanoparticles along with their corresponding histogram prior to their incorporation into BPSCCO superconductors. These nanoparticles exhibited a nearly spherical morphology, with crystallite dimensions spanning from 4 to 22 nm. On average, the size of these TiO_2 nanoparticles measured approximately 12 nm, falling within the range bounded by the coherence length ($\xi \sim 2.9$ nm) and the penetration depth ($\lambda \sim$ 60-1000 nm) of BSCCO [30,108].

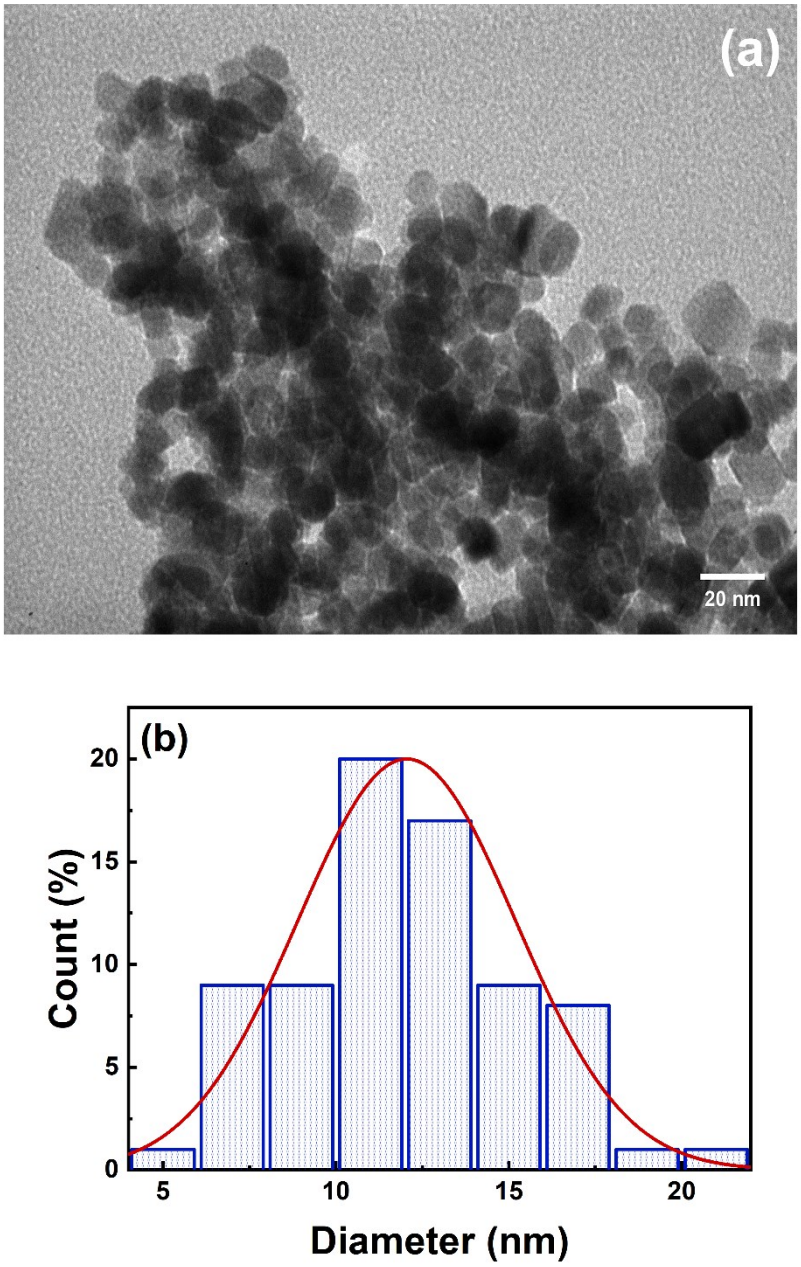

Figure 4.1. (a) TEM images and (b) histogram of TiO_2 nanoparticles.

4.2. FORMATION OF THE SUPERCONDUCTING PHASES

4.2.1. Phase analysis

Figure 4.2 presents XRD patterns for all the samples. The indexed XRD data reveal that these samples comprised both Bi-2223 and Bi-2212 phases. Peaks corresponding to the Bi-2223 phase were denoted by "H", while those corresponding to the Bi-2212 phase were denoted by "L".

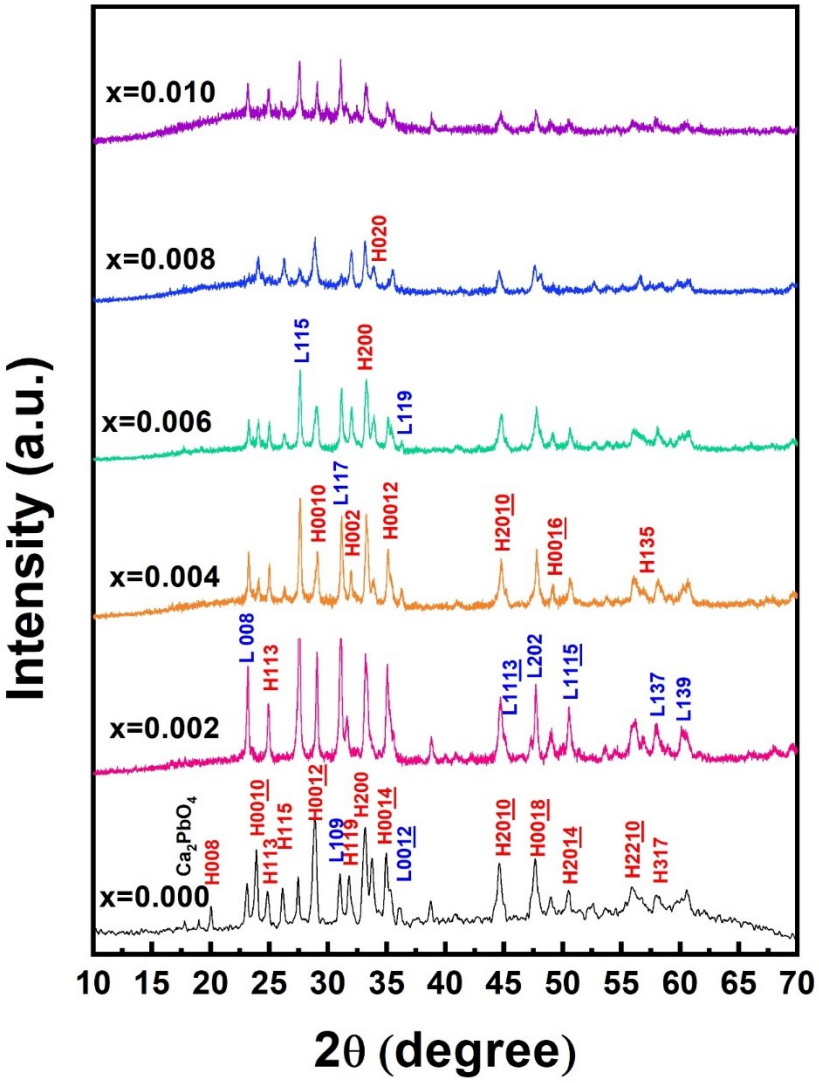

Figure 4.2. XRD patterns of $(Bi_{1.6}Pb_{0.4}Sr_2Ca_2Cu_3O_{10+\delta})_{1-x}(TiO_2)_x$ samples, with x = 0, 0.002, 0.004, 0.006, 0.008, and 0.010.

In the pure sample, the dominant phase is Bi-2223. However, in the samples with additives, notably in samples with higher additive content, the Bi-2212 phase became more prominent. The XRD patterns of these additive-containing samples displayed a significant increase in the intensity of peaks related to the Bi-2212 phase, whereas several peaks associated with Bi-2223

disappeared. In samples with high additive concentrations, such as x = 0.008 and x = 0.010, the background signal in the XRD pattern gradually increased. This could be attributed to the presence of nanoparticles as impurities.

To explore how the presence of TiO_2 impacts phase formation, the volume fraction of each phase was determined using the following relations:

$$\%Bi-2223 = \frac{\Sigma I_{2223}}{\Sigma I_{2223}+\Sigma I_{2212}} \times 100\%, \quad (4.1)$$

$$\%Bi-2212 = \frac{\Sigma I_{2212}}{\Sigma I_{2223}+\Sigma I_{2212}} \times 100\%, \quad (4.2)$$

where I_{2223} and I_{2212} are the intensity summations of the Bi-2223 and Bi-2212 phase peaks, respectively [13,90,108]. The calculated results have been summarized in Table 4.1. The volume fraction values indicate that the percentage of Bi-2223 phase decreased steadily as the TiO_2 content increased. In the pure sample, Bi-2223 accounted for 67.09% of the composition. For samples with x = 0.002 and x = 0.004, the percentage of Bi-2223 gradually decreased to 54.17% and 50.13%, respectively. However, at higher TiO_2 concentrations, the decline in *%Bi-2223* became more pronounced. In particular, the x = 0.010 sample exhibited only 27.84% Bi-2223. The values presented in Table 4.1 demonstrate that the crystallite size decreased with increasing TiO_2 nanoparticle content. Both the volume fraction and crystallite size analysis results suggest that TiO_2 nanoparticles slowed down the formation of the Bi-2223 phase.

The lattice parameters of the Bi-2223 phase were computed for all samples, and no significant variations were observed. The lattice parameters remained consistent at approximately $a = b$ = 5.395 ± 0.007 Å and c = 37.07 ± 0.01 Å, indicative of a tetragonal structure. This observation suggests that the TiO_2 nanoparticles did not incorporate into the superconducting structure.

Table 4.1. The volume fraction, average crystallite size, lattice constants for Bi-2223 phase, T_c and ρ_0 values of $(Bi_{1.6}Pb_{0.4}Sr_2Ca_2Cu_3O_{10+\delta})_{1-x}(TiO_2)_x$ samples, with x = 0, 0.002, 0.004, 0.006, 0.008, and 0.010.

x	*%Bi-2223*	*%Bi-2212*	τ (nm)	a (Å)	b (Å)	c (Å)	T_c (K)	ρ_0 (mΩ.cm)
0.000	67.09	32.91	43.25 ± 0.008	5.402 ± 0.007	5.388 ± 0.007	37.07 ± 0.01	107.10	9.34 ± 0.01
0.002	64.17	35.83	35.35 ± 0.008	5.409 ± 0.007	5.382 ± 0.007	37.07 ± 0.01	100.50	10.72 ± 0.01
0.004	50.13	59.87	34.73 ± 0.007	5.403 ± 0.007	5.386 ± 0.007	37.07 ± 0.01	96.91	11.64 ± 0.01
0.006	41.43	58.57	32.68 ± 0.006	5.404 ± 0.007	5.390 ± 0.007	37.07 ± 0.01	92.25	12.40 ± 0.01
0.008	35.16	64.84	31.50 ± 0.007	5.406 ± 0.007	5.380 ± 0.007	37.07 ± 0.01	86.42	22.04 ± 0.01
0.010	27.84	72.16	29.24 ± 0.008	5.404 ± 0.007	5.383 ± 0.007	37.07 ± 0.01	85.44	42.56 ± 0.01

4.2.2. Surface morphology

The surface morphology of the samples was analyzed through SEM images at 5000X magnification, as shown in Figure 4.3.

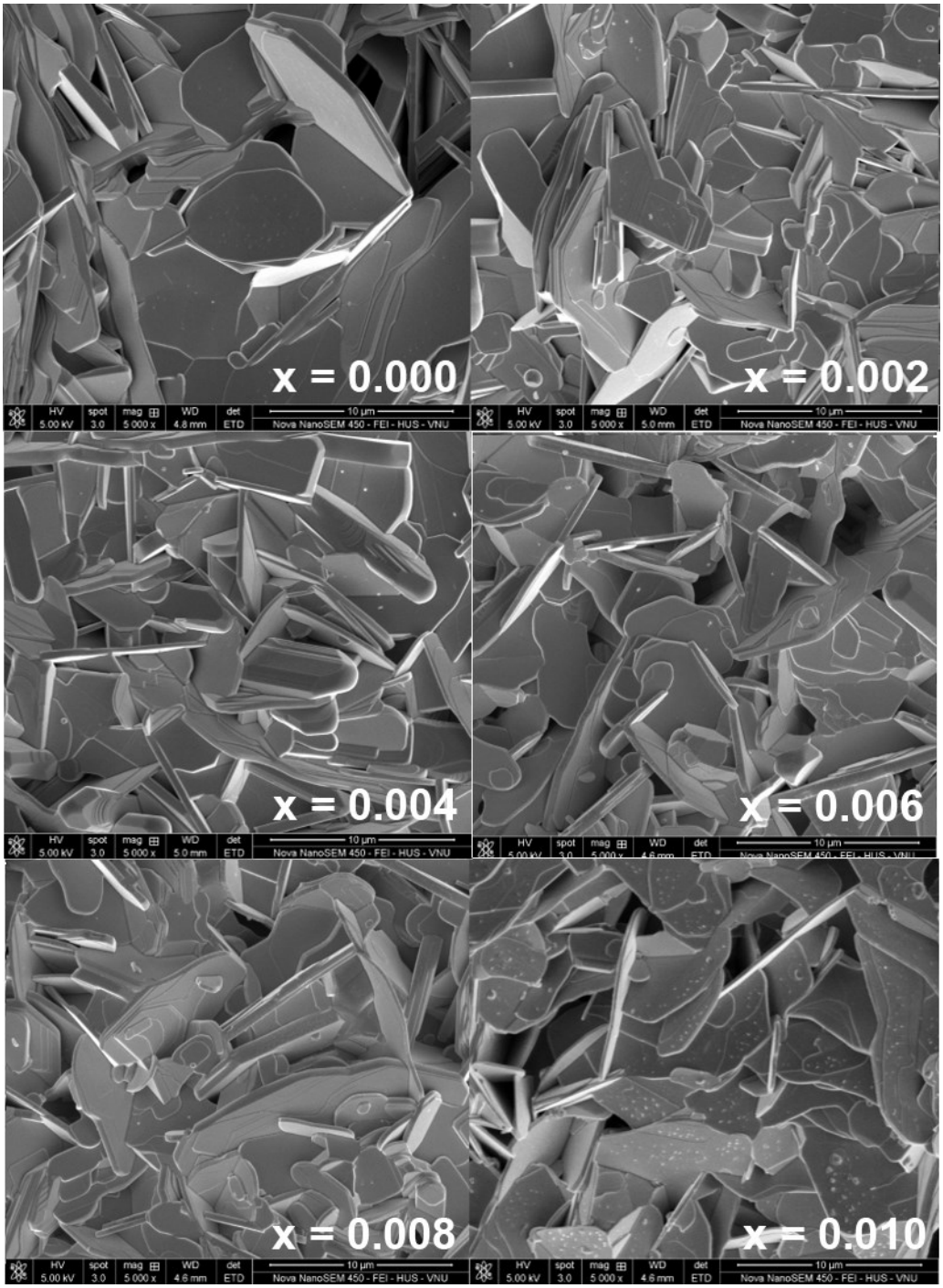

Figure 4.3. SEM images of $(Bi_{1.6}Pb_{0.4}Sr_2Ca_2Cu_3O_{10+\delta})_{1-x}(TiO_2)_x$ samples, with x = 0, 0.002, 0.004, 0.006, 0.008, and 0.010.

The grains exhibited a plate-like structure, which is commonly observed in ceramic BSCCO superconductors [4,72]. Notably, the inclusion of TiO_2 led

to noticeable alterations in the surface morphology of the samples. The surface of the sample without TiO_2 addition appeared relatively dense and smooth, featuring large and uniformly oriented grains. In contrast, the TiO_2-added samples displayed more misoriented grains. As the TiO_2 content increased, the average crystallite size gradually decreased. A smooth and dense surface was maintained in samples with TiO_2 content up to x = 0.004. However, a significant increase in porosity was observed when x ranged from 0.006 to 0.010. Consequently, inter-grain connectivity was reduced in these samples. These findings align with the XRD results, indicating that the addition of TiO_2 had a negative impact on the crystallinity of the superconducting phase, especially at higher TiO_2 content.

4.3. THE CORRELATION BETWEEN LOCAL STRUCTURE VARIATIONS AND CRITICAL TEMPERATURE

4.3.1. Critical temperature

The temperature-dependent resistivity of all samples was examined within the range of 50–300 K, and the results are presented in Figure 4.4(a). It was observed that the addition of TiO_2 resulted in a reduction of the samples' superconducting transition temperature, T_c. The T_c values for each sample were determined as the temperature at which the resistivity reached zero and are listed in Table 4.1. For the pure sample, T_c was estimated to be 107.09 K. However, with the introduction of TiO_2, the T_c value decreased to 100.50 K for x = 0.002 and continued to decrease as x increased. The lowest T_c value was observed in the x = 0.010 sample, at 85.44 K, which is in the range of critical temperatures seen in the Bi-2212 phase (~ 80 K). This reduction in T_c can be attributed to several factors, including the slower formation of the high-Tc Bi-2223 phase, the presence of non-superconducting TiO_2 nanoparticles,

weakened connectivity between grains, and grain misorientation, as determined through XRD and SEM analyses [109,110].

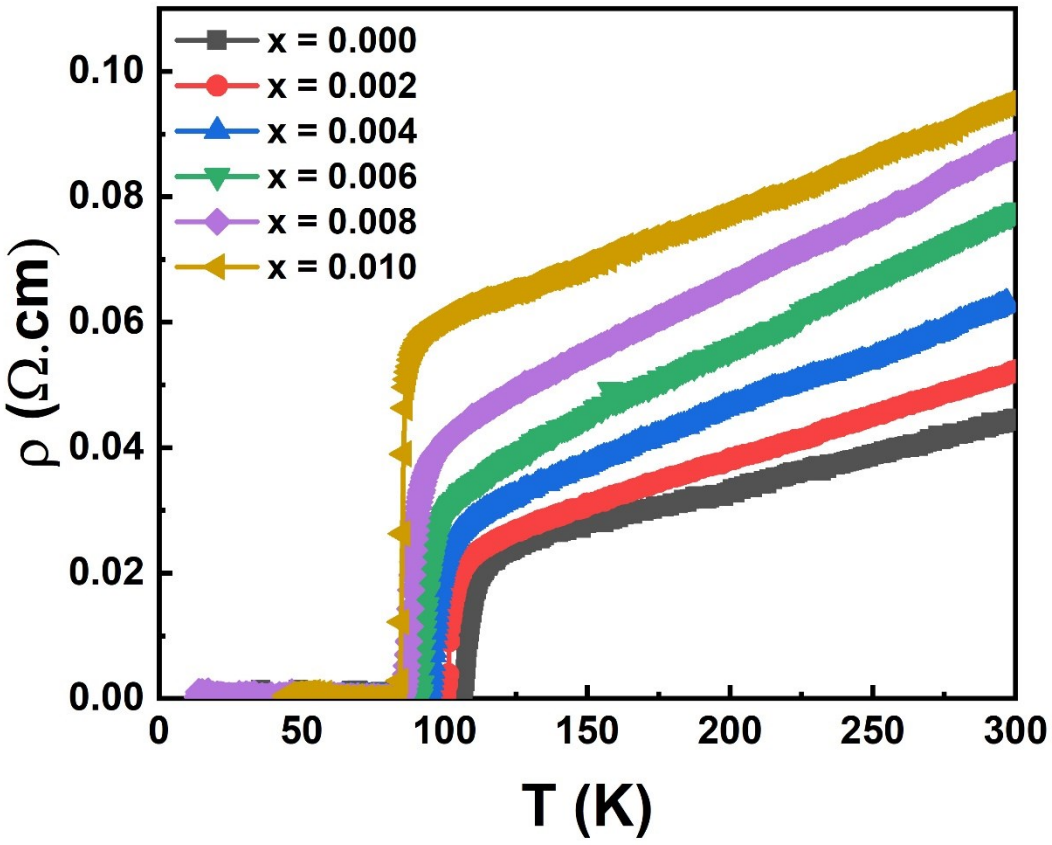

Figure 4.4. The temperature dependence of resistivity of $(Bi_{1.6}Pb_{0.4}Sr_2Ca_2Cu_3O_{10+\delta})_{1-x}(TiO_2)_x$ samples, with x = 0, 0.002, 0.004, 0.006, 0.008, and 0.010.

In the normal state, both the non-added and added samples exhibited metallic behavior. However, the resistivity values showed an increasing trend in the presence of TiO_2. To further investigate the effects of TiO_2 doping, Anderson and Zou's linear relation was applied for analyzing the high-temperature regime using the following function [5,109,110], as follows:

$$\rho(T) = aT + \rho_0, \quad (4.3)$$

where ρ is resistivity, T is temperature, a is linear slope, and ρ_0 is residual resistivity, which was extrapolated using the function mentioned above to the temperature of 0 K. The values of ρ_0 were extrapolated and are provided in Table 4.1. It was observed that ρ_0 increased gradually for x = 0.002 and 0.004. However, starting from x = 0.006, the rate of increase in ρ_0 became more pronounced. When x = 0.010, the ρ_0 value was approximately three times higher than that in the pure sample. These findings align with the results obtained from XRD and SEM investigations, indicating a consistent trend of increased residual resistivity with higher TiO_2 content.

It can be noted that the introduction of suitable types of pinning centers has indeed been demonstrated to enhance J_c in BPSCCO polycrystalline superconductors. Nevertheless, there is a clear trend of gradual decreases in T_c. Building on previous research, a strong link between changes in the local structure and variations in T_c of the fabricated samples has been established [97]. In the following section, we will apply structural analysis models to investigate the mechanism behind the observed degradation in T_c.

4.3.2. Fluctuation of mean field region

The analysis of the mean field region was conducted using the Aslamazov-Larkin (A-L) theory, which explains excess conductivity ($\Delta\sigma$) and provides insights into the behavior of microscopic structures and superconducting parameters [7,35,54,70,87]. Excess conductivity is defined as the difference between superconducting and metallic resistivity and can be calculated using the following formula [7,35,55,70,87]:

$$\Delta\sigma = \sigma(T) - \sigma_n(T), \tag{4.4}$$

where $\sigma(T) = 1/\rho(T)$ is the experimental conductivity, $\sigma_n(T) = 1/\rho_n(T)$ is the extrapolated conductivity from the metallic behavior region, and $\rho_n(T)$ is the resistivity extrapolated by the Anderson–Zou relation.

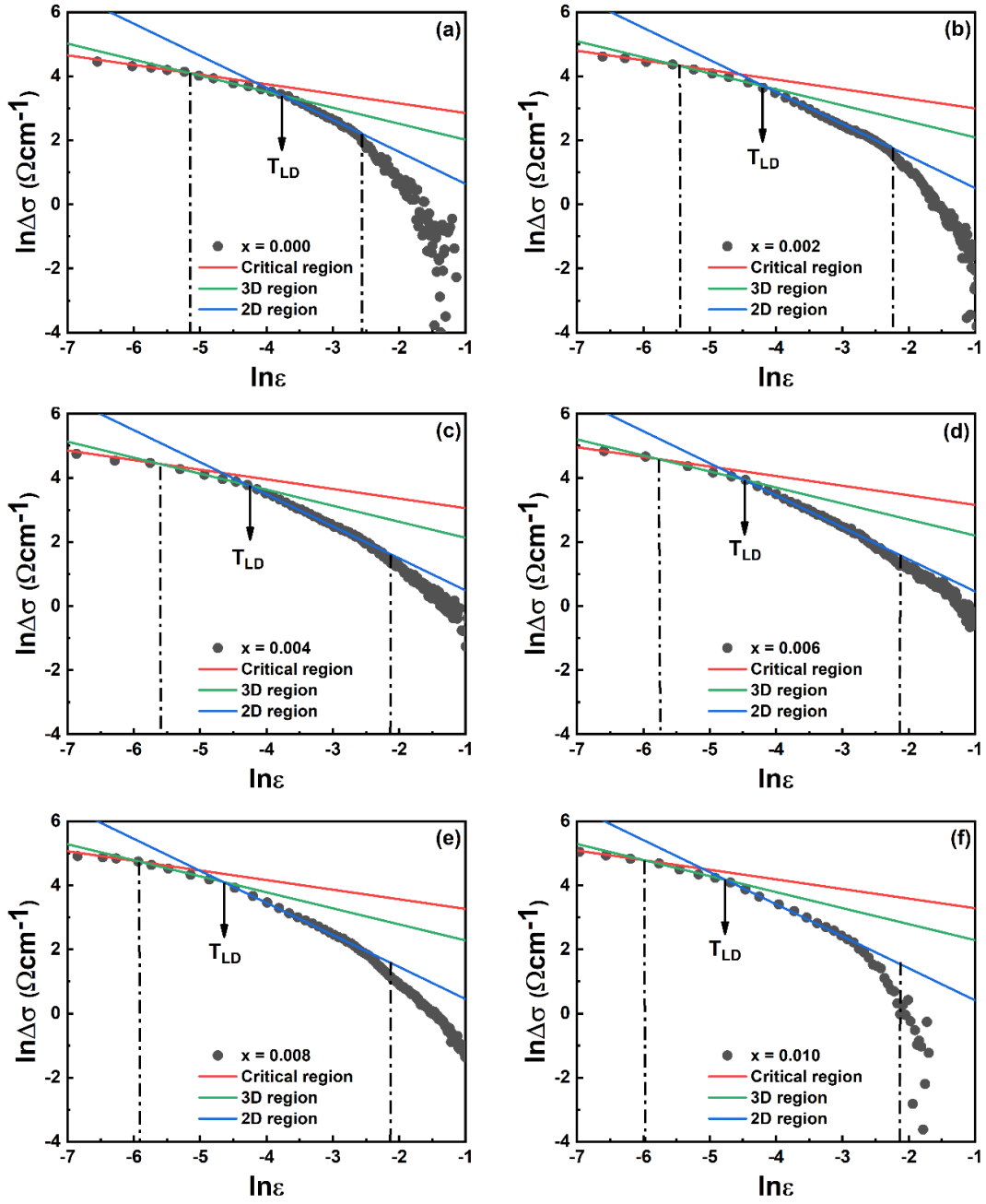

Figure 4.5. Double logarithmic plot of excess conductivity as a function of reduced temperature of $(Bi_{1.6}Pb_{0.4}Sr_2Ca_2Cu_3O_{10+\delta})_{1-x}(TiO_2)_x$ samples (a) $x = 0$, (b) $x = 0.002$, (c) $x = 0.004$, (d) $x = 0.006$, (e) $x = 0.008$, and (f) $x = 0.010$. The red, green, and blue solid lines correspond to the critical region, 3D and 2D region, respectively.

Excess conductivity is often theoretically modeled as $\Delta\sigma = A\varepsilon^{-k}$, where $\varepsilon = (T - T_c)/T_c$ is the reduced temperature, and k is the Gaussian critical exponent featuring Cooper pair fluctuation regions [7,31,54,66,92]. Theoretical classifications by Aslamazov and Larkin identify four specific regions, including $k = 0.3$ for critical fluctuations (CR), $k = 0.5$ for 3D fluctuations, $k = 1.0$ for 2D fluctuations, and $\lambda = 3.0$ for short wave fluctuations (SWF). Logarithmic plots of $\Delta\sigma$ versus ε for samples ranging from $x = 0.00$ to $x = 0.01$ were created on Figure 4.5(a–f) to investigate the CuO_2 interlayer coupling variations in the samples, respectively. The mean field regions were delineated by their characteristic fitting slopes, represented as solid red, green, and blue lines for the critical, 3D, and 2D regions, respectively. The interlayer coupling properties can be estimated by analyzing the fitting parameters within the 3D and 2D regions, following the approach suggested by Oh *et al.* [70]. Within the mean-field region, pairs of conducting electrons formed and primarily moved within the CuO_2 plane, characteristic of the 2D region [7,33,49]. As the temperature decreased, Josephson channeling developed between the CuO_2 planes, leading to the transition into the 3D region. Consequently, conducting electron pairs could move more freely between the conducting layers. The experimental results aligned well with theoretical predictions in all samples. However, slight variations in the range of the 2D and 3D regions were observed with the presence of TiO_2. In the pure sample, the mean field region spanned approximately $-5 < \ln\varepsilon < -2.5$. With the introduction of TiO_2, the mean field region extended from $\ln\varepsilon$ values of -5.5 or -6 to $\ln\varepsilon$ of -2.5. This indicated variations in both the intra-layer, corresponding to the 2D region, and the interlayer, corresponding to the 3D region, conducting behavior and local structure. In the Lawrence–Doniach (L–D) model, the L-D temperature T_{LD} was defined as the crossover point between the 2D and 3D regions, used to establish

the relationship between mean field regions and estimate the interlayer coupling strength $J = 1 - T_{LD}/T_c$. The calculated values are summarized in Table 4.2. The T_{LD} value for the pure sample was 106.34 K, which decreased progressively from 100.26 K to 85.31 K as the TiO_2 nanoparticle content increased. Consequently, the interlayer coupling strength declined from 0.0234 to 0.0086 due to the presence of TiO_2 nanoparticles.

The interlayer coupling strength, denoted as J, is dependent on two key parameters: the c-axis coherence length ξ_c and the effective interlayer spacing of CuO_2 planes, following the relationship $J = [2\xi_c(0)/d]^2$ [7]. To investigate deeper the conducting and local structure fluctuations, we measured the temperature-independent constant A in $\Delta\sigma$ expression of Aslamazov–Larkin using the following equations:

$$A = \frac{e^2}{32\hbar\xi_c(0)}, \tag{4.5}$$

for 3D fluctuations, and

$$A = \frac{e^2}{16\hbar d}, \tag{4.6}$$

for 2D fluctuations, where e is the electron charge, $\hbar$ is the Planck constant [7]. However, for a strongly anisotropic superconductor like the Lawrence–Doniach (L–D) model, d can be estimated from the interpolated β value using the formula $\beta = 16\hbar d/e^2 T_{ext}$, where T_{ext} is the temperature at the intersection of the extrapolation line with the temperature axis [35,70,87]. The coherence length at 0 K $\xi_c(0)$ and effective inter-layering spacing d were calculated and presented in Table 4.2.

The coherence length and effective inter-layer spacing increased as the TiO_2 content increased. This observation can explain the reduction in the superconducting properties of the material within the CuO_2 interlayer.

However, the significant decrease in T_c with increasing TiO_2 content may be attributed to other factors.

Table 4.2. Excess conductivity analysis calculated parameters of $(Bi_{1.6}Pb_{0.4}Sr_2Ca_2Cu_3O_{10+\delta})_{1-x}(TiO_2)_x$ samples, with x = 0, 0.002, 0.004, 0.006, 0.008, and 0.010.

x	T_{LD} (K)	J	$\xi_c(0)$ (Å)	d (Å)
0	106.34	0.0234	1.27	59.43
0.002	100.25	0.0155	1.38	82.15
0.004	97.11	0.0138	1.39	95.19
0.006	92.58	0.0112	1.49	111.74
0.008	87.94	0.0094	1.65	116.13
0.010	85.31	0.0086	1.77	118.52

4.3.3. Local structure variations

The bond distance is a crucial piece of information that can confirm the substitution of a site in the crystal structure [89]. Therefore, Cu-related bond distances, including Cu-O, Cu-Ca, and Cu-Sr, were calculated from XRD patterns using the Rietveld refinement method [85]. The calculated values are provided in Figure 4.6. It was evident that the bond distance of Cu-O only slightly changed with increasing TiO_2 content. However, the Cu-Ca and Cu-Sr bond distances increased significantly with increasing TiO_2 content. These observed variations indicate that a foreign ion may have substituted for Cu in the conducting plane or its reservoir planes [40,89]. Thus, the atomic characteristic fluctuation of copper was further investigated through X-ray absorption spectral analysis.

Based on the evidence from A–L and L–D theory analyses, as well as the increase in bond distances, the primary cause of the decrease in T_c is the variation in the local superconducting structure. However, the exact cause of

this structural fluctuation remains unclear. Other research has reported the substitution of trivalent ions into divalent ion positions [22,107,109,110].

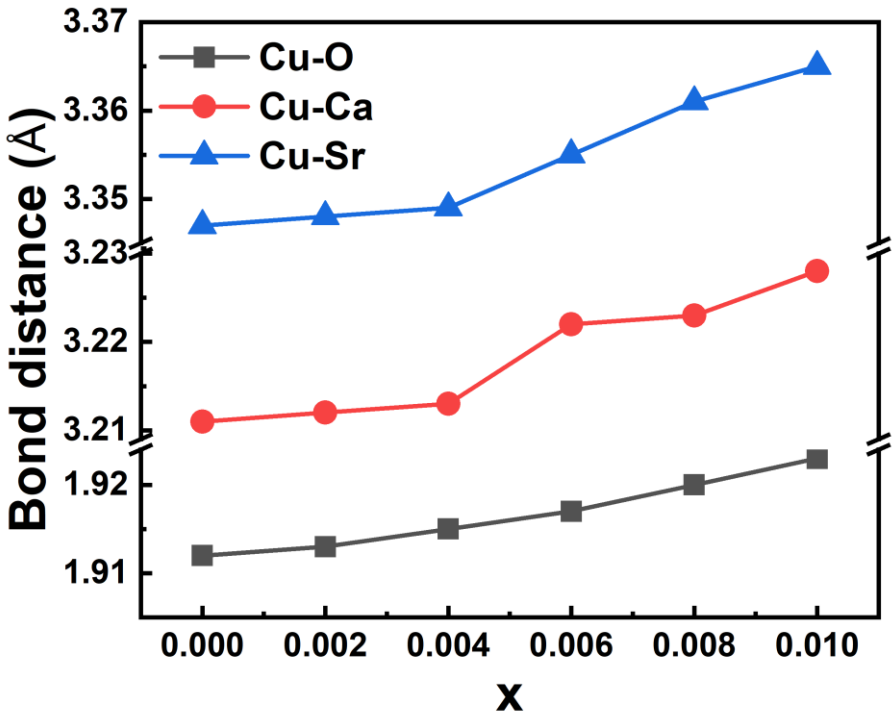

Figure 4.6. The Cu-O, Cu-Ca and Cu-Sr bond distances of $(Bi_{1.6}Pb_{0.4}Sr_2Ca_2Cu_3O_{10+\delta})_{1-x}(TiO_2)_x$ samples, with x = 0, 0.002, 0.004, 0.006, 0.008, and 0.010.

Yildirim *et al*. reported that the substitution of trivalent ions for Cu, Ca, and Pb sites in BPSCCO leads to the degradation of the Bi-2223 superconducting phase [109,110]. Similarly, the substitution of divalent cations by tetravalent ions (Ti^{4+}) may also lead to a decrease in T_c due to degradation in local structure and ionic properties. Many studies have examined the effect of creating holes in conducting layers by substituting ions of different valences into the crystal structure [64,88]. The electronic structure of the CuO_2 planes was investigated via XANES. The Cu K-edge XANES spectra of the samples

with added TiO_2 and reference data for Cu^{1+} and Cu^{2+} are shown in Figure 4.7(a). To indicate the peaks in the spectra, two vertical dashed lines were drawn to represent Cu^{1+}- and Cu^{2+}-related peaks. The higher energy stage corresponds to Cu^{2+}. These peaks arise due to electron transitions from the ground to an excited state. In general, the orbital of Cu^{1+} ion is completely filled with a $3d^{10}$ configuration, while the orbital of Cu^{2+} ions with a $3d^9$ configuration has a hole [11,98]. This result can be attributed to the quadrupole transition from 1s to 3d, which is the pre-peak P, as shown in Figure 4.7(a). With an increase in photon energy, the electron can make a longer transition from the 1s to the 4p orbital. These transitions are denoted as peaks A and B. The crystalline field splits the 4p orbital into two sub-states: out-of-plane ($4p_\pi$) and in-plane ($4p_\sigma$) states. Peak A results from the transition from 1s to $4p_\pi$ ($3d^{10}\ L^{-1}$) (where L denotes an oxygen ligand hole), whereas peak B is created by the transition from 1s to $4p_\pi$ ($3d^9$). The 1s-to-$4p_\pi$ ($3d^{10}\ L^{-1}$) transition corresponds to the electron transfer between the ligand and metal, which enhances the electron shielding effect and lowers the transition energy [53,63,81,82]. As shown in the Cu K-edge XANES spectra, the main peaks of the samples with added TiO_2 were at higher energies compared to both peaks of Cu^{1+} (Cu_2O) and Cu^{2+} (CuO). This suggests that the Cu valence in CuO_2 is between Cu^{2+} and Cu^{3+}, and it can be calculated using the following equation [97]:

$$V_{\mathrm{Cu}} = \frac{E_{\mathrm{sample}} - E_{\mathrm{Cu^{2+}}}}{E_{\mathrm{Cu^{2+}}} - E_{\mathrm{Cu^{+}}}} + 2, \tag{4.7}$$

where E_{sample}, $E_{\mathrm{Cu^{2+}}}$, and $E_{\mathrm{Cu^{1+}}}$ were gained from the maxima of the first derivative curves of Cu-K edge XANES. The subtraction of the denominator was 2.6 eV. Figure 4.7(b) depicts the valence state variation depending on the TiO_2 content. Interestingly, the valence state and critical temperature both exhibited the same trend with the TiO_2 content. This suggests that the change

in hole concentration is likely the primary factor contributing to the degradation of the critical temperature in the samples.

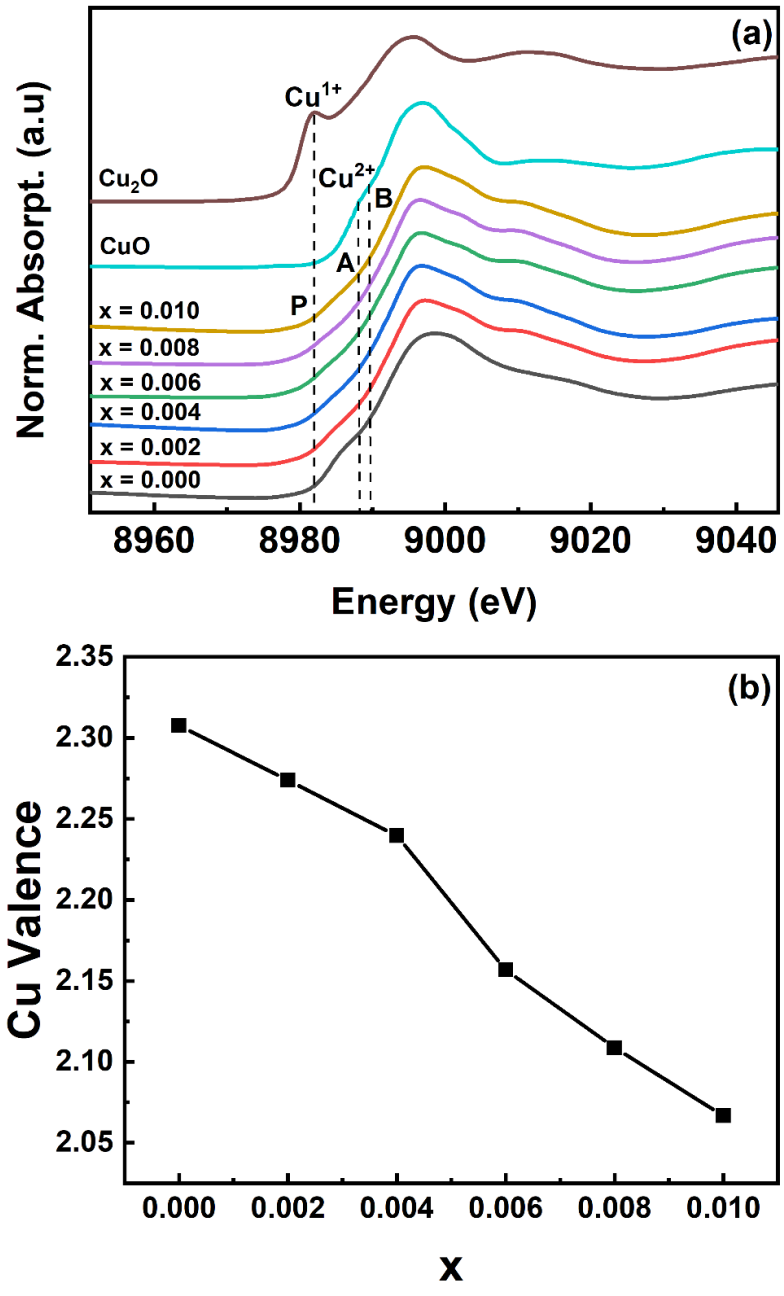

Figure 4.7. (a) Cu K-edge XANES spectra of $(Bi_{1.6}Pb_{0.4}Sr_2Ca_2Cu_3O_{10+\delta})_{1-x}(TiO_2)_x$ samples, with x = 0, 0.002, 0.004, 0.006, 0.008, and 0.010. (b) Copper valence of all samples.

The Cu $L_{2,3}$-edge spectra for all samples are plotted in Figure 4.8(a). The carrier concentration in the conducting planes was calculated from the XANES spectra of the Cu $L_{2,3}$-edge. This measurement was conducted at room temperature, and the energy range was set from 920 eV to 980 eV. Two main peaks appeared at approximately 933 and 955 eV for all samples. These peaks represent electron transitions from the ground state configuration $Cu(2p^{3/2,\ 1/2})$ $3d^9$ – $O2p^6$ to the excited state configuration $Cu(2p^{3/2,\ 1/2})^{-1}$ $3d^{10}$ – $O2p^6$. The $Cu(2p^{3/2,\ 1/2})^{-1}$ denotes that a hole was left by an excited electron in the Cu $2p^{3/2}$ or Cu $2p^{1/2}$ configuration. This main peak indicates the transition of Cu^{2+} [25,41–43]. Interestingly, these peaks were asymmetric. After deconvolution with the pseudo-Voigt function, a small shoulder appeared on the right side of the main peaks (as shown in Figure 4.8(b)), which corresponds to the transition of Cu^{3+} from $Cu(2p^{3/2,\ 1/2})$ $3d^9$ – L configuration to Cu $(2p^{3/2,\ 1/2})^{-1}$ $3d^{10}$ – L configuration, where L denotes the ligand hole [42,43]. Then, the hole concentration (p) was calculated based on an equation presented by Karppinen et al [42,43]. In this calculation, p represents the ratio of the Cu^{3+} peak intensity to the total intensity of the Cu^{2+} peaks and Cu^{3+} peaks. The L_3 spectra had higher intensity than the L_2 spectra, suggesting that they are more suitable for fitting with the pseudo-Voigt function. The intensities of the main and shoulder peaks were determined from the fitting of the L_3 spectra and applied to the following equation:

$$p = \frac{I(\mathrm{Cu^{3+}})}{(I(\mathrm{Cu^{2+}})+I(\mathrm{Cu^{3+}}))}, \tag{4.8}$$

where $I(Cu^{2+})$ and $I(Cu^{3+})$ are the integrated intensities of the main and shoulder peaks, respectively. The calculation results are presented in Figure 4.8(c).

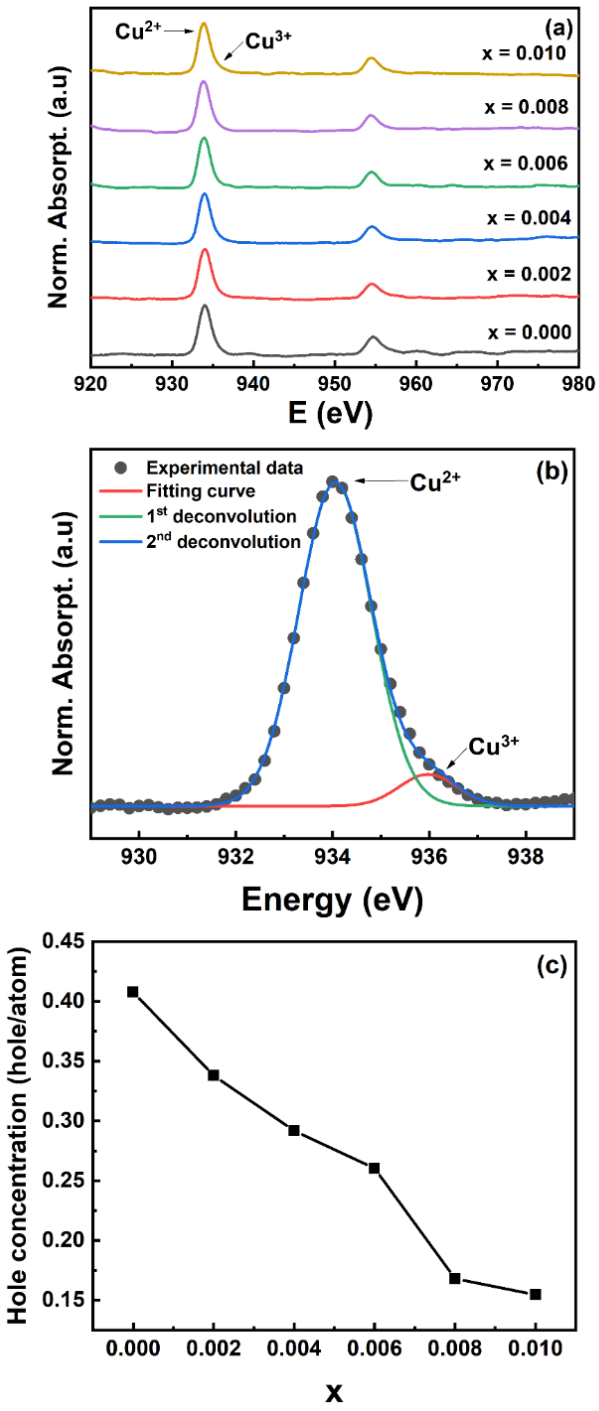

Figure 4.8. (a) Cu $L_{2,3}$-edge XANES spectra of $(Bi_{1.6}Pb_{0.4}Sr_2Ca_2Cu_3O_{10+\delta})_{1-x}(TiO_2)_x$ samples, with x = 0, 0.002, 0.004, 0.006, 0.008, and 0.010. (b) Cu L_2-edge XANES spectra deconvolution with pseudo-Voigt function. (c) Hole concentration of all samples.

With the increase in TiO_2 content, the hole carrier concentration values decreased from approximately 0.42 to nearly 0.15. This phenomenon can be explained by the hole filling effect becoming stronger, leading to a lower carrier concentration in the conducting planes. These pieces of evidence indicate that the Cu site in the superconducting structure was partially substituted by a higher valence ion, which is predicted to be Ti^{4+} ions, and this substitution led to a significant decline in T_c. Nevertheless, the substitution incident also influenced to some extent the enhancement of J_c via the point-like defects in the structure acting as the flux pinning centers.

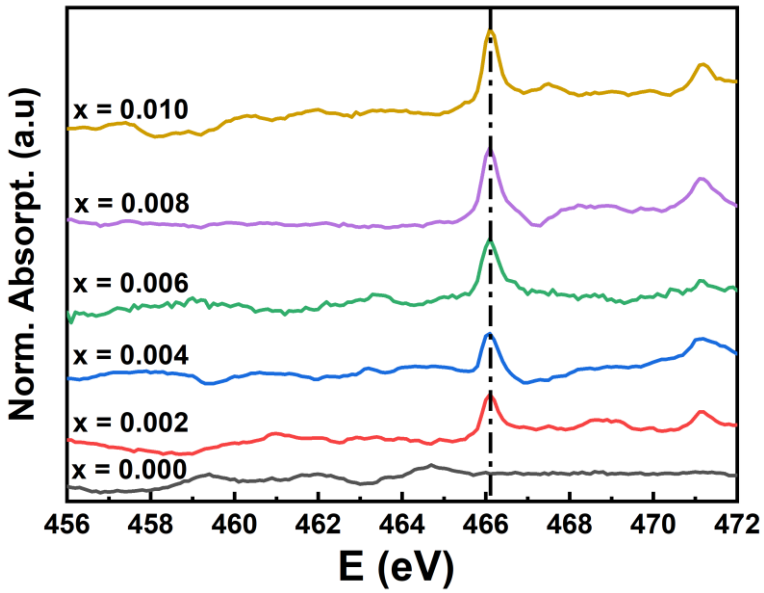

Figure 4.9. Ti $L_{2,3}$-edge spectra of $(Bi_{1.6}Pb_{0.4}Sr_2Ca_2Cu_3O_{10+\delta})_{1-x}(TiO_2)_x$ samples, with x = 0, 0.002, 0.004, 0.006, 0.008, and 0.010.

To confirm the presence of titanium incorporation in all the added samples, Ti-$L_{2,3}$-edge spectra were obtained. The plot of the XANES Ti-$L_{2,3}$-edge is shown in Figure 4.9. The Ti-L_2 and Ti-L_3 peaks were observed in all the added samples, with distinct absorption peaks compared to the pure sample. Absorption peaks at 466 and 471 eV were prominently visible only in the added

samples, indicating the presence of TiO_2 nanoparticles in the crystal structure of the superconductor. The absorption per mass unit steadily increased with the addition of TiO_2 content. These spectra confirmed that there was no variation in the ionic state of titanium. In comparison with the report by Kravtsova *et al.*, the energy range of obtained L_2 peaks likely suggests that TiO_2 nanoparticles were not in the form of nano-clusters and diffused well in the crystal lattice [47]. This observation is consistent with the appearance of normal core point-like pinning centers and also possibly indicates a high degree of substitution of the Titanium ions [77]. The homogeneous characteristics of Ti^{4+} ionic properties in all the added samples confirm that the substitution was intensified only by the addition of TiO_2 content and did not involve multivalence of the dopant.

The impact of adding TiO_2 nanoparticles on the local structure and interlayer coupling of the $Bi_{1.6}Pb_{0.4}Sr_2Ca_2Cu_3O_{10+\delta}$ polycrystalline superconductor, resulting in a decrease in T_c, was comprehensively investigated. The analysis of excess conductivity within the frameworks of the A–L and L–D theories revealed that TiO_2 induced fluctuations in the mean field region. These fluctuations were accompanied by an increase in the *c*-axis coherence length and effective CuO_2 interlayer spacing. Consequently, the interlayer coupling strength decreased progressively with increasing TiO_2 content. These findings were consistent with the observed increases in the Cu-O, Cu-Ca, and Cu-Sr bond distances. Furthermore, the addition of TiO2 led to a reduction in both the Cu valence state and hole concentration, as evidenced by Cu K-edge and Cu $L_{2,3}$-edge XANES spectra. These changes were correlated with the variations in the local structure and the decrease in T_c in the. The correlation between local structure variations and T_c of the $(Bi_{1.6}Pb_{0.4}Sr_2Ca_2Cu_3O_{10+\delta})_{1-x}(TiO_2)_x$ was possibly found.

4.4. IMPROVEMENTS OF J_c

Although the results given in 4.2.1 pointed out that the additions of TiO_2 nanoparticles decelerated the formation of the Bi-2223 phase, the additions were expected to enhance J_c of the fabricated samples. The field-dependent critical current density (J_c) of all samples was analyzed using the modified Bean's model, as described in section 2.2.2.2. The results of the external field dependence of J_c for all samples at various temperatures (65 K, 55 K, 45 K, and 35 K) are presented in Figure 4.10(a–d).

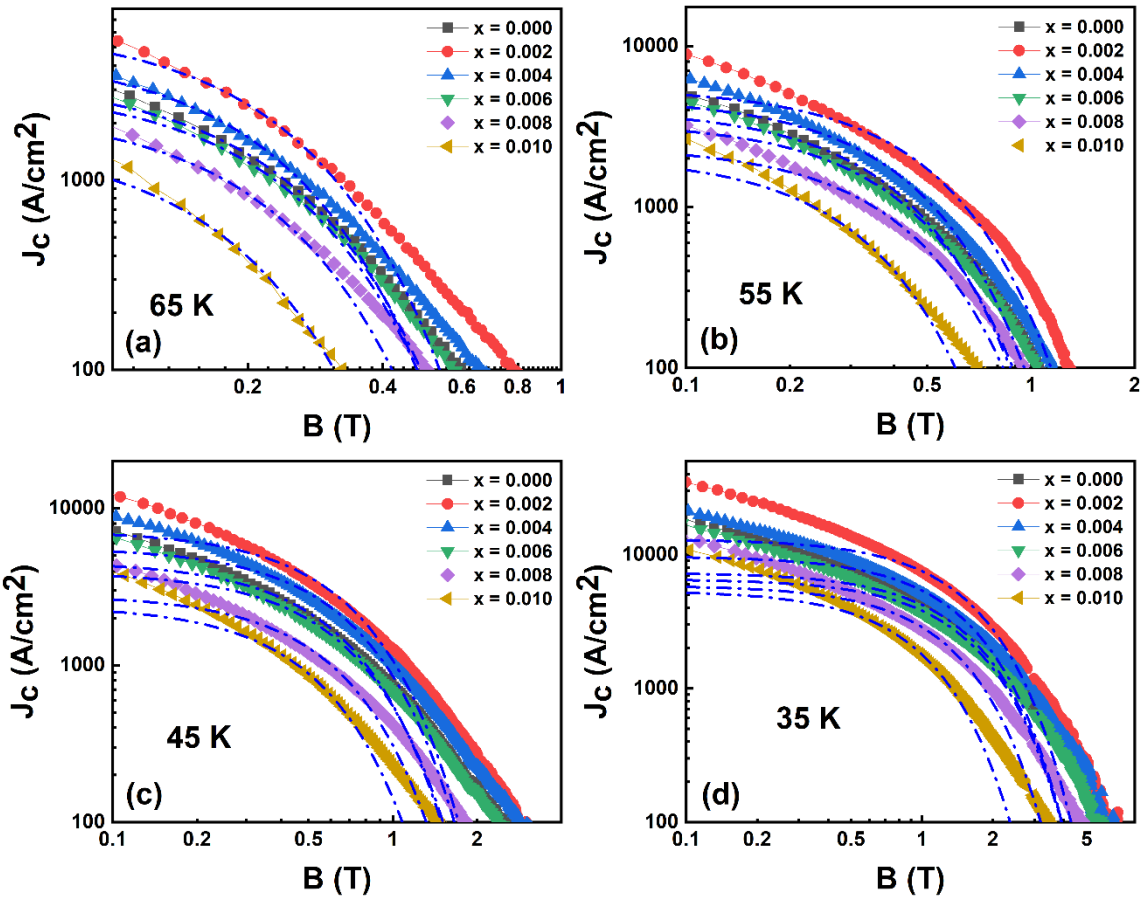

Figure 4.10. The field dependence of J_c of $(Bi_{1.6}Pb_{0.4}Sr_2Ca_2Cu_3O_{10+\delta})_{1-x}(TiO_2)_x$ samples, with x = 0, 0.002, 0.004, 0.006, 0.008, and 0.010 with small bundle regimes description using collective pinning theory at (a) 65 K, (b) 55 K, (c) 45 K, and (d) 35 K. Dash-dot lines are fitting curves using Equation (1.2).

The external field dependency of J_c for all samples was plotted at temperatures of 65 K, 55 K, 45 K, and 35 K, represented in Figure 4.10(a–d). For the sample without TiO_2 addition, the J_c values were found to be in line with previous reports on BPSCCO polycrystalline samples [72,96,114]. Remarkably, with TiO_2 contents of x = 0.002 and x = 0.004, there was a substantial increase in J_c across all examined magnetic fields and temperature ranges. The most significant improvement in J_c was observed at the x = 0.002 doping level, with a slight decrease noted in the x = 0.004 sample. Moreover, when comparing all the samples, it was evident that J_c exhibited a slower rate of decline under the applied magnetic field in these particular samples. As a result, J_c reached the threshold value of 100 A/cm² at a higher irreversible field compared to the other samples. However, with increasing TiO_2 content, J_c decreased and showed a more rapid decline under the influence of an external magnetic field, particularly in the x = 0.010 sample. These findings indicate that TiO_2 nanoparticles can act as additional pinning centers, leading to an improvement in J_c under external magnetic field conditions when added at the right addition [23,65,76,114]. The observed reduction in J_c in the x = 0.006, 0.008, and 0.010 samples might be attributed to a decrease in inter-grain connectivity, as evidenced by XRD and SEM analyses.

The study aimed to investigate the impact of TiO_2 nanoparticles and identify the optimal doping level for enhancing the critical current density (J_c). However, a deeper understanding of how TiO_2 nanoparticles influence each specific magnetic field regime and the underlying flux pinning mechanism was necessary. The collective pinning theory, as formulated by Blatter et al., provided a framework for analyzing the vortex pinning mechanism and elucidating the behavior of vortices in high-temperature superconductors [14,55]. According to this theory, J_c exhibits distinct characteristics in different

magnetic field regimes. Generally, J_c in a magnetic field can be divided into three regimes: the single vortex regime, the small bundle regime, and the large bundle regime, separated by crossover fields known as B_{sb} and B_{lb} [14,34,80,99,105,106]. B_{sb} marks the transition from the single vortex regime to the small bundle regime, while B_{lb} denotes the transition from the small bundle regime to the large bundle regime. In the single vortex regime, where vortices are individually pinned, J_c in the magnetic field is nearly constant. Interestingly, for samples with x = 0.002 and x = 0.004, the plateau in J_c was wider, indicating an increase in the number of pinning centers. As the magnetic field intensity increased, the vortex density surpassed the pinning center density, leading to collective pinning [14,16,34,105].

The fitting curves in the temperature range of 65 K, 55 K, 45 K, and 35 K, using Equation 1.2, are depicted as solid red lines in Figure 4.10(a–d). Based on the fitting results in the small-bundle regime, the values of the crossover fields B_{sb} and B_{lb} were identified as the points where the deviation occurred at lower and higher fields, respectively. This estimation method employed $-\log[J_c(B)/J_c(0)]$ as a function of B in a double-logarithmic plot, following the approach by Ghorbani *et al*. [24]. The B_{sb} and B_{lb} values are presented in Table 4.3. The B_{sb} and B_{lb} values increased with higher doping levels (x = 0.002 and x = 0.004) and decreased at higher adding content. The increments in B_{sb} and B_{lb} were more significant at the lower temperatures. About the x = 0.002 sample, the B_{sb} value at 65 K was only 0.01 T higher than the pure one, whereas the B_{sb} value at 35 K was 0.08 T higher than that. Similarly, the B_{lb} value for this sample was 0.06 T higher at 65 K and 0.34 T higher at 35 K compared to the non-doped sample.

The increment in B_{sb} for the x = 0.002 and x = 0.004 samples suggested an extension of the single vortex regime, which could be linked to the increased

quantity of pinning centers. Moreover, the increase in B_{lb} for these samples indicated that the additional pinning centers were effectively contributing to the collective pinning regime. The presence of sufficient TiO_2 content extended both the small and large bundle regimes, correlating with the enhancement of J_c at high external magnetic fields. In the single vortex regime, where the magnetic field is lower than B_{sb}, individual vortices were pinned by pinning centers [34,61,105]. Therefore, the expansion of the single vortex regime was likely attributed to the introduction of additional nano-defects as supplementary pinning centers [34,61,105]. These artificial pinning centers also demonstrated efficient collective pinning capabilities by extending the small bundle regime.

Table 4.3. B_{sb} and B_{lb} values of $(Bi_{1.6}Pb_{0.4}Sr_2Ca_2Cu_3O_{10+\delta})_{1-x}(TiO_2)_x$ samples, with x = 0, 0.002, 0.004, 0.006, 0.008, and 0.010 at 65 K, 55 K, 45 K, and 35 K.

x	T = 65 K		T = 55 K		T = 45 K		T = 35 K	
	B_{sb} (T)	B_{lb} (T)	B_{sb} (T)	B_{lb} (T)	B_{sb} (T)	B_{sb} (T)	B_{lb} (T)	B_{sb} (T)
0.000	0.138	0.290	0.227	0.530	0.370	0.830	0.730	1.800
0.002	0.150	0.300	0.277	0.650	0.430	0.950	0.820	2.500
0.004	0.140	0.290	0.253	0.587	0.410	0.870	0.800	1.930
0.006	0.135	0.285	0.227	0.538	0.350	0.840	0.670	1.750
0.008	0.128	0.280	0.215	0.514	0.300	0.800	0.580	1.730
0.010	0.125	0.270	0.200	0.470	0.280	0.670	0.450	1.420

4.5. FLUX PINNING PROPERTIES

4.5.1. Flux pinning mechanism

In light of the substantial improvement in J_c, it becomes imperative to investigate the flux pinning mechanism of TiO_2 nanoparticles in the BSCCO polycrystalline superconductor. In type-II superconductors, the core interaction stands as the most effective vortex-pinning center interaction [55,61,80].

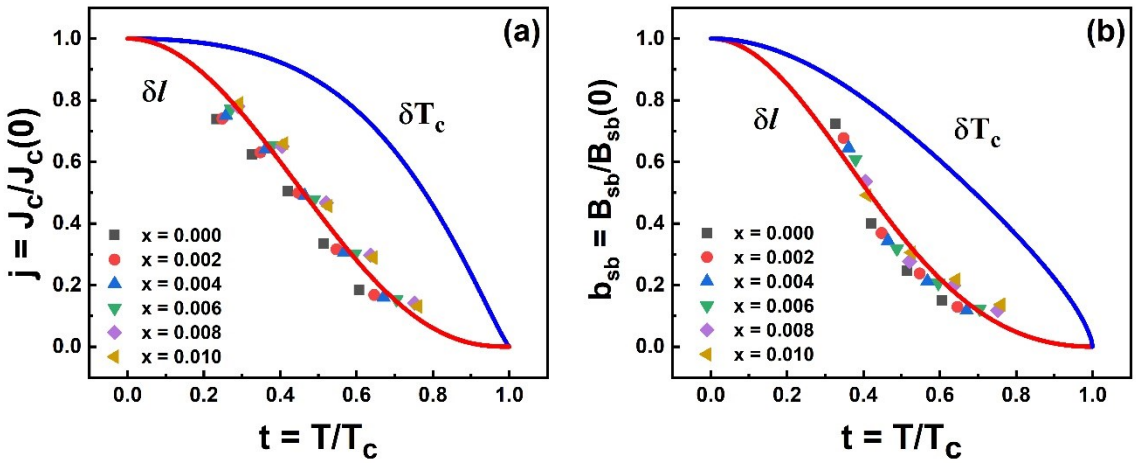

Figure 4.11. (a) The normalized temperature dependence of normalized J_c and (b) normalized B_{sb} of $(Bi_{1.6}Pb_{0.4}Sr_2Ca_2Cu_3O_{10+\delta})_{1-x}(TiO_2)_x$ samples, with x = 0, 0.002, 0.004, 0.006, 0.008, and 0.010. Solid lines are fitting curves in terms of the δl pinning and δT_c pinning mechanisms using Eqs. 1.5 and 1.6

The Figure 4.11(a) illustrates the presentation of the normalized critical current density ($j = J_c(T)/J_c(0)$) versus the normalized temperature $t=T/T_c$ for all the samples. The dominant pinning mechanism in all samples is δl, which is related to the variation in charge carrier mean free path near lattice defects [24,55,80,106]. This outcome aligns with the findings reported in other studies concerning YBCO and BSCCO [55,61].

Additionally, we evaluated the normalized small bundle field, denoted as b_{sb} (= $B_{sb}(t)/B_{sb}(0)$) values of the $(Bi_{1.6}Pb_{0.4}Sr_2Ca_2Cu_3O_{10+\delta})_{1-x}(TiO_2)_x$ samples at 65 K, 55 K, 45 K, and 35 K were estimated through fitting using the expressions mentioned and depicted the results Figure 4.11(b). Interestingly, the δl-pinning exhibits a remarkable agreement with the B_{sb} data. This consistency reaffirms the prevalence of the δl mechanism in both the undoped and doped samples at all temperatures, which correlates well with the j-t analysis discussed earlier. The natural pinning center is attributed to grain

boundaries in the pure sample, and δl pinning is a plausible explanation for this type of center. These additional pinning centers were also expected to introduce variations in the mean free path of charge carriers, which are associated with defects, distortions, and dislocations, as revealed in the XRD, SEM, and RT examinations. Further details regarding the properties of foreign pinning centers are discussed below.

4.5.2. Improvements of pinning force density

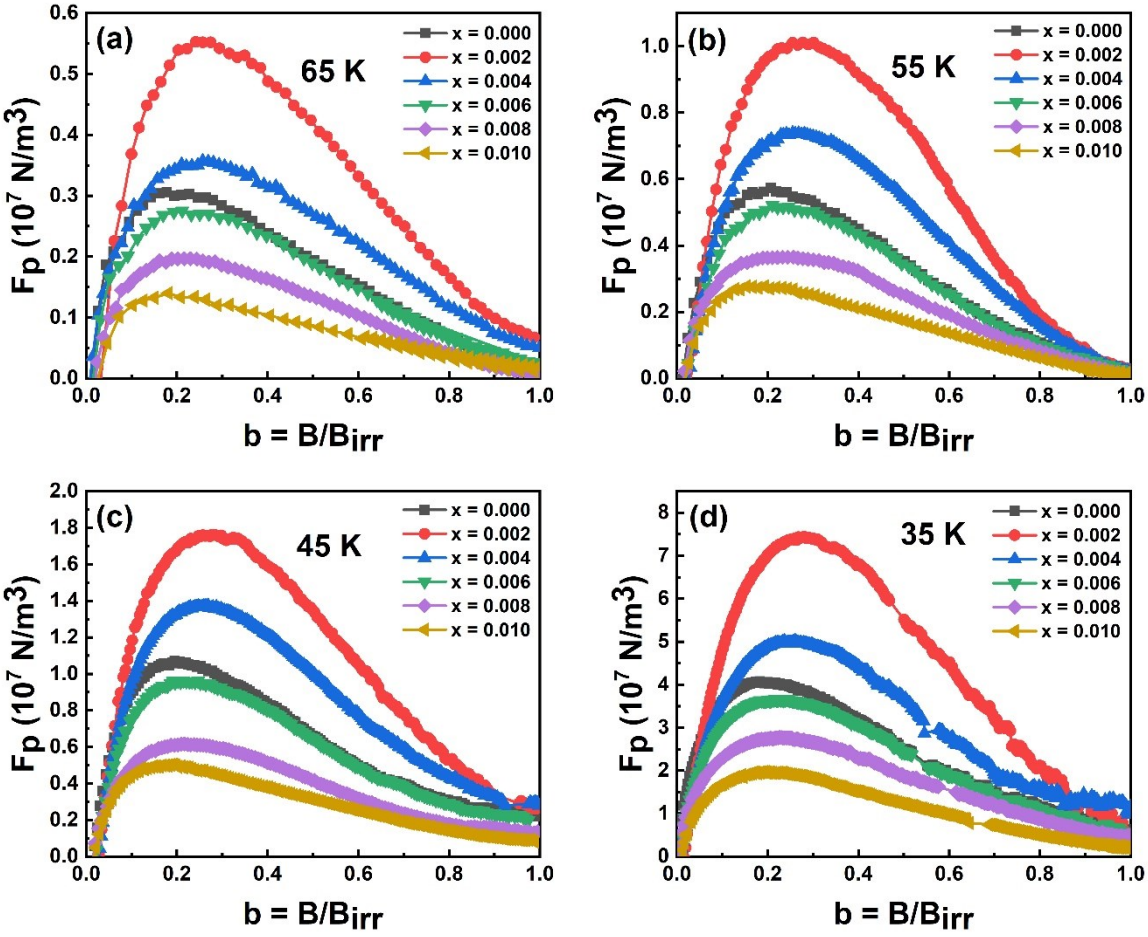

Figure 4.12. The normalized field dependence of flux pinning force density of $(Bi_{1.6}Pb_{0.4}Sr_2Ca_2Cu_3O_{10+\delta})_{1-x}(TiO_2)_x$ samples, with x = 0, 0.002, 0.004, 0.006, 0.008, and 0.010 at (a) 65 K, (b) 55 K, (c) 45 K, and (d) 35 K.

The flux pinning force density of all samples was also estimated using the relation: $F_p = J_c \times B$. To illustrate the changes in flux pinning properties, the F_p of all samples at 65, 55, 45, and 35 K as a function of the normalized field $b = B/B_{irr}$ was presented in Figure 4.12(a–d), where B_{irr} was defined using a criterion of J_c = 100 A/cm^2. The pinning strength was improved significantly on the x = 0.002 and x = 0.004 samples. For the non-added sample, the maximal F_p ($F_{p,max}$) values were 0.3×10^7, 0.5×10^7, 1.5×10^7, and 4×10^7 N/m^3 at 65 K, 55 K, 45 K, and 35 K, respectively. On the optimal added sample, x = 0.002, $F_{p,max}$ reached 0.4×10^7, 0.9×10^7, 1.7×10^7, and 7×10^7 N/m^3 at the appropriated temperatures. In addition to the improvement in strength, the most significant observation in the F_p-b results was the shift in the position $F_{p,max}$ (b_{peak}), indicating a change in the dominant pinning centers in the doped samples. This shift necessitates further analysis using the Dew-Hughes model [38]. The exact values of b_{peak} were estimated through the fitting process and are presented in Table 4.4.

4.5.3. Identification of flux pinning center

The f_p as a function of b along with the fitting lines according to the Dew-Hughes model of all samples is presented in Figure 4.13(a–d). The values of p and q are listed in Table 4.4. Notably, the fitting parameters for each sample exhibit similarity across all investigated temperatures. Generally, the q values of samples at all temperatures are approximately ~2, indicative of core interaction [20]. Therefore, it's possible to use the average p or b_{peak} values for each sample to analyze the dominant type of pinning centers. For the non-added sample, the average values of p and b_{peak} were 0.554 and 0.209, which correspond to the normal core surface pinning center (p = 0.5) [20]. This is consistent with previous studies defining grain boundaries as the natural

pinning centers for BPSCCO polycrystalline superconductors, which are categorized as normal core surface pinning centers [102,112].

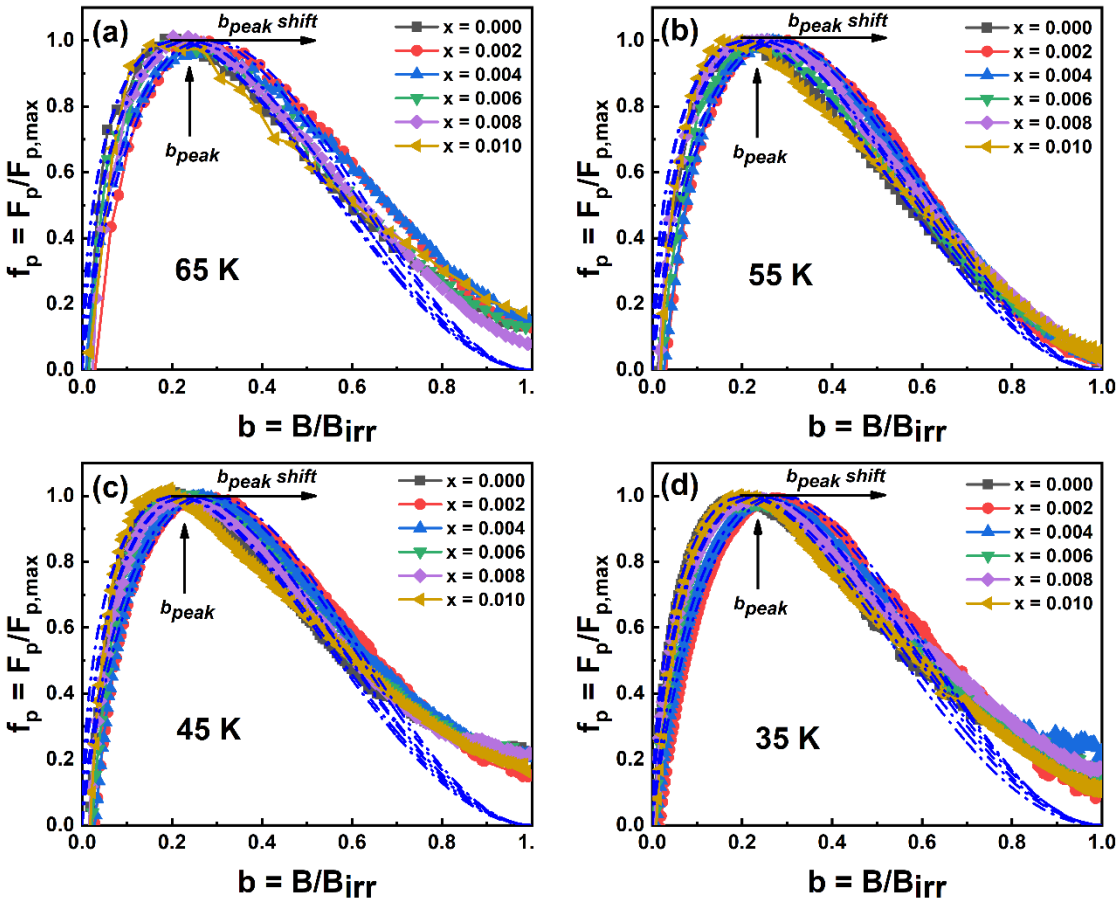

Figure 4.13. The normalized field dependence of $(Bi_{1.6}Pb_{0.4}Sr_2Ca_2Cu_3O_{10+\delta})_{1-x}(TiO_2)_x$ samples, with x = 0, 0.002, 0.004, 0.006, 0.008, and 0.010 with modified Dew-Hughes model scaling at (a) 65 K, (b) 55 K, (c) 45 K ,and (d) 35 K. Solid lines are fitting curves using Eq. (1.7).

For x = 0.002, the value of p increased to 0.813 with b_{peak} of 0.289, matching the observed shift in $F_{p,max}$ position observed in Figure 4.12. However, by adding content increment, the value of p fell back to 0.752, 0.621, 0.607, and 0.509, respectively. This behavior can be explained by considering the size of the TiO_2 nanoparticle dopant. The TEM images in Figure 4.1, the

average size of the TiO_2 nanoparticles was around 12 nm, which was in between the coherence length (~ 2.9 nm) and the penetration depth (~ 60 nm) of BPSCCO [20,30,108]. According to Dew-Hughes's model, when the size of the pinning center is smaller than the penetration depth, the interaction between flux lines and pinning centers is characterized as core interaction [20].

Moreover, when the pinning center size is larger than the coherence length, it's classified as a normal center. Furthermore, when compared to the inter-flux-line spacing d_ϕ, the average size of the TiO_2 nanoparticles is smaller across the entire range of magnetic fields investigated [20,102]. Therefore, the geometry of the center aligns with the characteristics of point-like pinning centers. Thus, the added TiO_2 nanoparticles function as normal core point pinning centers in the doped samples, corresponding to $p = 1$ and $q = 2$ in Dew-Hughes's model [20,44]. This explanation clarifies the increase in the p value in the doped samples. However, the value of p decreases with increasing x, indicating a re-occupation of the normal core surface pinning centers. This phenomenon is related to the presence of misoriented grains, voids, and porosity as indicated by XRD and SEM analysis.

SEM examination shows that the surface structure of the doped samples exhibits grain misorientation, porosity, and voids, particularly in samples with higher dopant content. The monotonic decrease in T_c values with increasing TiO_2 content is in agreement with this. The presence of TiO_2 is also linked to the increase in ρ_0 through Zou-Anderson fitting. In terms of $J_c(B)$, the samples benefited from adequate amounts of TiO_2 nanoparticles, particularly $x = 0.002$, 0.004. Within the framework of collective pinning theory, J_c in the small bundle regime was well-fitted. The values of B_{sb} and B_{lb} were estimated for all samples at 65, 55, 45, and 35 K. These results indicated that the small and large bundle regimes extended with sufficient amount of TiO_2 nanoparticles. The *j(t)*

analyses demonstrated that δl pinning was the dominant pinning mechanism in all samples. The investigation of the normalized field dependence of f_p helped clarify the influence of TiO_2 nanoparticles on the flux pinning mechanism through the Dew-Hughes model. The increase in the fitting parameter p in x = 0.002 and 0.004 samples suggests that the additional centers are normal core point pinning centers. Conversely, higher dopant content led to decreased p values due to the presence of misoriented grains, voids, and porosity.

Table 4.4. Flux pinning centers properties with modified Dew-Hughes model scaling of $(Bi_{1.6}Pb_{0.4}Sr_2Ca_2Cu_3O_{10+\delta})_{1-x}(TiO_2)_x$ samples, with x = 0, 0.002, 0.004, 0.006, 0.008, and 0.010 at 65 K, 55 K, 45 K, and 35 K.

x	T = 65 K			T = 55 K		
	p	q	b_{peak}	p	q	b_{peak}
0.000	0.514	1.934	0.210	0.534	2.009	0.213
0.002	0.813	1.998	0.289	0.821	2.018	0.293
0.004	0.752	1.998	0.273	0.763	2.027	0.269
0.006	0.621	1.983	0.238	0.644	2.056	0.250
0.008	0.607	1.963	0.236	0.597	1.931	0.237
0.010	0.509	1.961	0.206	0.518	1.996	0.211
x	T = 45 K			T = 35 K		
	p	q	b_{peak}	p	q	b_{peak}
0.000	0.517	1.910	0.221	0.524	1.847	0.211
0.002	0.823	1.986	0.290	0.848	2.076	0.302
0.004	0.758	2.060	0.277	0.766	1.999	0.281
0.006	0.627	1.881	0.247	0.633	1.930	0.241
0.008	0.601	1.935	0.241	0.591	1.861	0.238
0.010	0.518	1.937	0.208	0.548	2.087	0.217

4.6. CONCLUSION OF CHAPTER 4

The effects of TiO_2 nanoparticles on the structure, morphology, critical and flux pinning properties of $Bi_{1.6}Pb_{0.4}Sr_2Ca_2Cu_3O_{10+\delta}$ superconductor were systematically investigated. The $(Bi_{1.6}Pb_{0.4}Sr_2Ca_2Cu_3O_{10+\delta})_{1-x}(TiO_2)_x$ polycrystalline samples were successfully fabricated via the solid-state reaction method. XRD investigation results showed that the TiO_2 nanoparticles decelerated the Bi-2223 phase formation. SEM examination presented the degradation of the surface structure of added samples with grain misorientation, porous, and void, especially on samples with high adding content. The T_c values of the samples were decreased monotonously by TiO_2 content with significant descend from $x = 0.006$. This negative effects of TiO_2 nanoparticle adding was systematically with evidences in local structure. The excess conductivity in the framework of the A–L and L–D theory analyses displayed that the mean field region was fluctuated by TiO_2 with increasing c-axis coherence length and effective CuO_2 interlayer spacing. As a consequence, the interlayer coupling strength declined monotonously with adding content. The reduction in both Cu valence state and hole concentration on the added sample was probed by using Cu K-edge and Cu $L_{2,3}$-edge XANES spectra. The correlation between local structure variations and T_c of the $(Bi_{1.6}Pb_{0.4}Sr_2Ca_2Cu_3O_{10+\delta})_{1-x}(TiO_2)_x$ was possibly found.

Beyond these descend, the additions of TiO_2 nanoparticles were essential agent on J_c and flux pinning enhancements. The $J_c(B)$ of the samples were enhanced by adequate adding contents of $x = 0.002$, 0.004. In the collective pinning theory framework, the J_c in the small bundle regime is well fitted. The values of B_{sb} and B_{lb} were estimated for all samples at 65, 55, 45, and 35 K. The results revealed the extension of the small and large bundle regimes with adequate amounts of TiO_2 nanoparticles. The $j(t)$ analyses exhibited that the δl

pinning was the dominant pinning mechanism in all samples. The normalized field dependence of f_p was investigated to clarify the influence of TiO_2 nanoparticles in the flux pinning mechanism via Dew–Hughes model. The increasing p fitting parameter increase on x = 0.002 and 0.004 samples exhibited that the additional centers were normal core point pinning centers. On higher adding content, p values were decreased by the presence of misoriented grains, void, and porous.

CHAPTER 5: IMPROVEMENTS OF CRITICAL CURRENT DENSITY IN HIGH-T_c $Bi_{1.6}Pb_{0.4}Sr_2Ca_2Cu_3O_{10+\delta}$ SUPERCONDUCTOR BY ADDITION OF MAGNETIC Fe_3O_4 NANOPARTICLE

In Chapter 4, results showed that the non-magnetic nanoparticles effectively served as pinning centers in BPSCCO, leading to the obvious enhancements of J_c. TiO_2 semiconducting nanoparticles were clearly proved to effectively serve as 0D pinning centers. In the next research, the additions of the another type of nanoparticles having a similar range of diameters but owning higher potential to pin the penetrated vortices are going to be carried out. Since vortices have been identified to be flux quanta, pinning centers in forms of magnetic nanoparticles might play an important role in flux pinning mechanism. For more details, magnetite nanoparticle with the dimension mentioned above are characterized as ferromagnetic material, which has been known as the strongest pinning type. Among the magnetic nanoparticles, Fe_3O_4 nanoparticles have been chosen due to the reasons that Fe_3O_4 are oxide and stable at high sintering temperatures. This chapter will examine the effect of addition of Fe_3O_4 magnetic nanoparticles on crystal structure and superconducting properties of BPSCCO samples. The expected benefits of the addition of the Fe_3O_4 nanoparticles are that the magnetic pinning centers would attract and pin more penetrated vortices inside the BPSCCO samples. The stoichiometry of samples has been $(Bi_{1.6}Pb_{0.4}Sr_2Ca_2Cu_3O_{10+\delta})_{1-x}(Fe_3O_4)_x$, where x = 0.00, 0.01, 0.02, 0.03, 0.04 and 0.05.

5.1. NANOPARTICLE CHARACTERISTICS

The TEM images of the Fe_3O_4 nanoparticles and their histogram before the adding process was examined and shown in Figure 5.1. The nanoparticles were found to be mostly in spherical form and its average size was about 19 nm. The average size of the Fe_3O_4 nanoparticles is also adaptable as a dopant

for BPSCCO, which was between the coherence length and the penetration of the compound.

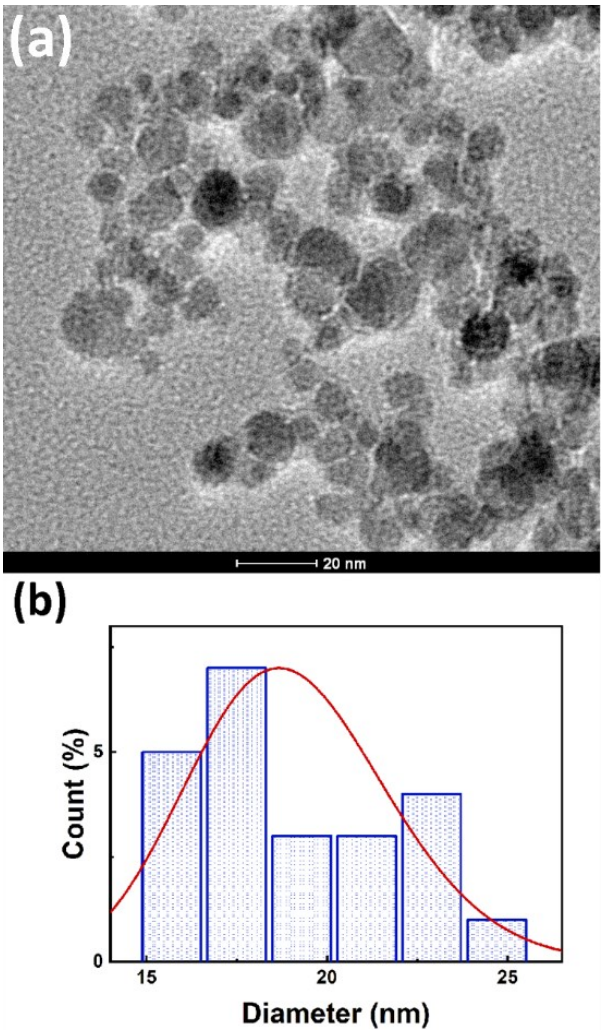

Figure 5.1. (a) TEM images and (b) histogram of Fe_3O_4 nanoparticles.

5.2. FORMATION OF THE SUPERCONDUCTING PHASES

5.2.1. Phase analysis

The X-ray diffraction (XRD) patterns of the samples are displayed in Figure 5.2. These patterns clearly indicate the presence of two main phases: Bi-2223 (marked as "H") and Bi-2212 (marked as "L"). Additionally, there is a secondary phase, Ca_2PbO_4, formed due to the substitution of Pb [96].

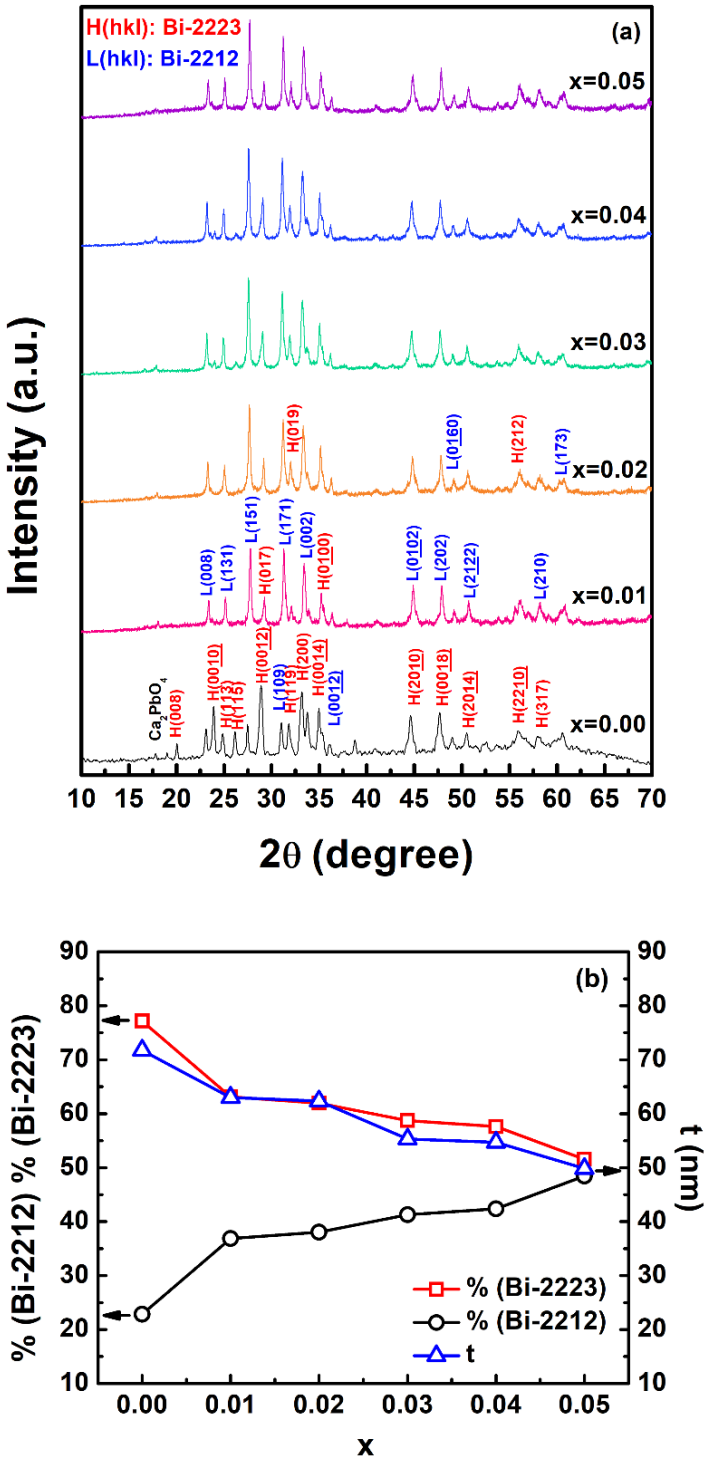

Figure 5.2. (a) XRD patterns and (b) Volume fractions and average crystalline size of $(Bi_{1.6}Pb_{0.4}Sr_2Ca_2Cu_3O_{10+\delta})_{1-x}(Fe_3O_4)_x$ samples, with x = 0, 0.01, 0.02, 0.03, 0.04, and 0.05.

In the non-added sample, the Bi-2223 phase is dominant and shows a high degree of *c*-axis orientation, evident from the strong H(00*l*) peaks. The volume fractions of the superconducting phases, *%Bi-2223* and *%Bi-2212*, were calculated. Moreover, the average crystallite size of the Bi-2223 grains was estimated using the Scherrer equation [96]. In comparison, as the dopant content increased, the *%Bi-2223* phase consistently decreased, while the *%Bi-2212* phase increased. Simultaneously, the average crystallite size of the Bi-2223 grains decreased continuously. These observations suggest that the presence of Fe_3O_4 nanoparticles likely decelerated the formation of the Bi-2223 phase. Despite this, no peaks related to iron were observed, which could be attributed to the relatively low concentration of Fe_3O_4 in these samples. To further investigate, the $x = 0.05$ was examined using Fe-edge X-ray absorption spectra in my independent article [97]. The XRD refinement results indicated a subtle shift in the spectra of the doped samples, hinting at the potential partial substitution of Fe ions into the BSCCO crystal structure [97].

5.2.2. Surface morphology

The scanning electron microscopy (SEM) images of all the samples are presented in Figure 5.3. In these images, the Bi-2223 phase is observed in the form of plate-like grains, while the Bi-2212 phase appears as needle-like grains, as previously noted [96]. Additionally, fine Fe_3O_4 nanoparticles are visible as randomly distributed dots adhering to the surfaces and boundaries of the grains in the doped samples. Up to $x = 0$–0.02, the microstructures of the samples do not show significant changes. However, in the $x = 0.03$–0.05samples, a portion of the plate-like grains has transformed into needle-like grains. This transformation may have contributed to an increase in the surface porosity of these samples. Such changes in microstructure indicate that the inter-grain connectivity can be compromised in samples with higher doping levels.

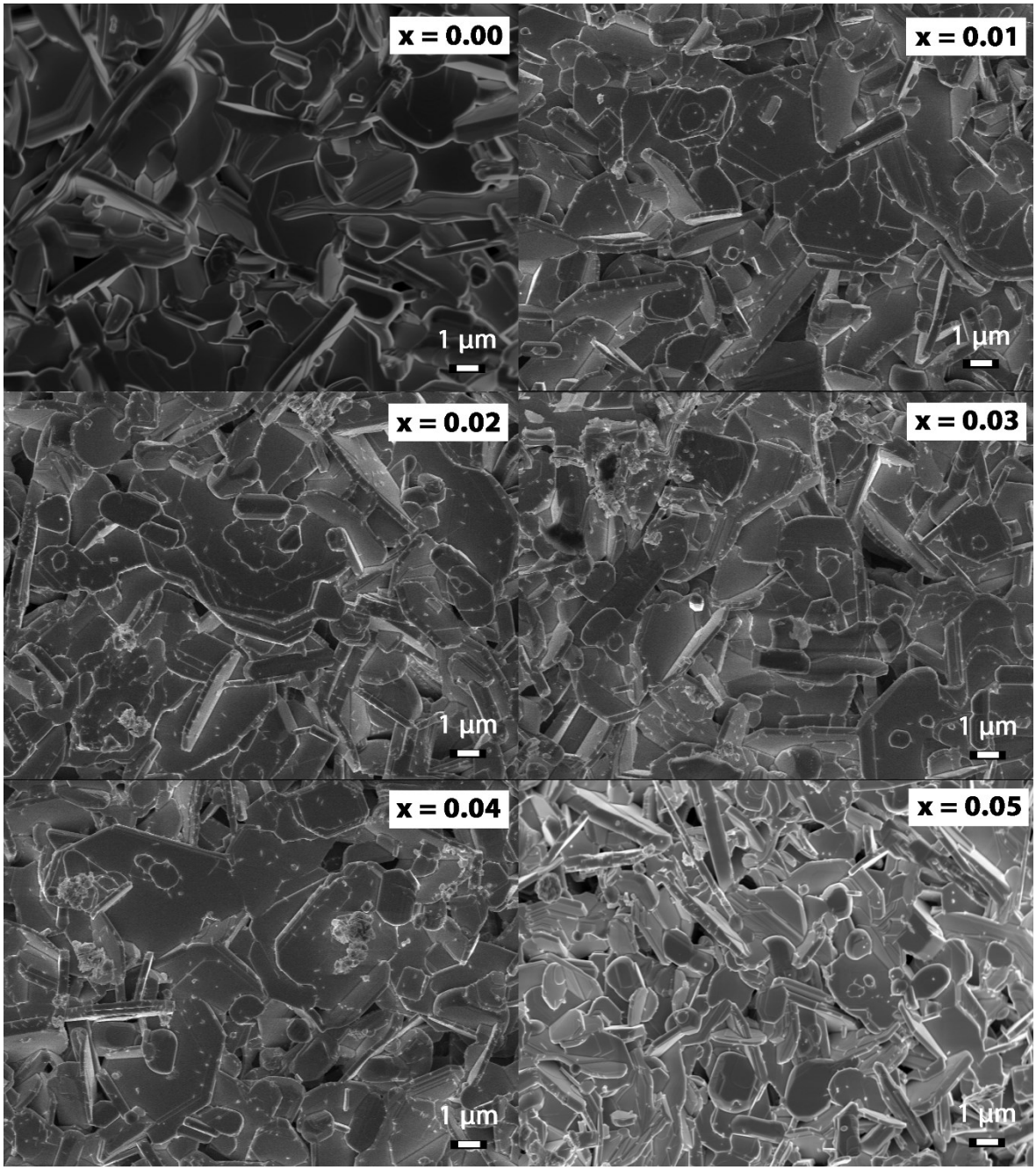

Figure 5.3. SEM images of $(Bi_{1.6}Pb_{0.4}Sr_2Ca_2Cu_3O_{10+\delta})_{1-x}(Fe_3O_4)_x$ samples, with x = 0, 0.01, 0.02, 0.03, 0.04, and 0.05.

5.3. IMPROVEMENTS OF J_c

Figure 5.4(a) illustrates the field dependence of J_c at 65 K in double-logarithmic scale with the exponential fitting lines for small bundle regime by using Equation 1.2.

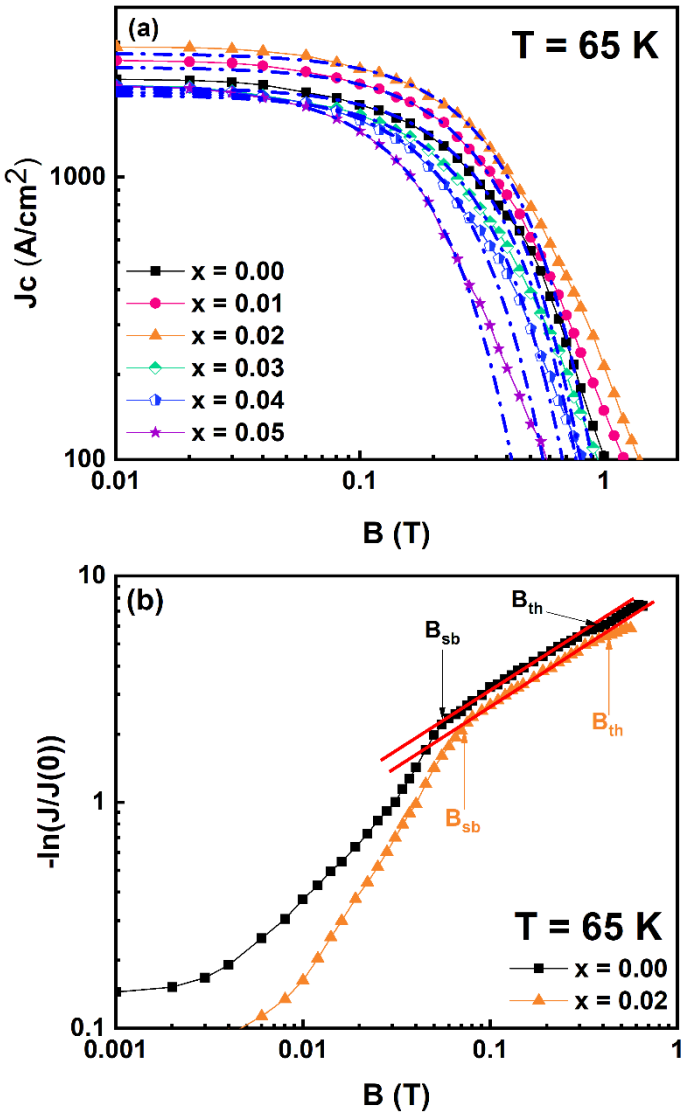

Figure 5.4. (a) Field dependence of J_c at 65 K with small-bundle regime fitting in double-logarithmic scale, (b) field dependence of $-\ln[J_c(B)/J_c(0)]$ of the x = 0 and 0.02 samples.

The results clearly demonstrate that the J_c values of the added samples increased for x = 0.01 and 0.02, and this enhancement was most significant for the x = 0.02 sample. However, the J_c values gradually decreased for $x \geq 0.03$. This decline in J_c for the $x \geq 0.03$ samples can be attributed to the observed

degradation in interconnectivity, as revealed in the SEM analyses. The influence of adding Fe_3O_4 nanoparticles varies across different field regions, and this behavior can be explained by the collective pinning theory [14,55,61]. The collective pinning theory divides the J_c behavior into three specific in-field regimes: the single vortex regime, the small bundle regime, and the large bundle regime. These regimes are separated by two characteristic fields small-bundle regime field B_{sb} and large bundle regime field B_{lb} [14,25,106]. The field dependence of $-\ln[J_c(B)/J_c(0)]$ of the $x = 0$ and 0.02 samples is depicted in Figure 5.4(b), with a fitting line based on Eq. 5.1. By analyzing the deviation points at lower and higher fields, the values of B_{sb} and B_{lb} were determined, as presented in Table 5.1. The results showed that the small bundle regime was slightly extended for the $x = 0.01$ and 0.02 samples, indicating improved vortex pinning in this regime. Conversely, for the $x \geq 0.03$ samples, J_c decreased more rapidly in the in-field conditions. The small porosity observed in the $x = 0.01$ and 0.02 samples may have contributed to enhanced inter-grain connectivity, facilitating improved current flow, as suggested by the SEM analysis.

5.4. FLUX PINNING PROPERTIES

5.4.1. Identification of pinning center

The flux pinning force density was estimated as $F_p = J_c \times B$ to gain further insights into the impact of Fe_3O_4 nanoparticles on BPSCCO [96]. The normalized field $b = B/B_{irr}$, B_{irr} was determined using the criterion $J_c = 100$ A/cm^2, dependence of F_p at 65 K is illustrated in Figure 5.5(a) [25]. F_p obviously increased significantly for the $x = 0.01$ and 0.02 samples but not for the $x \geq 0.03$ samples. This indicates that Fe_3O_4 nanoparticles acted as additional pinning centers, enhancing the pinning strength for the $x = 0.01$ and 0.02 samples. Furthermore, the position of maximum F_p ($F_{p,max}$) in all added samples

shifted to a higher normalized field. This observation indicates a change in the flux pinning mechanism.

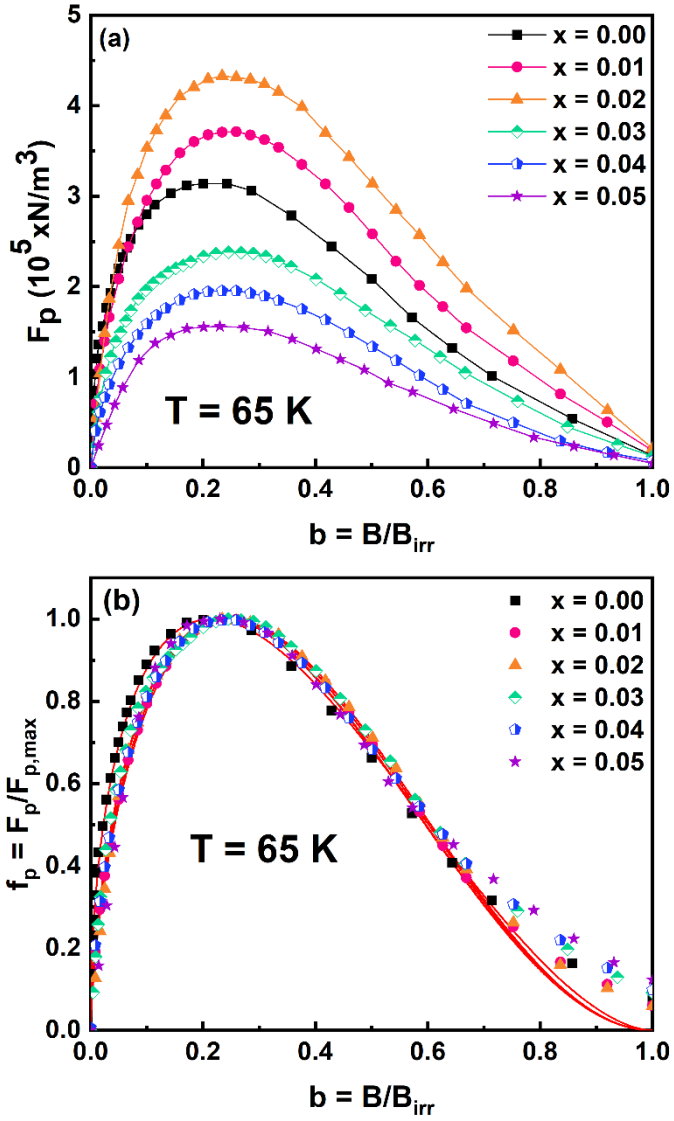

Figure 5.5. (a) Normalized field dependence of F_p at 65 K, (b) normalized field dependence of f_p with Dew–Hughes model fitting of $(Bi_{1.6}Pb_{0.4}Sr_2Ca_2Cu_3O_{10+\delta})_{1-x}(Fe_3O_4)_x$ samples, with x = 0, 0.01, 0.02, 0.03, 0.04, and 0.05.

The flux pinning mechanism, developed by Dew-Hughes for type-II superconductors, has been widely used to investigate pinning center

characteristics in high-temperature superconductors. By fitting the data using Equation 1.7 and presented in Figure 5.6(b), characteristic parameters were determined and are shown in Table 5.1. For the x = 0 sample, the values of p, q, and b_{peak} were ~0.5537, ~2, and ~0.2168, respectively. According to the Dew-Hughes model, the dominant natural pinning centers in polycrystalline $Bi_{1.6}Pb_{0.4}Sr_2Ca_2Cu_3O_{10+\delta}$ superconductors are grain boundaries, with a b_{peak} = 0.2 [20]. For the x = 0.01 and 0.02 samples, the value of p increased from 0.5537 to 0.6523 and 0.6695, and the value of b_{peak} increased from 0.2168 to 0.2459 and 0.2508, respectively, with both exhibiting the point-like pinning mechanism (b_{peak} = 1/3) [20]. Moreover, the q values of all samples were approximately 2, indicating core interaction [20]. The average size of the Fe_3O_4 nanoparticles was ~20 nm, which falls between the coherence length (~ 2.9 nm) and the penetration depth (~ 60 nm) of BPSCCO [56]. Therefore, the additional pinning centers were predicted to be normal core pinning centers [20]. The fitting results showed a slight increase in the p parameters and b_{peak} values on the added samples. his suggests that the flux pinning mechanism in the added samples is a combination of normal core surface and point-like pinning. Point-like pinning centers may form when the size of spherical Fe_3O_4 nanoparticles is smaller than the inter-flux-line spacing d_ϕ, or when Fe ions are partially substituted by superconducting crystals [20,97]. Additionally, Fe_3O_4 nanoparticles located around superconducting grains could act as surface pinning centers [20,44]. In the present study, SEM images frequently revealed misoriented and porous surfaces in the x = 0.03, 0.04, and 0.05 samples. Consequently, the excessive presence of surface pinning centers could lower the value of p in these samples [20,44]. As a result, the b_{peak} values for the x = 0.03, 0.04, and 0.05 samples were reduced to 0.2396, 0.2391, and 0.2383, respectively.

Table 5.1. Characteristic fields and Dew–Hughes model fitting parameters of $(Bi_{1.6}Pb_{0.4}Sr_2Ca_2Cu_3O_{10+\delta})_{1-x}(Fe_3O_4)_x$ samples

x	B_{sb} (T)	B_{lb} (T)	p	q	b_{peak}
0.00	0.055	0.32	0.514	1.934	0.210
0.01	0.065	0.34	0.653	1.994	0.246
0.02	0.080	0.40	0.670	1.988	0.252
0.03	0.050	0.31	0.630	2.015	0.238
0.04	0.040	0.28	0.629	2.021	0.237
0.05	0.030	0.25	0.626	2.032	0.235

5.4.2. Improvements of pinning potential

The thermal activation flux flow using Arrhenius relation was also investigated at B = 0.5 T and presented in Figure 5.7(a)

$$R(T,B) = R_0 exp\left(-\frac{U_0}{k_B}\right), \quad (5.1)$$

where R_0 was the field-independent pre-exponential factor, U_0 is the pinning potential, k_B was the Boltzmann's constant [101,113]. Figure 5.7(b) provides the values of U_0, obtained from the slopes of the linear portion in the Arrhenius plots. It is evident that the potential barrier strengthens until it reaches a maximum in the x = 0.02 sample. However, for the added bulk samples, there is a relatively immediate reduction in U_0/k_B at higher fields. This reduction may be connected to a crossover to a collective flux creep phase, suggesting that weakly pinned intergranular Josephson vortices dominate at these conditions. This vortex motion within the material is related to this dissipative process.

This phenomenon implies that the precipitates at grain boundaries enhance U_0 of the Bi-2223 bulks. However, this pinning effect is insufficient to hold the vortices in place in a strong magnetic field. Therefore, the flux

pinning ability of the samples is enhanced in these samples, consistent with the trends observed in J_c and F_p analyses.

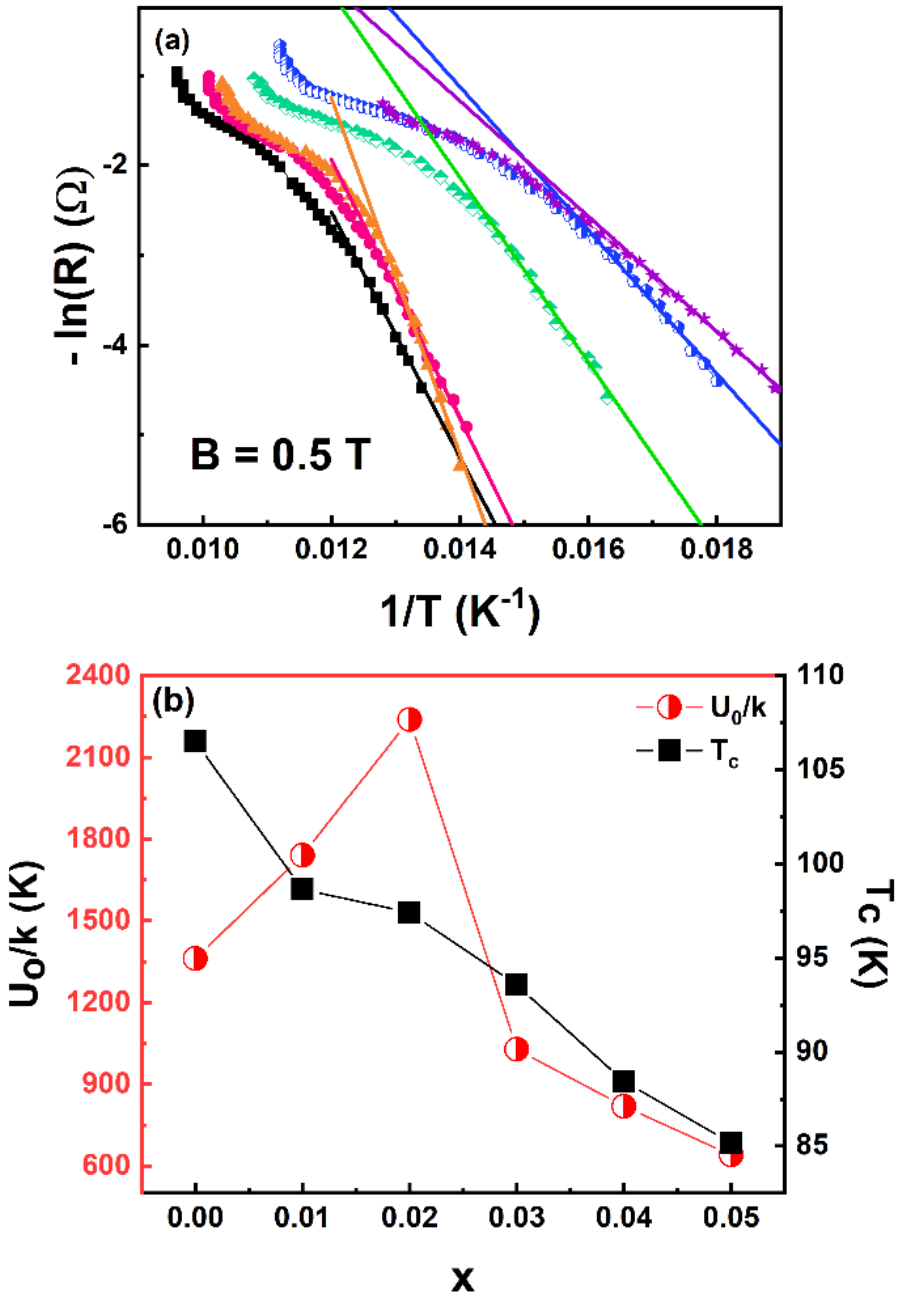

Figure 5.6. (a) Arrhenius plot at 0.5 T using Equation (5.1), and (b) Pinning potential and T_c of $(Bi_{1.6}Pb_{0.4}Sr_2Ca_2Cu_3O_{10+\delta})_{1-x}(Fe_3O_4)_x$ samples, with x = 0, 0.01, 0.02, 0.03, 0.04, and 0.05.

In summary, the $(Bi_{1.6}Pb_{0.4}Sr_2Ca_2Cu_3O_{10+\delta})_{1-x}(Fe_3O_4)_x$ superconductors were successfully fabricated using the solid-state reaction method. Microstructural analyses revealed that the presence of Fe_3O_4 nanoparticles decelerated the formation of the Bi-2223 phase. Samples with $x = 0.01$ and 0.02 showed increased J_c values. These enhancements can be attributed to the improved pinning force (F_p) and the strengthened activation energy (U_0). The Dew-Hughes model was employed to confirm the presence of additional normal core point pinning centers in the added samples.

5.5. COMPARISON OF SUBSTITUTION EFFECT, ADDITIONS OF NON-MAGNETIC AND MAGNETIC NANOPARTICLE ON THE CRITICAL CURRENT DENSITY OF $Bi_{1.6}Pb_{0.4}Sr_2Ca_2Cu_3O_{10+\delta}$ CERAMIC SUPERCONDUCTOR

The influence of substitution and nanoparticle additions on J_c and flux pinning properties of $Bi_{1.6}Pb_{0.4}Sr_2Ca_2Cu_3O_{10+\delta}$ superconductor have been systematically investigated. In general, the sodium substitution, the non-magnetic nanoparticle or also the magnetic nanoparticle are available to enhance the J_c of the BPSCCO polycrystalline samples with proper contents. The optimal content for each dopant has been found, and the J_c has been increased effectively in a wide range of applied magnetic field. Comparison between effect of improvements of J_c by using different methods should be discussed. Figure 5.8 showed the plot of enhancements of J_c of the BPSCCO polycrystalline samples, in which the optimum enhancements of J_c at 65 K obtained by each method were inserted. The results illustrate that the highest enhancement of J_c was achieved by the addition of Fe_3O_4 magnetic nanoparticles with $x = 0.02$. As we expected, the Fe_3O_4 magnetic nanoparticles would have a stronger ability to attract and pin penetrated vortices, leading to induce a stronger pinning force. Consequently, magnetic nanoparticles might

be concluded as the most suitable candidate for enhancements of J_c in type-II superconductors.

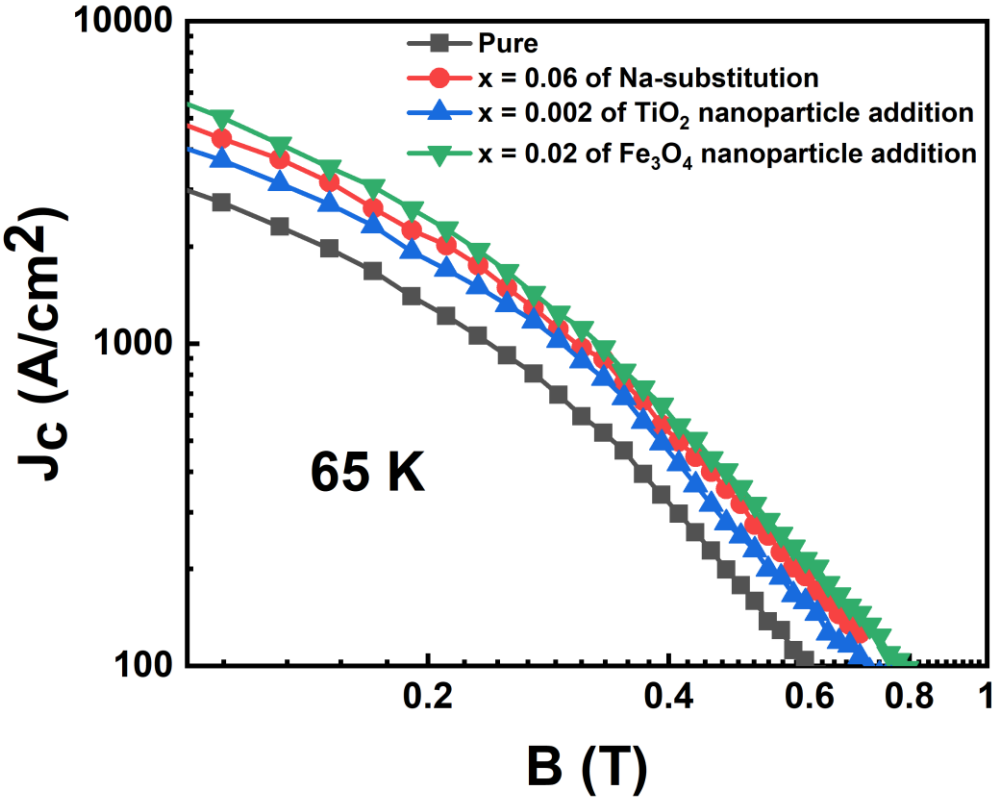

Figure 5.7. The field dependence of J_c at the optimal content of Na-substituted, TiO_2-nanoparticle-added, and Fe_3O_4-nanoparticle-added $Bi_{1.6}Pb_{0.4}Sr_2Ca_2Cu_3O_{10+\delta}$ superconductor.

CONCLUSIONS

In this dissertation, the explorations of the issue of critical current density and pinning mechanism in Bi-Pb-Sr-Ca-Cu-O superconductors with three types of 0D APC, including Na-substitution, TiO_2 nanoparticle addition and Fe_3O_4 nanoparticle addition, were carried out. Main results of this dissertation, improvements of J_c in BPSCCO superconductors via the addditions of 0D APC was systematically investigated, and summarized as the followings:

For the BPSCCO superconductors with the substitution of Na into Ca site, the dominant pinning mechanism appeared to be temperature independent. The improved flux pinning properties in the Na-substituted samples were induced the growth of point-like pinning and the decline of grain boundary pinning resulting from the Na substitution. Especially, the δl pinning was found to be the predominant pinning mechanism responsible for the samples.

For the BPSCCO superconductors with the addition of non-magnetic TiO_2 nanoparticles, the $J_c(B)$ of the samples were enhanced by adequate doping contents of x = 0.002, 0.004. The results revealed the extension of the small and large bundle regimes with adequate amounts of TiO_2 nanoparticles. The $j(t)$ analyses exhibited that the δl pinning was the dominant pinning mechanism in all samples. The normalized field dependence of f_p was investigated to clarify the influence of TiO_2 nanoparticles as normal core point pinning. Additionally, a close correlation between local structural variations and change in T_c of the BPSCCO was investigated.

For the BPSCCO samples with the additions of magnetic Fe_3O_4 nanoparticles, the enhancements of J_c were obtained for x = 0.01 and 0.02. The appearance of additional normal core point pinning centers in the doped samples was confirmed by using the Dew–Hughes model. Interestingly, the

additions of magnetic nanoparticles were concluded to provide the strongest enhancements of J_c among the methods used in the research.

Motivated by results presented in the dissertation, further studies on BPSCCO superconductors will be carried out. The effects of volume pin – by using nanoparticles with larger size and columnar pin – by adding nanotubes or self-assembled nanorods/nanocolumns are being predicted to play important roles in comparing and understanding possible shifts in pinning mechanism in BPSCCO. Consequently, the key factors to apply nano-technology in the enhancements of flux-pinning properties in type-II superconductors will be obtained.

DISSERTATION PUBLICATIONS

[1] **An T. Pham**, Dzung T. Tran, Duong B. Tran, Luu T. Tai, Nguyen K. Man, Nguyen T. M. Hong, Tien M. Le, Duong Pham, Won-Nam Kang, Duc H. Tran (2021), "Unravelling the scaling characteristics of flux pinning forces in $Bi_{1.6}Pb_{0.4}Sr_2Ca_{2-x}Na_xCu_3O_{10+\delta}$ superconductors", Journal of Electronics Materials 50, pp. 1444-1451.

[2] Dzung T. Tran, **An T. Pham**, Ha H. Pham, Nhung T. Nguyen, Nguyen H. Nam, Nguyen K. Man, Won-Nam Kang, I-Jui Hsu, Wantana Klysubun, Duc H. Tran (2021), "Local structure and superconductivity in $(Bi_{1.6}Pb_{0.4}Sr_2Ca_2Cu_3O_{10+\delta})_{1-x}(Fe_3O_4)_x$ compounds", Ceramics International 47(12), pp. 16950-16955.

[3] **An T. Pham**, Dzung T. Tran, Ha H. Pham, Nguyen H. Nam, Luu T. Tai, Duc H. Tran (2021), "Improvement of flux pinning properties in Fe_3O_4 nanoparticle-doped $Bi_{1.6}Pb_{0.4}Sr_2Ca_2Cu_3O_{10+\delta}$ superconductors", Materials Letters 298, pp. 130015(1-5).

[4] **An T. Pham**, Dzung T. Tran, Linh H. Vu, Nang T.T. Chu, Nguyen Duy Thien, Nguyen H. Nam, Nguyen Thanh Binh, Luu T. Tai, Nguyen T.M. Hong, Nguyen Thanh Long, Duc H. Tran (2022), "Effects of TiO_2 nanoparticle addition on the flux pinning properties of the $Bi_{1.6}Pb_{0.4}Sr_2Ca_2Cu_3O_{10+\delta}$ ceramics", Ceramics International 48(14), pp. 20996–21004.

[5] **An T. Pham**, Linh H. Vu, Dzung T. Tran, Nguyen Duy Thien, Wantana Klysubun, T. Miyanaga, Nguyen K. Man, Nhan T.T. Duong, Nguyen Thanh Long, Phong V. Pham, Nguyen Thanh Binh, Duc H. Tran (2023), "Correlation between local structure variations and critical temperature of

($Bi_{1.6}Pb_{0.4}Sr_2Ca_2Cu_3O_{10+\delta})_{1-x}(TiO_2)_x$ superconductor", Ceramics International 49(7), pp. 10506-10512.

[6] Tran Tien Dung, **Pham The An**, Tran Ba Duong, Nguyen Khac Man, Nguyen Thi Minh Hien, Tran Hai Duc (2021), "Excess Conductivity Analyses in Bi-Pb-Sr-Ca-Cu-O Systems Sintered at Different Temperatures", VNU Journal of Science: Mathematics – Physics 37(4), pp. 1-10.

[7] **An T. Pham**, Thao V. Nguyen, Yen T. Pham, Duc H. Tran, Nguyen K. Man, Dang T. B. Hop (2019), "Effects of Fe_3O_4 nanoparticle addition on structural and superconducting properties of $Bi_{1.6}Pb_{0.4}Sr_2Ca_2Cu_3O_{10+\delta}$ system", Proceedings of The 4th International Conference on Advanced Materials and Nanotechnology, pp. 17-20.

[8] **An T. Pham**, Duc V. Ngo, Duc H. Tran, Nguyen K. Man, Dang T. B. Hop (2019), "Improvements of flux pinning properties in $Bi_{1.6}Pb_{0.4}Sr_2Ca_2Cu_3O_{10+\delta}$ system by Na substitutions", Proceedings of The 4th International Conference on Advanced Materials and Nanotechnology, pp. 36-39.

[9] **An T. Pham**, Dzung T. Tran, Luu T. Tai, Nhung T. Nguyen, Nguyen K. Man, Dang T. B. Hop, Phung Manh Thang, Duc H. Tran (2022), "Investigation of flux pinning properties of the $(Bi_{1.6}Pb_{0.4}Sr_2Ca_2Cu_3O_{10+\delta})_{1-X}(Fe_3O_4)_X$ superconductors", Proceedings of The 12th Vietnam National Conference of Solid Physics and Materials Science, pp. 19-22.

REFERENCE

[1] Abbas M.M., Dehi H.D. (2014), "Influences of K Substitution on Bi (Pb) -2223 Superconductors", (2), pp. 177–179.

[2] Abd-Shukor R., Jannah A.N. (2017), "Advances in superconductivity and Co3O4 nanoparticles as flux pinning center in (Bi, Pb)-2223/Ag superconductor tapes", *AIP Conf. Proc.* 1877(September), pp. 1–7.

[3] Abrikosov A.A. (1957), "Magnetic properties of superconductors of the second type", *Zh. Eksp. Teor. Fiz.* 32(6), pp. 1442–1452.

[4] Albiss B.A., Obaidat I.M., Gharaibeh M., Ghamlouche H., Obeidat S.M. (2010), "Impact of addition of magnetic nanoparticles on vortex pinning and microstructure properties of Bi-Sr-Ca-Cu-O superconductor", *Solid State Commun.* 150(33–34), pp. 1542–1547.

[5] Anderson P.W., Zou Z. (1988), "'Normal' Tunneling and 'Normal' Transport: Diagnostics for the Resonating-Valence-Bond State", *Phys. Rev. Lett.* 60(2), pp. 132–135.

[6] Annabi M., M'chirgui A., Ben Azzouz F., Zouaoui M., Ben Salem M. (2004), "Addition of nanometer Al_2O_3 during the final processing of (Bi,Pb)-2223 superconductors", *Phys. C Supercond.* 405(1), pp. 25–33.

[7] Aslamasov L.G., Larkin A.I. (1968), "The influence of fluctuation pairing of electrons on the conductivity of normal metal", *Phys. Lett. A* 26(6), pp. 238–239.

[8] Atikur Rahman M. (2015), "A Review on Cuprate Based Superconducting Materials Including Characteristics and Applications", *Am. J. Phys. Appl.* 3(2), pp. 39.

[9] Bardeen J., Cooper L.N., Schrieffer J.R. (1957), “Theory of superconductivity”, *Phys. Rev.* 108(5), pp. 1175–1204.

[10] Bean C.P. (1964), “Magnetization of High-Field Superconductors”, *Rev. Mod. Phys.* 36(1), pp. 31–31.

[11] Bielecki J., Bozek S., Dutkiewicz E., Hajduk R., Jarzyna J., Lekki J., Pieprzyca T., Stachura Z., Szklarz Z., Kwiatek W.M. (2012), “Preliminary investigations of elemental content, microporosity, and specific surface area of porous rocks using pixe and X-ray microtomography techniques”, *Acta Phys. Pol. A* 121(2), pp. 474–479.

[12] Biju A., Aloysius R.P., Syamaprasad U. (2005), “Enhanced critical current density in Gd-added (Bi, Pb)-2212 bulk superconductor”, *Supercond. Sci. Technol.* 18(11), pp. 1454–1459.

[13] Bilgili O., Selamet Y., Kocabaş K. (2008), “Effects of Li substitution in Bi-2223 superconductors”, *J. Supercond. Nov. Magn.* 21(8), pp. 439–449.

[14] Blatter G., Feigel’Man M. V., Geshkenbein V.B., Larkin A.I., Vinokur V.M. (1994), “Vortices in high-temperature superconductors”, *Rev. Mod. Phys.* 66(4), pp. 1125–1388.

[15] Bordet P., Capponi J.J., Chaillout C., Chenavas J., Hewat A.W., Hewat E.A., Hodeau J.L., Marezio M., Tholence J.L., Tranqui D. (1988), “Powder X-ray and neutron diffraction study of the superconductor $Bi_2Sr_2CaCu_2O_8$”, *Phys. C Supercond.* 153–155(PART 2), pp. 623–624.

[16] Campbell A.M., Evetts J.E., Dew-Hughes D. (2016), “Pinning of Flux Vortices in Type II Superconductors”, *Philos. Mag.* 18(152), pp. 313–343.

[17] Christova K., Manov A., Nyhus J., Thisted U., Herstad O., Foss S.E., Haugen K.N., Fossheim K. (2002), "$Bi_2Sr_2CaCu_2O_x$ bulk superconductor with MgO particles embedded", *J. Alloys Compd.* 340(1–2), pp. 1–5.

[18] Clem J.R. (1991), "Two-dimensional vortices in a stack of thin superconducting films: A model for high-temperature superconducting multilayers", *Phys. Rev. B* 43(10), pp. 7837–7846.

[19] Davar F., Fereshteh Z., Salavati-niasari M. (2009), "Nanoparticles Ni and NiO : Synthesis , characterization and magnetic properties", 476, pp. 797–801.

[20] Dew-Hughes D. (1974), "Flux pinning mechanisms in type II superconductors", *Philos. Mag.* 30(2), pp. 293–305.

[21] Efetov K.B. (1980), "Effect of random distortions on the critical field in layered superconductors", *J. Low Temp. Phys.* 38(5–6), pp. 719–735.

[22] Eisaki H., Kaneko N., Feng D.L., Damascelli A., Mang P.K., Shen K.M., Shen Z.X., Greven M. (2004), "Effect of chemical inhomogeneity in bismuth-based copper oxide superconductors", *Phys. Rev. B* 69(6), pp. 064512-1–7.

[23] Ghattas A., Annabi M., Zouaoui M., Azzouz F. Ben, Salem M. Ben (2008), "Flux pinning by Al-based nano particles embedded in polycrystalline (Bi,Pb)-2223 superconductors", *Phys. C Supercond. Its Appl.* 468(1), pp. 31–38.

[24] Ghorbani S.R., Farshidnia G., Wang X.L., Dou S.X. (2014), "Flux pinning mechanism in SiC and nano-C doped MgB2: Evidence for transformation from δT_c to $\delta \ell$ pinning", *Supercond. Sci. Technol.* 27(12), pp. 125003-1–7.

[25] Ghorbani S.R., Wang X.L., Dou S.X., Lee S.I.K., Hossain M.S.A. (2008), "Flux-pinning mechanism in silicone-oil-doped MgB_2: Evidence for charge-carrier mean free path fluctuation pinning", *Phys. Rev. B - Condens. Matter Mater. Phys.* 78(18), pp. 184502-1–5.

[26] Ginzburg V.L., Landau L.D. (1950), "On the Theory of superconductivity", *Zh. Eksp. Teor. Fiz.* 20, pp. 1064–1082.

[27] Griessen R., Wen Hai-Hu, Van Dalen A.J.J., Dam B., Rector J., Schnack H.G., Libbrecht S., Osquiguil E., Bruynseraede Y. (1994), "Evidence for mean free path fluctuation induced pinning in $YBa_2Cu_3O_7$ and $YBa_2Cu_4O_8$ films", *Phys. Rev. Lett.* 72(12), pp. 1910–1913.

[28] Gündoğmuş H. (2017), "The effect of Y substitution on Bi-2212 superconductor by sol–gel method", *J. Mater. Sci. Mater. Electron.* 28(17), pp. 12598–12605.

[29] Gupta S.M., Tripathi M. (2011), "A review of TiO_2 nanoparticles", *Chinese Sci. Bull.* 56(16), pp. 1639–1657.

[30] Habermeier H.U. (2016), "Science and technology of cuprate-based high temperature superconductor thin films, heterostructures and superlattices—the first 30 years (Review Article)", *Low Temp. Phys.* 42(10), pp. 840.

[31] Han S.H., Lundqvist P., Rapp Ö. (1997), "Excess conductivity in $Y_{1-2x}Ca_xTb_xBa_2Cu_3O_{7-\delta}$", *Phys. C Supercond.* 282–287(PART 3), pp. 1571–1572.

[32] Hannachi E., Slimani Y., Ekicibil A., Manikandan A., Azzouz F. Ben (2019), "Magneto-resistivity and magnetization investigations of YBCO superconductor added by nano-wires and nano-particles of titanium

oxide", *J. Mater. Sci. Mater. Electron.* 30(9), pp. 8805–8813.

[33] Hohenberg P.C., Halperin B.I. (1977), "Theory of dynamic critical phenomena", *Rev. Mod. Phys.* 49(3), pp. 435–479.

[34] Hosseinzadeh M., Ghorbani S.R., Arabi H. (2020), "On the Determination of Pinning Mechanisms and Regimes in Type-II Superconductors with Weak Thermal Fluctuations", *J. Supercond. Nov. Magn.* 33(4), pp. 971–980.

[35] Ibrahim E.M.M., Saleh S.A. (2007), "Influence of sintering temperature on excess conductivity in Bi-2223 superconductors", *Supercond. Sci. Technol.* 20(7), pp. 672.

[36] Iijima Y., Tanabe N., Kohno O., Ikeno Y. (1992), "In-plane aligned $YBa_2Cu_3O_{7-x}$ thin films deposited on polycrystalline metallic substrates", *Appl. Phys. Lett.* 60(6), pp. 769–771.

[37] Kamerlingh O.H. (1911), "The Superconductivity of Mercury", *Comm. Phys. Lab. Univ. Leiden* 122, pp. 122–124.

[38] Kang B., Tran D.H., Kang W.N. (2017), "Scaling of pinning forces in $BaSnO_3$-added $GdBa_2Cu_3O_{7-x}$ superconducting thin films", *Thin Solid Films* 624, pp. 16–20.

[39] Kim H.W., Jo Y.S., Kim S.W., Ko R.K., Ha D.W., Kim H.M., Joo J.H., Kim H.J., Kim S.B., Hur J. (2015), "Study of magnetomotive force control type superconducting magnet using BSCCO HTS wire", *IEEE Trans. Appl. Supercond.* 25(3), pp. 4600804-1–4.

[40] Kir M.E., Özkurt B., Aytekin M.E. (2016), "The effect of K-na co-doping on the formation and particle size of Bi-2212 phase", *Phys. B Condens.*

Matter 490, pp. 79–85.

[41] Kishan H., Awana V.P.S., de Oliveira T.M., Alam S., Saito M., de Lima O.F. (2007), "Superconductivity of nano-TiO_2-added MgB2", *Phys. C Supercond.* 458(1–2), pp. 1–5.

[42] Kizler P., Su H.L., Majewski P., Aldinger F. (1994), "EXAFS study of BiO bond lengths in '$Bi_2Sr_2CaCu_2O_8$' high-Tc superconductor", *Phys. C Supercond. Its Appl.* 233(3–4), pp. 415–422.

[43] Koblischka M., van Dalen A., Higuchi T., Yoo S., Murakami M. (1998), "Analysis of pinning in $NdBa_2Cu_3O_{7-\delta}$ superconductors", *Phys. Rev. B - Condens. Matter Mater. Phys.* 58(5), pp. 2863–2867.

[44] Koblischka M.R., Sosnowski J. (2005), "Temperature-dependent scaling of pinning force data in Bi-based high-Tc superconductors", *Eur. Phys. J. B* 44(3), pp. 277–280.

[45] Koblischka M.R., Koblischka-Veneva A., Murakami M. (2004), "Nanosized Pinning Sites in HTSC Compounds", *J. Supercond.* 17, pp. 373–377.

[46] Kocabaş K., Şakiroğlu S., Çiftçioğlu M., Ercan İ., Epik H., Bilgili O. (2009), "The Effect of Zn Substitution of Ca in Bi-Pb-Sr-Ca-Cu-O Superconductors Sintered at 830 °C", *J. Supercond. Nov. Magn.* 22(8), pp. 749–754.

[47] Kravtsova A.N., Mazalova V.L., Yalovega G.E., Soldatov A. V., Johnston R.L. (2009), "Analysis of the X-ray absorption fine structure near the Ti-L2, 3 edge in free titanium nanoclusters", *J. Surf. Investig.* 3(1), pp. 38–40.

[48] Kwok W.K., Welp U., Glatz A., Koshelev A.E., Kihlstrom K.J., Crabtree G.W. (2016), "Vortices in high-performance high-temperature superconductors", Reports Prog. Phys. 79(11), pp. 116501-1–39.

[49] Lang W., Heine G., Kula W., Sobolewski R. (1995), "Superconducting fluctuations in Bi2Sr2Ca2Cu3Ox thin films: Paraconductivity, excess Hall effect, and magnetoconductivity", *Phys. Rev. B* 51(14), pp. 9180–9192.

[50] Larkin A.I., Ovchinnikov Y.N. (1979), "Pinning in Type II Superconductors", *J. Low Temp. Phys.* 34, pp. 409–428.

[51] Li B., Xu K., Hara S., Zhou D., Izumi M. (2013), "TiO2 addition effect on flux pinning properties of bulk $GdBa_2Cu_3O_{7-\delta}$ superconductors", *Phys. C Supercond.* 484, pp. 112–116.

[52] Li Y., Kang G., Gao Y. (2016), "Scaling rules for critical current density in anisotropic biaxial superconductors", *Phys. B Condens. Matter* 491, pp. 70–78.

[53] Lin B.N., Lin Y.X., Hsu Y.Y., Liao J.D., Cheng W.H., Lee J.F., Jang L.Y., Ku H.C. (2003), "Anomalous Pr ordering, Pr L3-edge and Cu K-edge XANES studies for the insulating $PrBa_2Cu_3O_{7-y}$ system", *J. Low Temp. Phys.* 131(5–6), pp. 803–807.

[54] Lobb C.J. (1987), "Critical fluctuations in high-Tc superconductors", *Phys. Rev. B* 36(7), pp. 3930–3932.

[55] Loudhaief N., Ben Salem M., Labiadh H., Zouaoui M. (2020), "Electrical properties and fluctuation induced conductivity studies of Bi-based superconductors added by CuS nanoparticles synthesized through the aqueous route", *Mater. Chem. Phys.* 242, pp. 122464.

[56] Lyuksyutov I.F., Naugle D.G. (1999), “Frozen flux superconductors”, *Mod. Phys. Lett. B* 13(15), pp. 491–497.

[57] MacManus-Driscoll J.L., Wimbush S.C. (2021), “Processing and application of high-temperature superconducting coated conductors”, *Nat. Rev. Mater.* 6(7), pp. 587–604.

[58] Maeda H., Tanaka Y., Fukutomi M., Asano T. (1993), *A New High-T c Oxide Superconductor without a Rare Earth Element*, in: Ten Years Supercond. 1980–1990, : pp. 303–304.

[59] Majewski P. (2000), “Materials aspects of the high-temperature superconductors in the system Bi_2O_3-SrO-CaO-CuO”, *J. Mater. Res.* 15(4), pp. 854–870.

[60] Meissner W., Ochsenfeld R. (1933), “Ein neuer Effekt bei Eintritt der Supraleitfähigkeit”, *Naturwissenschaften* 21(44), pp. 787–788.

[61] Mellekh A., Salem M. Ben, Zouaoui M. (2019), “Flux pinning mechanisms and competition between δl and δT_c pinning in polycrystalline nano-alumina-doped YBa 2 Cu 3 O 7-y”, *IEEE Trans. Appl. Supercond.* 29(1), pp. 1–19.

[62] Mohammed N.H., Awad R., Abou-Aly A.I., Ibrahim I.H., Hassan M.S. (2012), “Optimizing the Preparation Conditions of Bi-2223 Superconducting Phase Using PbO and PbO_2”, *Mater. Sci. Appl.* 03(04), pp. 224–233.

[63] Morita Y., Karppinen M., Yamauchi H., Liu R.S., Chen J.M. (2003), “XANES Study on the Evolution Among Different Copper Species, CuI, CuII and CuIII, in $CuBa_2YCu_2O_{6+z}$ Upon Oxygen Loading”, *J. Low Temp. Phys. 2003 1315* 131(5), pp. 1205–1210.

[64] Müller R., Schneider M., Mitdank R., Janowitz C., Unger R.S., Krapf A., Dwelk H., Frentrup W., Manzke R. (2002), "Systematic X-ray absorption study of hole doping in BSCCO-phases", *Phys. B Condens. Matter* 312–313, pp. 94–96.

[65] Mumtaz M., Waqee-ur-Rehman M., Rabbani M.W. (2017), "Comparative study of ferromagnetic and anti-ferromagnetic nanoparticles as artificial flux pinning centers in CuTl-1223 superconductor", *Ceram. Int.* 43(17), pp. 15842–15845.

[66] Mun M.O., Lee S.I., Suck Salk S.H., Shin H.J., Joo M.K. (1993), "Conductivity fluctuations in a single crystal of $Bi_2Sr_2CaCu_2O_x$", *Phys. Rev. B* 48(9), pp. 6703–6706.

[67] Newville M. (2014), "Fundamentals of XAFS", *Rev. Mineral. Geochemistry* 78(1), pp. 33–74.

[68] Nurbaisyatul E.S., Azhan H., Azman K., Ibrahim N. (2020), "Effect of CeO_2 Nanoparticle on the Structural and Electrical Properties of BSCCO-2223 High Temperature Superconductor", *Solid State Phenom.* 307, pp. 104–109.

[69] Nurbaisyatul E.S., Azhan H., Ibrahim N., Saipuddin S.F. (2021), "Structural and superconducting properties of low-density Bi(Pb)-2223 superconductor: Effect of Eu_2O_3 nanoparticles addition", *Cryogenics (Guildf).* 119, pp. 103353-1–9.

[70] Oh J.Y., Le T.M., Pham A.T., Tran D.H., Yang D.S., Kang B. (2019), "Role of interlayer coupling in alkaline-substituted (Bi, Pb)-2223 superconductors", *J. Alloys Compd.* 804, pp. 348–352.

[71] Özçelik B., Gürsul M., Sotelo A., Madre M.A. (2015), "Improvement of

superconducting properties in Na-doped BSCCO superconductor", *J. Mater. Sci. Mater. Electron.* 26(1), pp. 441–447.

[72] Özkurt B. (2014), "Improvement of the critical current density in Bi-2223 ceramics by sodium-silver co-doping", *J. Mater. Sci. Mater. Electron.* 25(8), pp. 3295–3300.

[73] Özkurt B. "The effects of yttrium substitution in Bi-2223 superconductors", 24(2), pp. 758–763.

[74] Palau A., Puig T., Obradors X., Pardo E., Navau C., Sanchez A., Usoskin A., Freyhardt H.C., Fernández L., Holzapfel B., Feenstra R. (2004), "Simultaneous inductive determination of grain and intergrain critical current densities of $YBa_2Cu_3O_{7-x}$ coated conductors", *Appl. Phys. Lett.* 84(2), pp. 230–232.

[75] Palau A., Valles F., Rouco V., Coll M., Li Z., Pop C., Mundet B., Gazquez J., Guzman R., Gutierrez J., Obradors X., Puig T. (2018), "Disentangling vortex pinning landscape in chemical solution deposited superconducting $YBa_2Cu_3O_{7-x}$ films and nanocomposites", *Supercond. Sci. Technol.* 31(3), pp. 034004-1–12.

[76] Pham A.T., Tran D.T., Pham H.H., Nam N.H., Tai L.T., Tran D.H. (2021), "Improvement of flux pinning properties in Fe_3O_4 nanoparticle-doped $Bi_{1.6}Pb_{0.4}Sr_2Ca_2Cu_3O_{10+\delta}$ superconductors", *Mater. Lett.* 298, pp. 130015-1–5.

[77] Pham A.T., Tran D.T., Vu L.H., Chu N.T.T., Thien N.D., Nam N.H., Binh N.T., Tai L.T., Hong N.T.M., Long N.T., Tran D.H. (2022), "Effects of TiO_2 nanoparticle addition on the flux pinning properties of the $Bi_{1.6}Pb_{0.4}Sr_2Ca_2Cu_3O_{10+\delta}$ ceramics", *Ceram. Int.* 48(14), pp. 20996–

21004.

[78] Pham D., Jung S.G., Tran D.H., Park T., Kang W.N. (2019), “Effects of oxygen ion implantation on single-crystalline MgB_2 thin films”, *J. Appl. Phys.* 125(2), pp. 023904-1–7.

[79] Prischepa S.L., Della Rocca M.L., Maritato L., Salvato M., Di Capua R., Maglione M.G., Vaglio R. (2003), “Critical currents of (formula presented) thin films deposited in situ by sputtering”, *Phys. Rev. B - Condens. Matter Mater. Phys.* 67(2), pp. 6–9.

[80] Qin M.J., Wang X.L., Liu H.K., Dou S.X. (2002), “Evidence for vortex pinning induced by fluctuations in the transition temperature of MgB superconductors”, *Phys. Rev. B - Condens. Matter Mater. Phys.* 65(13), pp. 1–4.

[81] Rao K.V.R., Garg K.B. (1991), “XANES study of oxygen doping in 1-2-3 system”, *Bull. Mater. Sci.* 14(3), pp. 853–858.

[82] Rao K.V.R., Garg K.B., Agarwal S.K., Awana V.P.S., Narlikar A. V. (1992), “Cu K-edge X-ray absorption study of Fe-doped $Bi_2Ca_1Sr_2Cu_2O=$ superconductors”, *Phys. C Supercond. Its Appl.* 192(3–4), pp. 419–424.

[83] Ray P.J., Lefmann K., Udby L. (2015), *Structural investigation of La $_{2-x}$ Sr $_x$ CuO $_{4+y}$ Following staging as a function of temperature Academic advisors*, .

[84] Rey C.M., Malozemoff A.P. (2015), “Fundamentals of superconductivity”, *Supercond. Power Grid Mater. Appl.*, pp. 29–73.

[85] Rietveld H.M. (1969), “A profile refinement method for nuclear and magnetic structures”, *J. Appl. Crystallogr.* 2(2), pp. 65–71.

[86] Saleem A., Hussain S.T. (2014), “Review the High Temperature Superconductor (HTSC) Cuprates-Properties and Applications”, *J. Surfaces Interfaces Mater.* 1(2), pp. 97–119.

[87] Saleh S.A., Ahmed S.A., Elsheikh E.M.M. (2008), “A study on thermoelectric power and electrical properties of Bi-2223 superconductors sintered for different time periods”, *J. Supercond. Nov. Magn.* 21(3), pp. 187–192.

[88] Sales B.C., Chakoumakos B.C. (1991), “Hole filling and hole creation in the superconducting compounds $Bi_2Sr_{2-x}R_xCuO_{6+y}$ (R=La, Pr, Nd, and Sm)”, *Phys. Rev. B* 43(16), pp. 12994–13000.

[89] Saritekin N.K., Üzümcü A.T. (2022), “Improving Superconductivity, Microstructure, and Mechanical Properties by Substituting Different Ionic Pb Elements to Bi and Ca Elements in Bi-2223 Superconductors”, *J. Supercond. Nov. Magn.* 35(9), pp. 2259–2273.

[90] Shalaby M.S., Hamed M.H., Yousif N.M., Hashem H.M. (2021), “The impact of the addition of Bi_2Te_3 nanoparticles on the structural and the magnetic properties of the Bi-2223 high-Tc superconductor”, *Ceram. Int.* 47(18), pp. 25236–25248.

[91] Shibata T., Sakai S.I. (2016), “Passive Micro Vibration Isolator Utilizing Flux Pinning Effect for Satellites”, *J. Phys. Conf. Ser.* 744(1), pp. 1–12.

[92] Solovjov A.L., Habermeier H.U., Haage T. (2002), “Fluctuation conductivity in $YBa_2Cu_3O_{7-y}$ films with different oxygen content. I. Optimally and lightly doped YBCO films”, *Low Temp. Phys.* 28(1), pp. 17–24.

[93] Song L.W., Yang M., Chen E., Kao Y.H. (1992), “Pinning-force scaling

and magnetic relaxation in doped Y-Ba-Cu-O thin films", *Phys. Rev. B* 45(6), pp. 3083–3092.

[94] Takano M., Takada J., Oda K., Kitaguchi H., Miura Y., Ikeda Y., Tomii Y., Mazaki H. (1988), "High-Tc Phase Promoted and Stabilized in the Bi, Pb-Sr-Ca-Cu-O System", *Jpn. J. Appl. Phys.* 27(6A), pp. L1041–L1043.

[95] Tran D.H., Le T.M., Do T.H., Dinh Q.T., Duong N.T.T., Anh D.T.K., Man N.K., Pham D., Kang W.N. (2018), "Enhancements of critical current density in the Bi-Pb-Sr-Ca-Cu-O superconductor by Na substitution", *Mater. Trans.* 59(7), pp. 1071–1074.

[96] Tran D.H., Pham A.T., Le T.M., Anh D.T.K., Phan Y.T., Man N.K., Pham D., Kang W.N. (2019), "Enhanced flux pinning properties in $Bi_{1.6}Pb_{0.4}Sr_{2-x}K_xCa_2Cu_3O_{10+\delta}$ compounds", *J. Mater. Sci. Mater. Electron.* 30(9), pp. 8233–8238.

[97] Tran D.T., Pham A.T., Pham H.H., Nguyen N.T., Nam N.H., Man N.K., Kang W.N., Hsu I.J., Klysubun W., Tran D.H. (2021), "Local structure and superconductivity in $(Bi_{1.6}Pb_{0.4}Sr_2Ca_2Cu_3O_{10+\delta})_{1-x}(Fe_3O_4)_x$ compounds", *Ceram. Int.* 47(12), pp. 16950–16955.

[98] Tranquada J.M., Heald S.M., Moodenbaugh A.R., Xu Y. (1988), "Mixed valency, hole concentration, and Tc in $YBa_2Cu_3O_{6+x}$", *Phys. Rev. B* 38(13), pp. 8893–8899.

[99] Tripathi D., Dey T.K. (2014), "Critical current density of MgB_2 superconductor with (Bi , Pb) -2223 addition", *J. Alloys Compd.* 607, pp. 264–273.

[100] Vaitkus A., Merkys A., Grazulis S. (2021), "Validation of the Crystallography Open Database using the Crystallographic Information

Framework", *J. Appl. Crystallogr.* 54(2), pp. 661–672.

[101] Vinu S., Sarun P.M., Shabna R., Biju A., Syamaprasad U. (2008), "Improved microstructure and flux pinning properties of Gd-substituted (Bi,Pb)-2212 superconductor sintered between 846 and 860 °C", *Mater. Lett.* 62(29), pp. 4421–4424.

[102] Vinu S., Sarun P.M., Shabna R., Biju A., Syamaprasad U. (2008), "Enhancement of critical current density and flux pinning properties of Gd-doped (Bi, Pb)-2212 superconductor", *J. Appl. Phys.* 104(4), pp. 1–6.

[103] Wang J.L., Zeng R., Kim J.H., Lu L., Dou S.X. (2008), "Effects of C substitution on the pinning mechanism of MgB2", *Phys. Rev. B - Condens. Matter Mater. Phys.* 77(17), pp. 1–7.

[104] Wei K., Abd-Shukor R. (2007), "Superconducting and transport properties of (Bi-Pb)-Sr-Ca-Cu-O with nano-Cr $_2$O $_3$ additions", *J. Electron. Mater.* 36(12), pp. 1648–1651.

[105] Wördenweber R. (1999), "Mechanism of vortex motion in high-temperature superconductors", *Reports Prog. Phys.* 62(2), pp. 187–236.

[106] Xi'Ang F.X., Wang X.L., Xun X., De Silva K.S.B., Wang Y.X., Dou S.X. (2013), "Evidence for transformation from δT_c to δl pinning in MgB2 by graphene oxide doping with improved low and high field Jc and pinning potential", *Appl. Phys. Lett.* 102(15), pp. 152601.

[107] Yang C.Y., Heald S.M., Tranquada J.M., Xu Y., Wang Y.L., Moodenbaugh A.R., Welch D.O., Suenaga M. (1989), "Variation of electronic and atomic structures in $YBa_2(Cu_{1-x}Fe_x)_3O_{7-}$", *Phys. Rev. B* 39(10), pp. 6681–6689.

[108] Yavuz Ş., Bilgili Ö., Kocabaş K. (2016), "Effects of superconducting parameters of SnO_2 nanoparticles addition on (Bi, Pb)-2223 phase", *J. Mater. Sci. Mater. Electron.* 27(5), pp. 4526–4533.

[109] Yildirim G. (2013), "Beginning point of metal to insulator transition for Bi-2223 superconducting matrix doped with Eu nanoparticles", *J. Alloys Compd.* 578, pp. 526–535.

[110] Yildirim G. (2017), "Determination of optimum diffusion annealing temperature for Au surface-layered Bi-2212 ceramics and dependence of transition temperatures on disorders", *J. Alloys Compd.* 699, pp. 247–255.

[111] Zhang S., Li C., Hao Q., Feng J., Lu T., Zhang P. (2015), "Optimized Intergrain Connection and Transport Properties of Bi-2212 High-Temperature Superconductors by Ag Nanoparticles Inclusions", *J. Supercond. Nov. Magn. 2015 286* 28(6), pp. 1729–1736.

[112] Zhang S., Li C., Hao Q., Lu T., Zhang P. (2015), "Influences of Yb substitution on the intergrain connections and flux pinning properties of Bi-2212 superconductors", *Phys. C Supercond. Its Appl.* 511, pp. 26–32.

[113] Zhang S., Liang M., Li C., Hao Q., Feng J., Zhang P. (2015), "Enhanced flux pinning properties in Bi-2212 high temperature superconductors with nano-sized precipitates", *Mater. Lett.* 157, pp. 197–200.

[114] Zouaoui M., Ghattas A., Annabi M., Ben Azzouz F., Ben Salem M. (2008), "Effect of nano-size ZrO_2 addition on the flux pinning properties of (Bi, Pb)-2223 superconductor", *Supercond. Sci. Technol.* 21(12), pp. 125005-1–7.

[115] https://www.britannica.com/science/Bragg-law.